UNIVERSITÀ DEGLI STUDI DI NAPOLI "FEDERICO II"

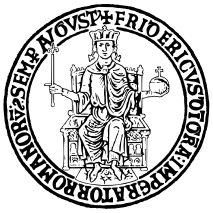

SCUOLA DI MEDICINA E CHIRURGIA

Dipartimento di Scienze Biomediche Avanzate

Direttore Prof. Alberto Cuocolo

DOTTORATO DI RICERCA IN SCIENZE BIOMORFOLOGICHE E CHIRURGICHE

XXXIII CICLO

Coordinatore Prof. Alberto Cuocolo

TESI DI DOTTORATO

Advanced MRI techniques in the study of cerebellar cortex

RELATORE

Ch.mo Prof. Arturo Brunetti

CANDIDATO

Dott. Sirio Cocozza

CONTENTS

LIST OF PUBLICATIONS **4**

SUMMARY **5**

CHAPTER 1: CEREBELLUM **7**

1.1 *ANATOMY* **7**

1.2 *INTRINSIC CIRCUITRY* **13**

1.3 *CONNECTIONS* **16**

1.3.1 Afferents **16**

1.3.2 Efferents **21**

CHAPTER 2: MAGNETIC RESONANCE IMAGING **26**

2.1 *VOLUMETRIC ANALYSES* **26**

2.1.1 Image segmentation **26**

2.1.2 Voxel based morphometry **32**

2.1.3 Cerebellar segmentation methods **36**

2.2 *FUNCTIONAL MRI* **39**

2.2.1 Principles **39**

2.2.2 fMRI data analysis methods **42**

CHAPTER 3: ULTRA-HIGH FIELD CEREBELLAR SEGMENTATION METHOD DEVELOPMENT **46**

3.1 *BACKGROUND* **46**

3.2 *METHODS* **47**

3.3 *RESULTS* **57**

3.4 *DISCUSSION* **67**

CHAPTER 4: CEREBELLAR CORTEX INVOLVEMENT IN FRIEDREICH'S ATAXIA .71

4.1 *BACKGROUND* **71**

4.2 *METHODS* **73**

4.3 *RESULTS* **77**

4.4 *DISCUSSION* **81**

CHAPTER 5: CEREBELLAR CORTEX INVOLVEMENT IN IDIOPATHIC CERVICAL DYSTONIA..... 86

5.1 *BACKGROUND* **86**

5.2 *METHODS* **88**

5.3 *RESULTS* **93**

5.4 *DISCUSSION* **97**

CHAPTER 6: CEREBELLAR CORTEX INVOLVEMENT IN MULTIPLE SCLEROSIS 101

6.1 *BACKGROUND* **101**

6.2 *METHODS* **103**

6.3 *RESULTS* **107**

6.4 *DISCUSSION* **113**

CONCLUSIONS AND FUTURE PERSPECTIVES 116

BIBLIOGRAPHY 117

LIST OF PUBLICATIONS

- **Cocozza S**, Pontillo G, Russo C, Russo CV, Costabile T, Pepe A, Tedeschi E, Lanzillo R, Brescia Morra V, Brunetti A, Inglese M, Petracca M. *Cerebellum and cognition in progressive MS patients: functional changes beyond atrophy?* Journal of Neurology 2018 Oct;265(10):2260-2266. doi: 10.1007/s00415-018-8985-6. Epub 2018 Jul 28. PMID: 30056570

- **Cocozza S**, Costabile T, Pontillo G, Lieto M, Russo C, Radice L, Pane C, Filla A, Brunetti A, Saccà F. *Cerebellum and cognition in Friedreich ataxia: a voxel-based morphometry and volumetric MRI study.* Journal of Neurology 2020 Feb;267(2):350-358. doi: 10.1007/s00415-019-09582-9. Epub 2019 Oct 22. PMID: 31641877

- El Mendili MM, Petracca M, Podranski K, Fleysher L, **Cocozza S**, Inglese M. *SUITer: An Automated Method for Improving Segmentation of Infratentorial Structures at Ultra-High-Field MRI.* Journal of Neuroimaging 2020 Jan;30(1):28-39. doi: 10.1111/jon.12672. Epub 2019 Nov 5. PMID: 31691416

- Pontillo G, Castagna A, Vola EA, Macerollo A, Peluso S, Russo C, Baglio F, Manganelli F, Brunetti A, **Cocozza S**, Esposito M. *The cerebellum in idiopathic cervical dystonia: A specific pattern of structural abnormalities?* Parkinsonism & Related Disorders 2020 Nov;80:152-157. doi: 10.1016/j.parkreldis.2020.09.033. Epub 2020 Sep 23. PMID: 33010532

SUMMARY

The cerebellum (from the Latin “little brain”) is the dorsal portion of the metencephalon and is located in the posterior cranial fossa. Although representing only 10% of the total brain volume, it contains more than 50% of the total number of neurons of the central nervous system (CNS). Its organization resembles the one found in the telencephalon, with the presence of a superficial mantle of gray matter (GM) known as the cerebellar cortex, covering the cerebellar white matter (WM) in which three pairs of deep cerebellar GM nuclei are embedded.

The number of studies dedicated to the study of the cerebellum and its function has significantly increased during the last years. Nevertheless, although many theories on the cerebellar function have been proposed, to date we still are not able to answer the question about the exact function of this structure. Indeed, the classical theories focused on the role of the cerebellum in fine-tuning for muscle control has been widely reconsidered during the last years, with new hypotheses that have been advanced. These include its role as sensory acquisition device, extending beyond a pure role in motor control and learning, as well as a pivotal role in cognition, with a recognized cerebellar participation in a variety of cognitive functions, ranging from mood control to language, memory, attention and spatial data management.

A huge contribution to our understanding of how the cerebellum participates in all these different aspects of motor and non-motor behavior comes from the application of advanced imaging techniques. In particular, Magnetic Resonance Imaging (MRI) can provide a non-invasive evaluation of anatomical integrity, as well as information about functional connections with other brain regions.

This thesis is organized as follows:

- In Chapter 1 is presented a general introduction to the cerebellar anatomy and functions, with particular reference to the anatomical organization of cerebellar cortex and its connections with the telencephalon

- Chapter 2 will contain a general overview about some of the major advanced MRI methods that can be applied to investigate the anatomical integrity and functional status of the cerebellar cortex

- In Chapter 3 will be presented a new method to evaluate the anatomy and integrity of cerebellar cortex using ultra-high field MRI scanners

- Chapters 4, 5 and 6 will contain data obtained from the application of some of the previously described advanced imaging techniques to the study of cerebellar cortex in neurodegenerative and neuroinflammatory disorders affecting the CNS.

CHAPTER 1

Cerebellum

1.1 Anatomy

Microscopically, the cerebellar cortex is organized in three layers that, from the most superficial to the more adjacent to the WM, are respectively the molecular layer, the Purkinje cell layer and the granular layer. These layers are collectively composed of five cell types: stellate, basket, Purkinje, Golgi and granule cells (Figure 1).

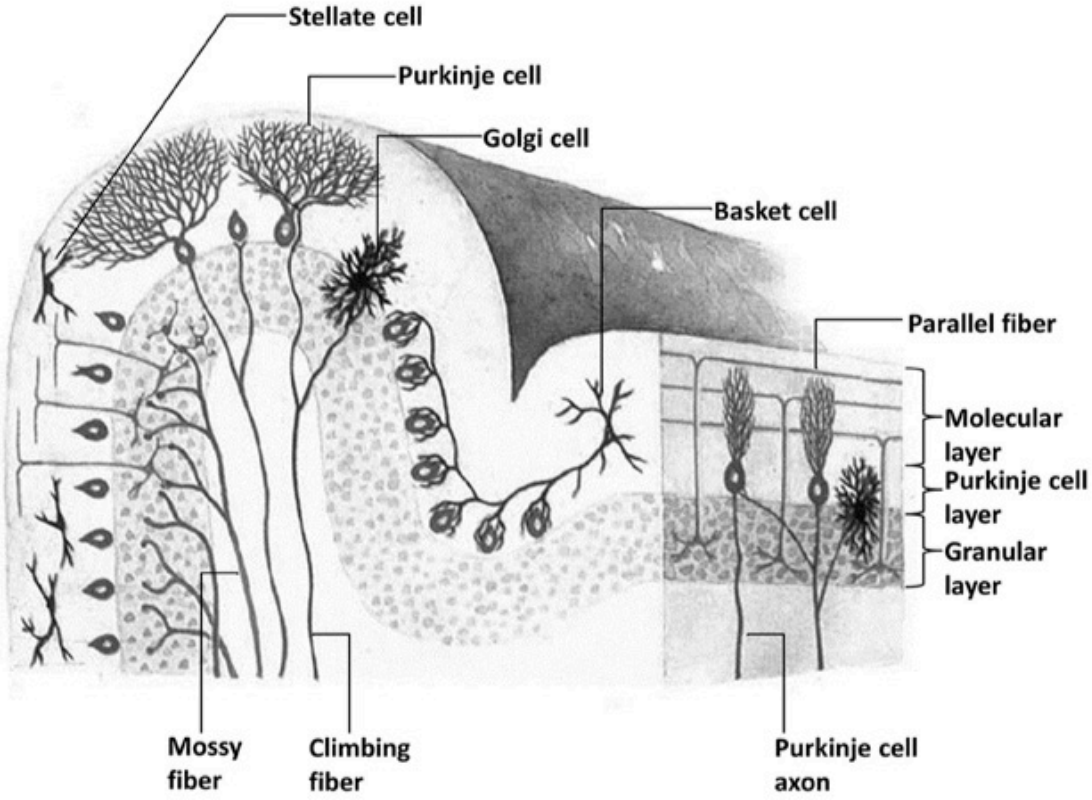

Figure 1: Histological organization of the cerebellar cortex (modified from (Mosconi, Wang, Schmitt, Tsai, & Sweeney, 2015))

The molecular layer is mostly composed by the parallel fibers arising from granule neurons and the dendritic zones of the Purkinje neurons, along with three types of interneurons (namely, the Golgi, stellate, and basket cells). The Purkinje cell layer is the intermediate one, mostly formed by a single line of Purkinje cells. On the other hand, the granular layer, although containing only the granule cells, plays a central role in the physiology of the cerebellum. Indeed, it contains the largest population of neurons in the cerebellum (granule cells), also being the only excitatory neurons of the cerebellar cortex. This very thick layer contains not only neuronal bodies, but also dendrites that receive many terminals from mossy fibers, which are part of the main afferent system, forming a complex synaptic arrangement also with terminals from a Golgi axons called the glomerulus. The axon of this granule neuron projects into the molecular layer through the Purkinje neuronal layer, where two opposite branches, perpendicular to the longitudinal axis of the folium are formed, called parallel fibers. In doing so, the axon of a granule neuron is therefore able to make synapsis with the dendritic zone of several Purkinje neurons, similarly to how telephone wires (i.e. granule neuronal axons) course from one telephone pole (i.e. dendritic zone of Purkinje neurons) to another. At this level are also present the dendrites of the climbing fibers, which are axons originating from olivary neurons entering through the inferior cerebellar peduncles. Some of these fibers create synapses with neurons of the deep cerebellar nuclei, while the main axon passes through the two deepest layers to reach the molecular one, where it entwines around the dendritic zone of the Purkinje neuron.

Finally, it is noteworthy to mention that besides mossy and climbing fibers, a third, often neglected, afferent system has been known since the late 1960s, which is the aminergic fibers system, which is made of axons showing a widespread distribution in the cerebellar cortex. More details about the biological and neurochemical functions of all these afferents fibers will be provided in Chapter 1.2.

Macroscopically, the cerebellum lies in the posterior cranial fossa, with the tentorium cerebelli that separates it from the cerebrum above. The cerebellar surface is characterized by the presence of

several parallel convolutions that run perpendicularly along its antero-posterior axis, giving it a characteristic appearance of leaves stemming from a same trunk. This appearance, that underwent the name of arbor vitae (from the Latin “life tree”), gave origin to the term folia (from the Latin “leaves”) that has been applied to the cerebellar convolutions. It covers the fourth ventricle, and is attached to the brainstem by three pairs of fiber bundles (namely, the inferior, middle and superior cerebellar peduncles) on each side of the ventricle. Briefly, the inferior cerebellar peduncles connect the spinal cord and medulla with the cerebellum, containing primarily afferent processes projecting to the cerebellum. The middle cerebellar peduncles connect the transverse pontine fibers with the cerebellum, which is entirely an afferent pathway, while the superior cerebellar peduncles connect the cerebellum with the mesencephalon, containing mainly efferent processes.

From a morphological standpoint, two major subdivisions can be recognized: a median portion (the vermis) and a lateral one (the hemispheres, in number of two) (Figure 2).

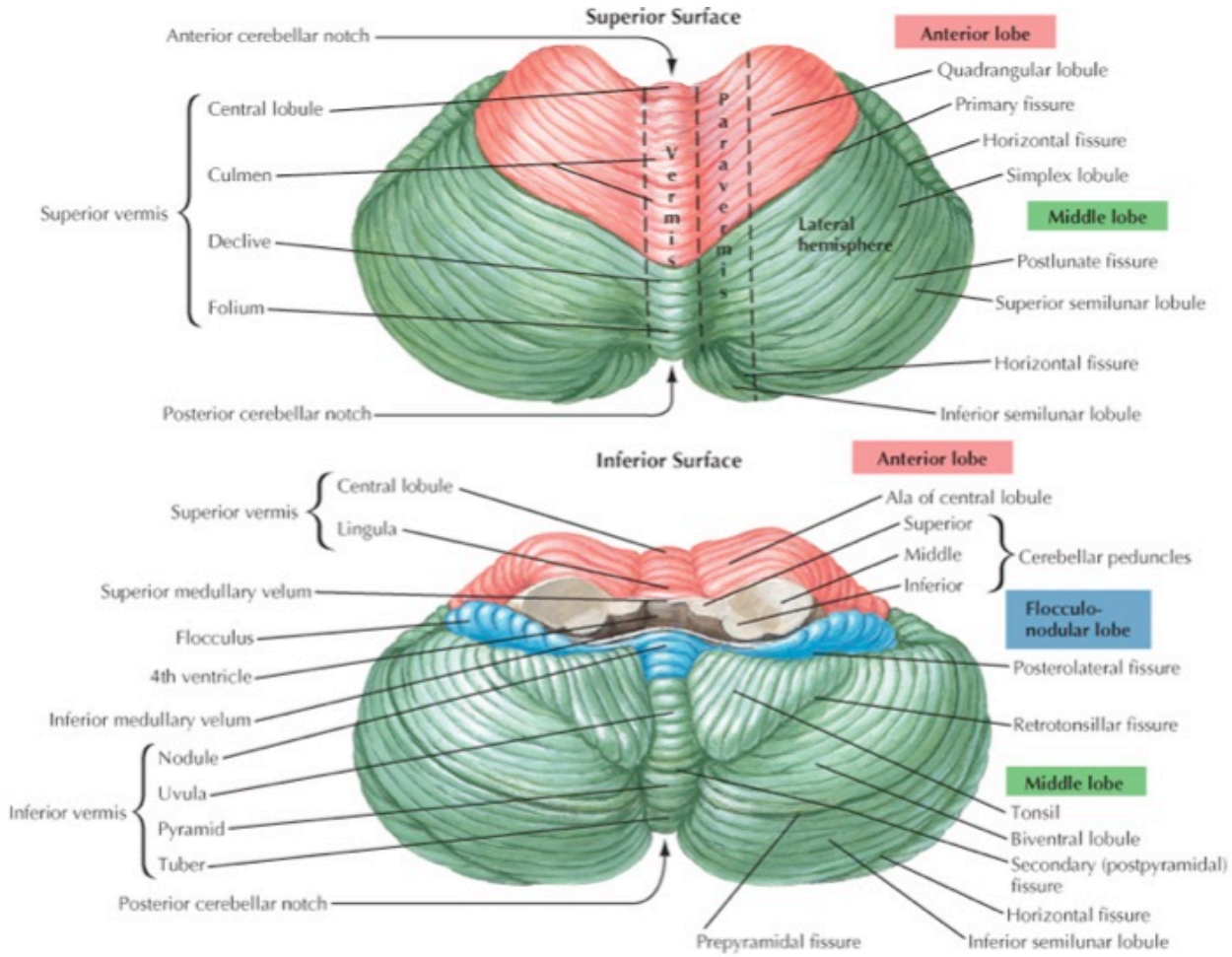

Figure 2: Morphological anatomy of the cerebellum (from (Felten, O'Banion, & Maida))

The superior vermis is confluent with the hemispheres, whereas the inferior vermis is a well-delineated structure that is located in a deep depression in the midline named the vallecula.

The presence of two deep fissures between the folia allows for the subdivision of the cerebellum in three major lobes: the anterior lobe, the posterior lobe and the flocculonodular lobule. The anterior lobe corresponds to the paleocerebellum and constitutes the rostral portion of the rostral cerebellar surface, being divided from the posterior one by the primary fissure, which is visible on the dorsal surface of the cerebellum. On the inferior surface lies the posterolateral fissure, which separates the posterior lobe (neocerebellum) from the flocculonodular lobule. The latter, also known as the archicerebellum or vestibulocerebellum, is therefore confined to the ventral aspect of the cerebellum, with the nodulus being the most rostral part of the caudal vermis.

An additional subdivision is the one achieved when the cerebellum is divided in 10 lobules (labeled using the roman numeration from I to X) for both vermis and hemispheres, with an antero-posterior gradient (Figure 3).

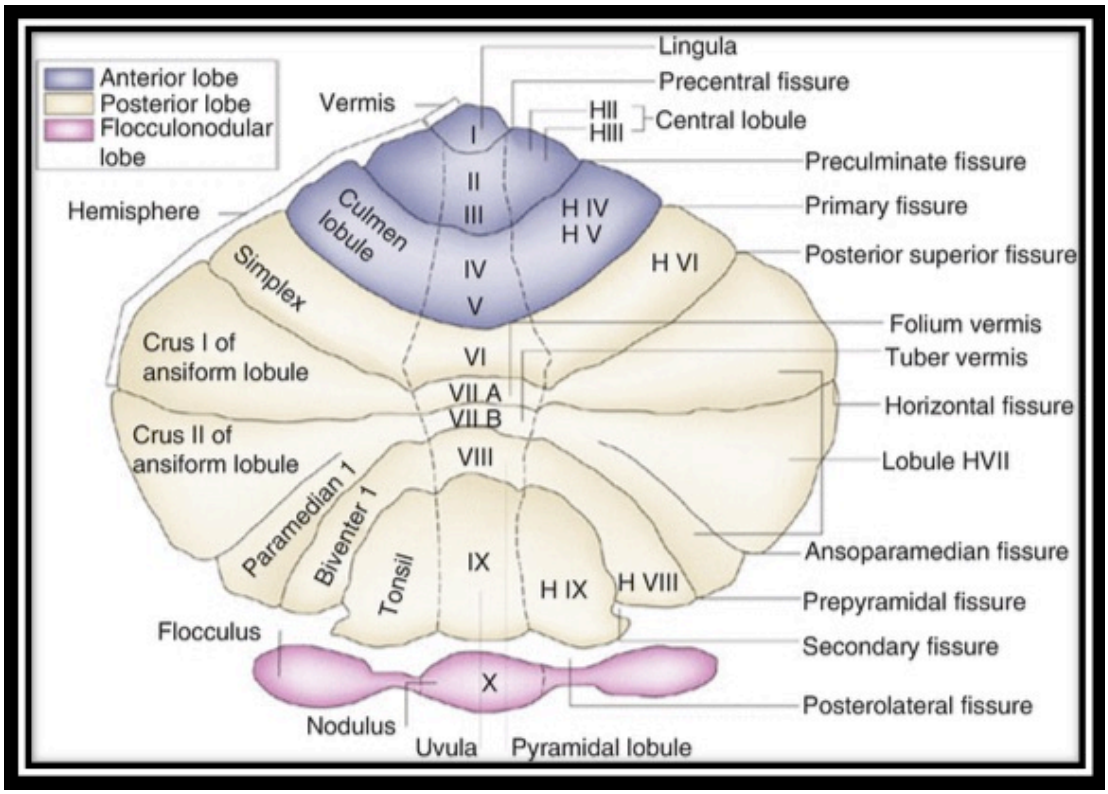

Figure 3: Lobular organization of the cerebellar cortex (modified from (Manni & Petrosini, 2004))

Finally, four pairs of deep GM nuclei are located within the cerebellar WM, which are (from medial to lateral) the fastigial, the globose, the emboliform, and the dentate nuclei (DN) (Figure 4). The globose and the emboliform nuclei are also referred as the interposed nuclei, given that they are indeed interposed between the fastigial and the DN. The input to the cerebellar nuclei is mainly derived from fibers arising from the Purkinje cells of the cerebellar cortex, although excitatory fibers from extra-cerebellar axons are also present in these areas.

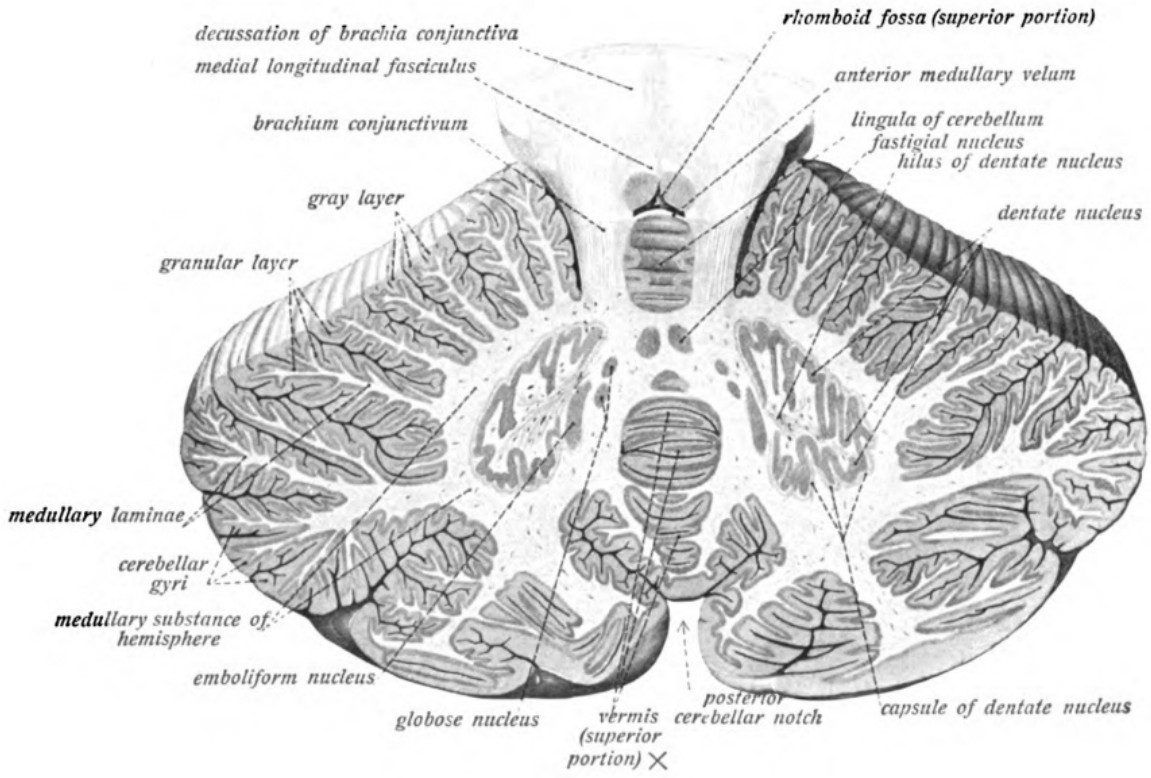

Figure 4: Cerebellar deep GM nuclei (from (Sobotta, 1908))

1.2 Intrinsic circuitry

The overall circuit in the cerebellar cortex can be very briefly summarized as follows: excitatory inputs to the cerebellar cortex are primarily derived from the afferent system (i.e. climbing and mossy fibers). This excitatory input is received by the Purkinje cells, which are in turn responsible, along with the additional inhibitory influences of the modulating interneurons, for the entire inhibitory output of the cerebellar cortex via projection through the deep cerebellar nuclei. A brief scheme of this circuit is presented in Figure 5.

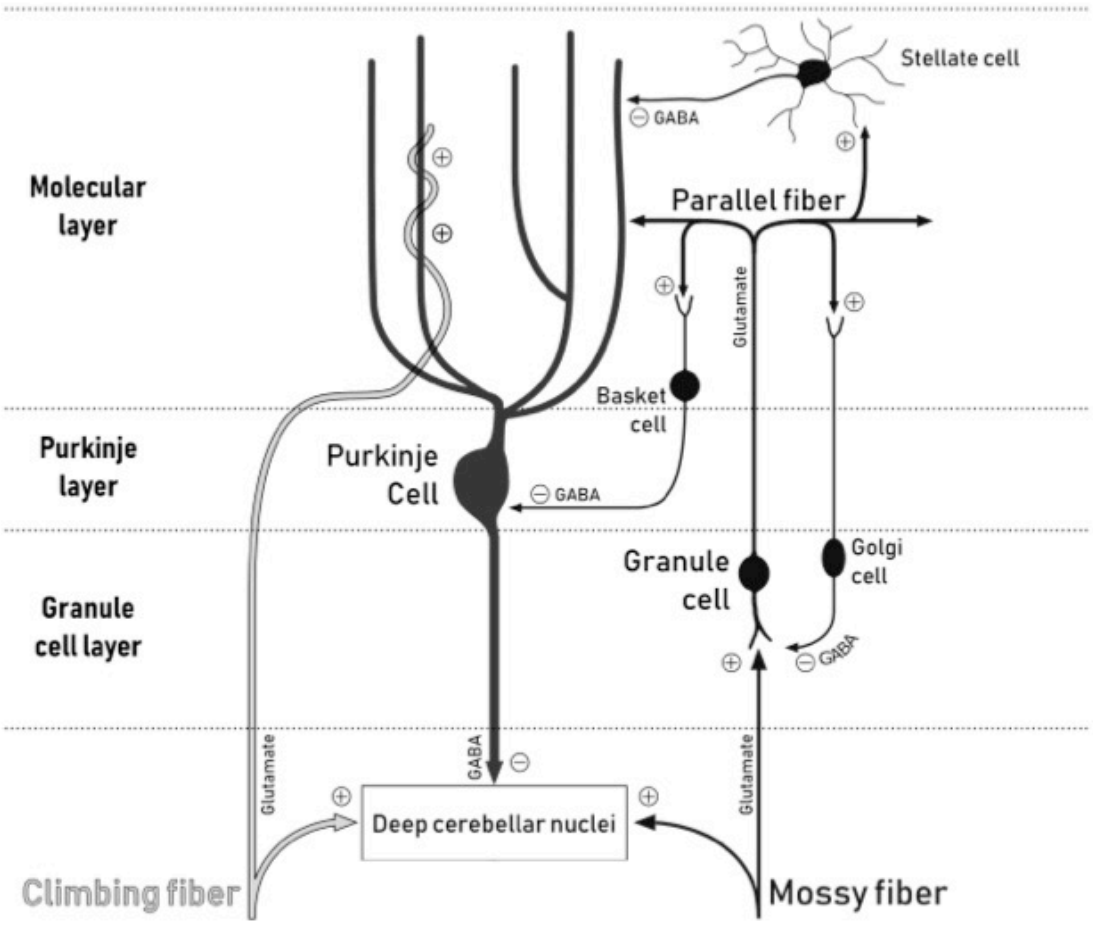

Figure 5: Schematic representation of the cerebellar circuitry.

Form a neurobiological standpoint, four out of the five cells in the cerebellar cortex (namely, the, basket, Golgi, stellate and Purkinje cells) contain the neurotransmitter gamma-aminobutyric acid

(GABA), which is the main inhibitory neurotransmitter in the central nervous system. Nevertheless, it is noteworthy to mention that other neurotransmitters besides GABA are present in the cerebellum, and specifically in the Golgi cells. Indeed, almost 70% of these cells also present glycine, whereas 5% of the Golgi cell population also shows the presence of choline acetyltransferase, which is the synthesizing enzyme for acetylcholine.

Given that Four out of the five cells in the cerebellar cortex show inhibitory functions, the granule cells, along with neurons of the afferent system (climbing and the mossy fibers) are the only cerebellar excitatory neurons. With particular reference to afferent fibers, several evidences indicate that glutamate is the main neurotransmitter of the mossy fibers. Nevertheless, there is debate regarding which molecule is used by the climbing fibers, with glutamate and aspartate that are the main candidates. Furthermore, a third type of afferent axons is also present along with climbing and the mossy fibers, called the aminergic fibers. These fibers contain biogenic amines and can be therefore divided into two different groups: the serotonin-containing axons (that originate from the raphe nuclei) and the norepinephrine-containing axons (originating from the locus ceruleus).

As previously described in the microscopic anatomy of the cerebellum (Chapter 1.1, page 8), the dendrites of the Purkinje cells in the molecular layer make synapses with the parallel fibers of the granule cells, receiving therefore indirect excitatory inputs from a large number of mossy fibers. Furthermore, the Purkinje cells also receive a direct modulatory input on their dendritic shafts from the climbing fibers, with each Purkinje cell that receives numerous synaptic contacts from a single climbing fiber. In doing so, the climbing fibers regulate the cerebellar function by modulating the effectiveness of the mossy fiber connection with the Purkinje cells

The Purkinje cells project in turn to the deep cerebellar nuclei. Given the GABAergic role of the Purkinje cells, the output of the cerebellar cortex is almost exclusively inhibitory. However, it has to be considered that virtually both climbing and mossy fibers provide collateral for the cerebellar nuclei on their way to the cerebellar cortex. For this reason, within the deep cerebellar nuclei is present a convergence of both extracerebellar excitatory and Purkinje inhibitory synapses over the

same projection neurons, although with a higher number of the latter synapses over the excitatory ones, reflecting in a significant influence over neuron firing.

The inhibitory activity of Purkinje cells is modulated by inputs from local circuit neurons occur on both the dendritic shafts and the cell body. The most powerful of these local inhibitory inputs the synapses made around the Purkinje cell bodies by the basket cells. These cells fire inhibitory GABAergic signals to the Purkinje cell, to inhibit its physiological GABAergic inhibitory activity over to the deep cerebellar nuclei, in order to facilitate motor coordination and therefore the execution of a movement. Additional modulations to the inhibitory activity arise from the stellate and the Golgi cells. In the molecular layer, the stellate cells are present and receive input from the parallel fibers, making direct synapse with the dendritic arbors of Purkinje cells and sending therefore direct inhibitory signals to this type of cells. On the other hand, in the same layer terminate the dendrites of the Golgi cells (while the body lays in the granular cell layer), that receive input from the parallel fibers and provide an inhibitory feedback to the cells of origin of the parallel fibers itself (the granular cell), therefore providing an indirect inhibitory activity somehow independent from direct synapses with Purkinje cells.

This basic circuit is repeated over and over in time, creating functional loops, being therefore the fundamental module of the cerebellum. Indeed, the modulation of signal flow through these modules provides the basis for the real-time regulation of movement, as well as the long-term changes in regulation that underlie motor learning.

1.3 Connections

1.3.1 Afferents

Cerebellar afferents are derived from three main sources: the cerebral cortex, the spinal cord, and the vestibular nerve, with only a small number of afferents that originate from the red nucleus and the tectum.

Regarding the afferents from the cerebral cortex, these projections establish synapses with three main brainstem structures: the pontine nuclei, the inferior olivary nucleus, and the reticular formation (Figure 6).

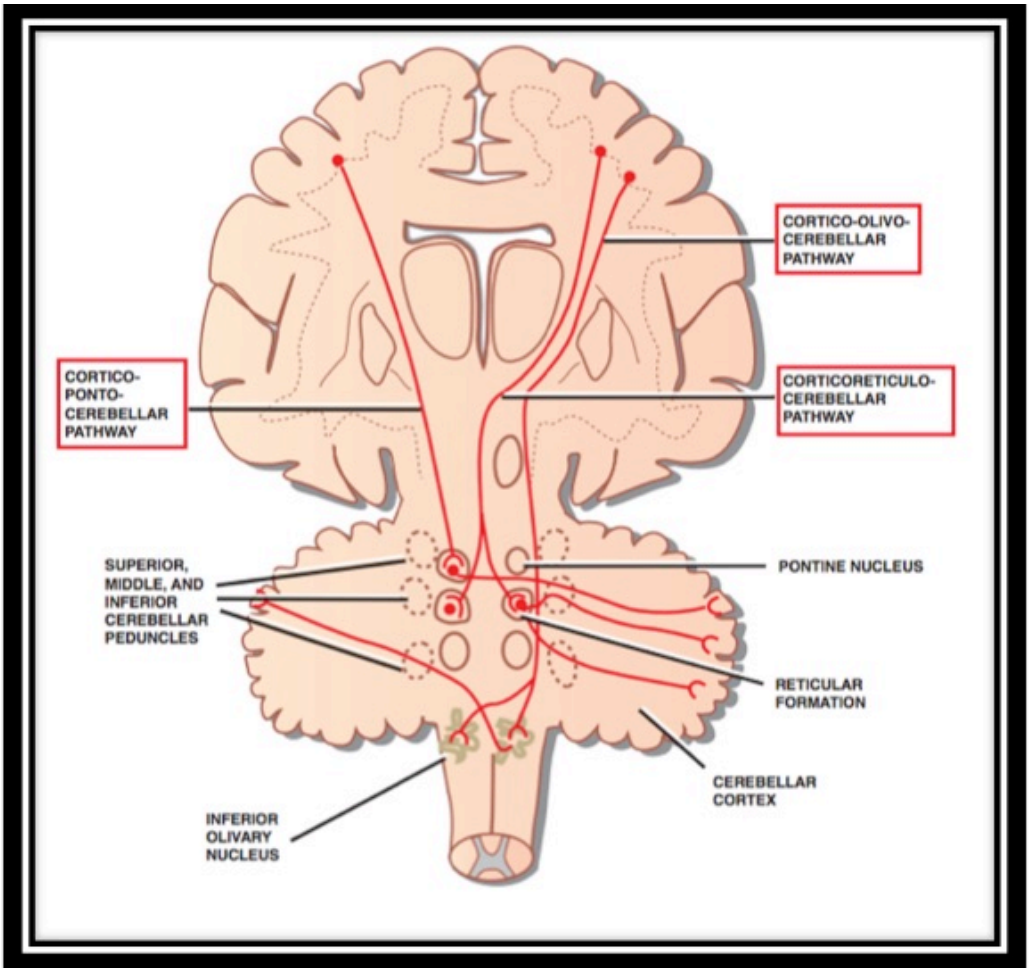

Figure 6: Schematic representation of the cerebellar afferents from the cerebral cortex (modified from (Alberstone, Steinmetz, Najm, & Benzel, 2009)).

The pontine nucleus serves as a major relay nucleus for projection axons arising from different areas of the cerebral cortex, and therefore serves for many functions such as visual-related information from cortical and subcortical structures or related to the upper motor neuron system. Indeed, many cerebral cortical areas are connected with the contralateral cerebellum through the pontine system, which therefore represent the largest group of mossy fibers that provide afferents to the cerebellum. Regarding the upper motor neuron system, the corticopontine fibers originate from layer V of the pyramidal cells, with axons descending from the cerebral cortex through the corona radiata and internal capsule to the brainstem, where they reach the longitudinal pontine fibers. The axons in this cerebro-ponto-cerebellar pathway leave the longitudinal fibers of the pons and make synapses with these ipsilateral pontine neuronal cell bodies, where axons that origin from these GM areas cross the midline, forming the transverse pontine fibers, finally entering the cerebellum via the contralateral middle peduncles to reach primarily to the folia the cerebellar hemisphere.

Another significant station providing afferents to the cerebellum is represented by the olivar nuclei. These nuclei are located in the ventrolateral portion of the caudal medulla, extending cranially to reach the caudal portion of the facial nucleus, while caudally they extend to reach the inferior portion of the obex. These structures receive information from a wide range of brain structures, conveying data to the cerebellar cortex from both the periphery (e.g. spinal cord, dorsal column nuclei, trigeminal and vestibular nuclei) and higher brain structures (e.g. red nucleus and cerebral cortex). Nevertheless, these afferences also reach the deep cerebellar nuclei, which provide fibers as a return route from the cerebellum to the inferior olive cells. Axons of the olivary nuclei neurons, activated by both ascending and descending neurons, cross the midline and join the contralateral inferior cerebellar peduncle, and represent the major source of the climbing fibers entering the cerebellum. These afferent fibers show a topographical organization, with each inferior olive fiber that sends one collateral to the deep cerebellar nuclei, and one to the cerebellar cortex that project to the same sector of the deep nuclei.

Finally, reticulocerebellar axons enter through the inferior cerebellar peduncle, with many different cell groups that are located within the reticular formation that provide origin to the mossy fibers. Indeed, the lateral reticular nucleus is not only the recipient of spinal afferents, but also receives a relevant amount of fibers from both the red nucleus and descending from the cerebral cortex. The fibers originating from the lateral portion of the reticular nucleus provide visual-related information from cortical and subcortical structures, and show a clear ipsilateral prevalence terminating mainly to vermian lobules VII and VIII. On the other hand, fibers originating from the paramedian portion of the reticular nucleus convey information from the somatosensory and frontal cortices mainly to vestibulocerebellar areas.

Regarding afferents from the spinal cord, these can be divided in three major spinocerebellar pathways: the ventral spinocerebellar tract, the dorsal spinocerebellar tract and the cuneocerebellar tract (Figure 7).

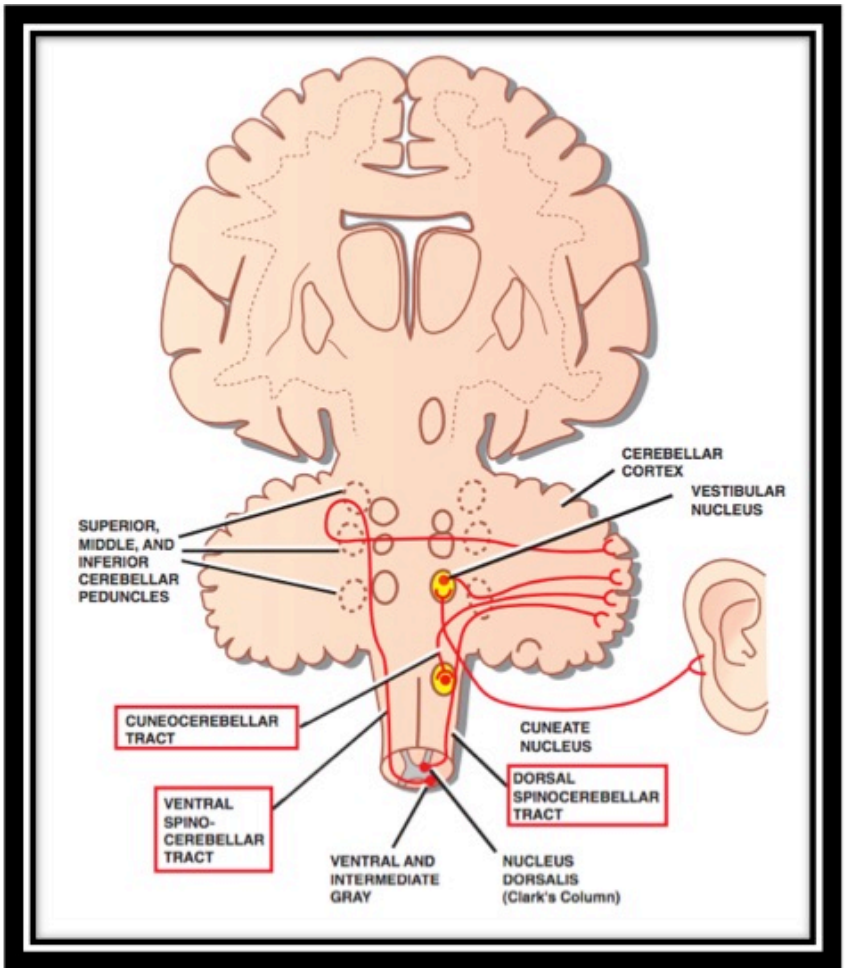

Figure 7: Schematic representation of the cerebellar afferents from the spinal cord and the vestibular nerve (modified from (Alberstone et al., 2009)).

The ventral spinocerebellar tract (historically known as Gowers' tract) carries mainly proprioceptive information from the lower limbs of one side of the body to the ipsilateral cerebellum, It originates from the ventral and intermediate GM of the spinal cord, and ascends bilaterally in the dorsolateral region of the lateral funiculus. A large portion of these fibers cross the midline as part of the anterior commissure and enter the cerebellum via the contralateral superior cerebellar peduncle, where it crosses a second time ("double cross"), provide collaterals to the globose and emboliform nuclei before terminating as mossy fiber in the cortex of the anterior lobe and vermis of the posterior lobe. Nevertheless, a small number of fibers uncross and remain ipsilateral in in its entirety.

The dorsal spinocerebellar tract (historically known as Flechsig's tract) also carries mainly proprioceptive information lower limbs of one side of the body, as well as part of that side of the trunk, to the ipsilateral cerebellum. Although it runs in parallel with fibers of the ventral spinocerebellar tract, most of its fibers are uncrossed. Indeed, originating from the nucleus dorsalis, the tract ascends bilaterally in the ventrolateral region of the lateral funiculus and enters the cerebellum via the inferior cerebellar peduncle, terminating as mossy fibers in the intermediate zone of the cerebellar cortex.

On the other hand, the cuneocerebellar tract convey mainly proprioceptive sensory information from the upper limb and upper part of the thorax and neck to the ipsilateral cerebellum, being an analogue of the dorsal spinocerebellar tract for the upper limbs. It originates in the accessory cuneate nucleus of the medulla and enters the cerebellar hemisphere via the inferior cerebellar peduncle.

Finally, regarding afferents from the vestibular nerve (Figure 7), it is noteworthy mentioning that the organization of the vestibulocerebellum is different from those previously described. Indeed, the labyrinth that sends direct primary afferents to the cerebellar cortex that passes through the inferior cerebellar peduncles to reach the ipsilateral flocculonodular lobe, to the folia of the cerebellar vermis or the adjacent paravermian areas. Along with these axons, a second-order fibers arising from the four vestibular nuclei are present, that are along with the deep cerebellar nuclei the only deep GM nuclei that receive Purkinje cell axons.

1.3.2 Efferents

The output system of the cerebellum is represented by the deep cerebellar nuclei, which receive massive projections from the Purkinje cells of the cerebellar cortex. These connections show a topographic organization, with a medio-lateral and antero-posterior arrangement. In particular, more medially Purkinje cells usually project to the medial nucleus, while the most lateral ones tend to project to the lateral nucleus. Similarly, axons from the anterior lobe projects to the more anterior sectors of the nuclei, with the ones originating from the posterior lobe that are directed to the more posterior sections. Nevertheless, this general arrangement is not consistently preserve and some divergence and convergence have been reported.

All cerebellar efferences convey through the inhibitory fibers of the Purkinje cells, with almost the entirety of these axons that terminate in the deep cerebellar nuclei, although a minor proportion continue over the cerebellar nuclei to synapse with the lateral vestibular nucleus in the medulla.

Efferents from deep cerebellar nuclei leave the cerebellum through mostly through the superior cerebellar peduncles, although few fibers pass through the inferior cerebellar peduncles, terminating in the following four destinations: the red nucleus and the thalamus, (via the superior cerebellar peduncles), and the vestibular complex and the reticular formation (through the inferior ones).

Regarding the efferences directed through the superior cerebellar peduncles to the red nucleus, axons originating from the globose and emboliform nuclei cross the midline in the ventral tegmental decussation at the level of the caudal colliculi and ascend to make synapses with the contralateral magnocellular portion of the red nucleus, which in turn projects fibers in the rubrospinal tract. Thus, projections from the globose and emboliform nuclei cross twice before reaching their destination, therefore influencing ipsilateral motor body activity, and in particular the flexor activity of the limbs (Figure 8).

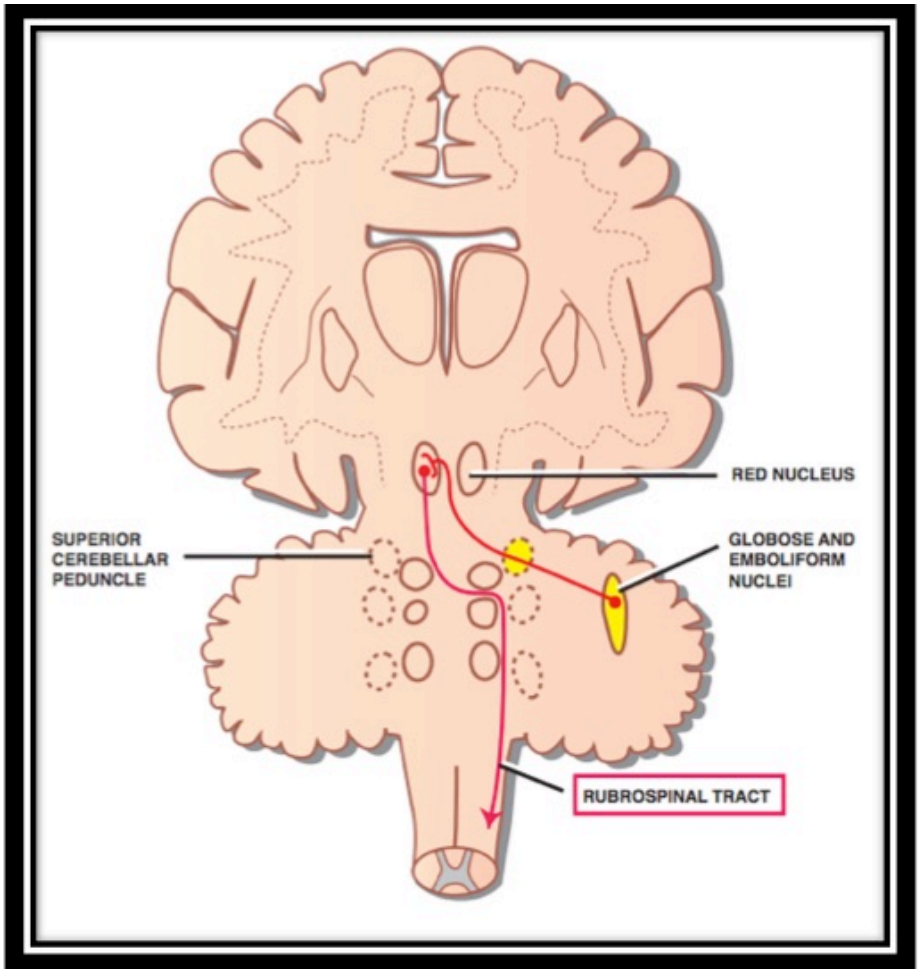

Figure 8: Schematic representation of the cerebellar efferents to the red nucleus (modified from (Alberstone et al., 2009)).

On the other hand, axons originating from the dentate nucleus can also reach, with a similar pathway and decussation, the contralateral red nucleus, although they reach in this case its parvicellular portion. Here, fibers descend directly via the central tegmental tract to reach the dorsal lamella of the inferior olivary nucleus. This last structure, as previously described, gives origin to the climbing fibers, thus this connection will reverberate the information to the cerebellum through these fibers. Indeed, decussating fibers arises from the inferior olivary nucleus, and pass through inferior cerebellar peduncle to reach the dentate nucleus where the fibers originally started, creating the dentatorubro-olivary tract. In this way, a closed dentatorubro-olivary functional loop is also created, that undergoes the name of triangle of Guillain-Mollaret (Figure 9).

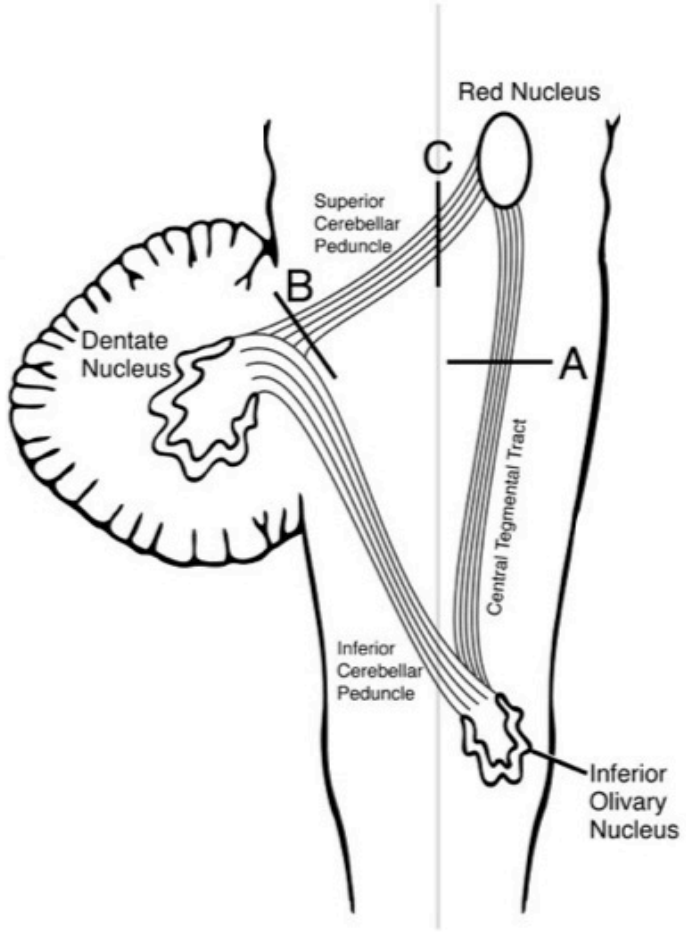

Figure 9: Schematic representation of triangle of Guillain-Mollaret (modified from (Gatlin, Wineman, Schlakman, Buciuc, & Khan, 2011)).

Efferents directed to the thalamus originate mostly from the dentate nucleus, with only a minor portion arising from the globose and emboliform nuclei. These fibers exit the cerebellum via the superior cerebellar peduncles, also cross the midline in the ventral tegmental decussation at the level of the caudal colliculi, and ascend to make synapses in the contralateral nuclei of the thalamus (mainly the ventro-lateral nucleus, with only a small contribution to the ventro-postero-lateral and centro-lateral nuclei). From these stations, axons projecting to the primary motor cortex arise, passing through the fibers of the internal capsule and the corona radiata. Therefore, DN efferents influences contralateral neurons of the primary motor cortex (Figure 10).

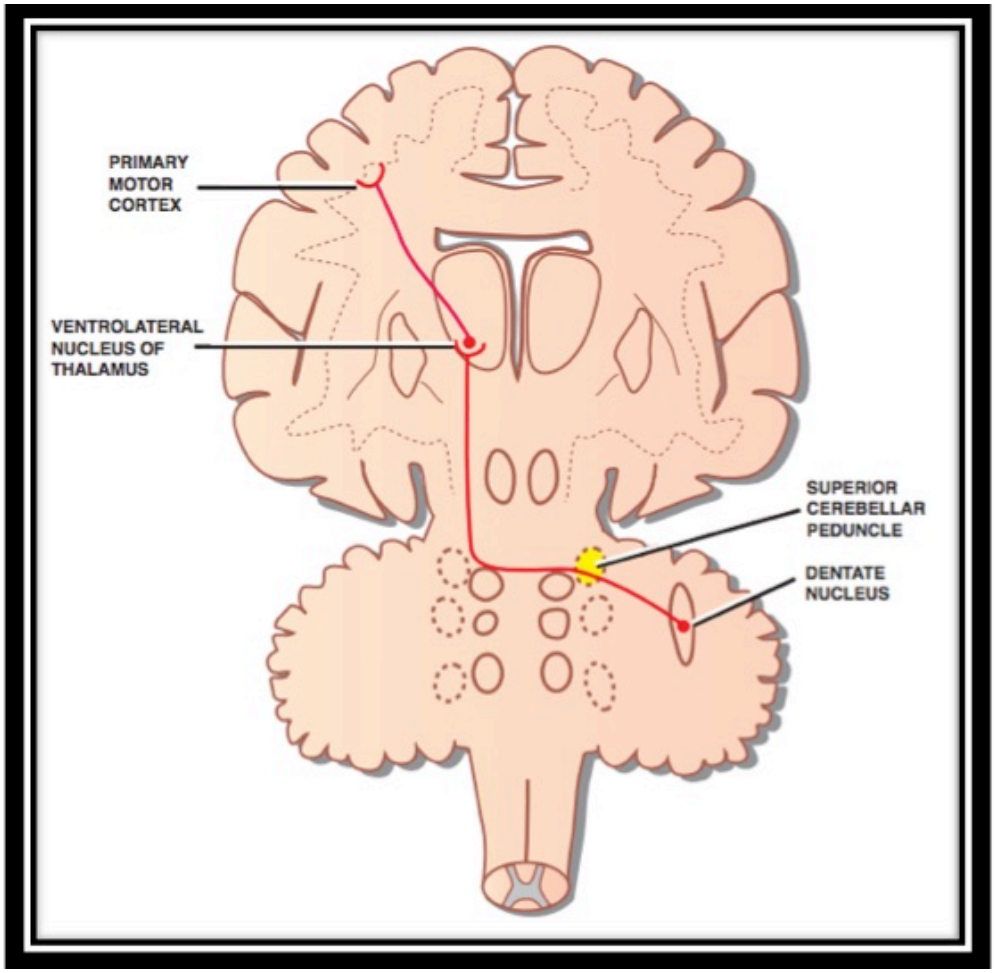

Figure 10: Schematic representation of the cerebellar efferents to the thalamus (modified from (Alberstone et al., 2009)).

Nevertheless, it has to be considered that the motor cortex projects descending motor fibers through the corticospinal tracts, that are know to decussate at the level of the pyramids. For this reason, the final effect is that neurons of the dentate nucleus influence ipsilateral motor activity and coordination.

Regarding efferents through the inferior cerebellar peduncles, axons originating from neurons of the fastigial nucleus exit the cerebellum through these structures and terminates caudally in the ipsilateral vestibular nucleus, along with a small number of Purkinje cell axons that project directly in the lateral vestibular nucleus (as previously briefly described), without being interposed in any deep cerebellar nuclei. From the lateral vestibular nucleus originate the descending vestibulospinal

tract. Therefore, efferents from the fastigial nucleus influence motor activity, by facilitating extensor muscle tone of the ipsilateral side of the body (Figure 11).

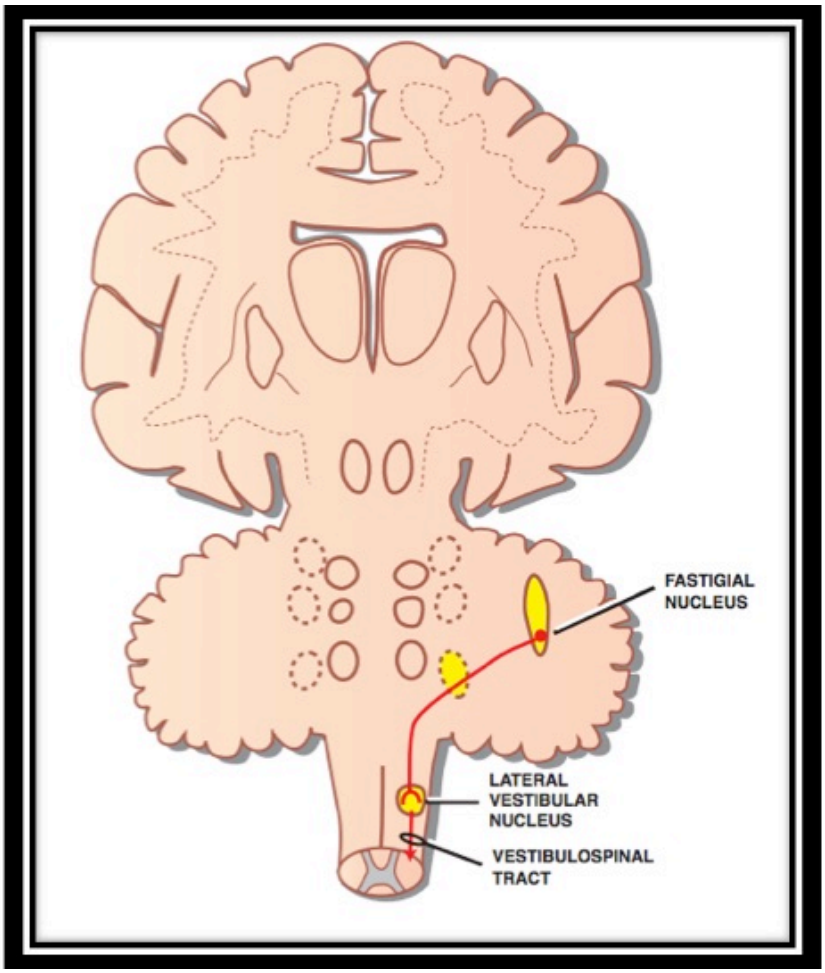

Figure 11: Schematic representation of the cerebellar efferents to the vestibular nucleus (modified from (Alberstone et al., 2009)).

Finally, some of the axons originating from the fastigial nucleus and exiting from the inferior cerebellar peduncles make synapses with the ipsilateral reticular formation, from which the reticulospinal tract arises. Fibers of this tract terminate on interneurons of the spinal GM, therefore influencing indirectly motor neurons through synaptic relays within the spinal cord.

CHAPTER 2

Magnetic Resonance Imaging

2.1 Volumetric analyses

2.1.1 Image segmentation

Every image is constituted by a finite set of elements called pixels in 2D images and voxels in 3D images (Figure 12).

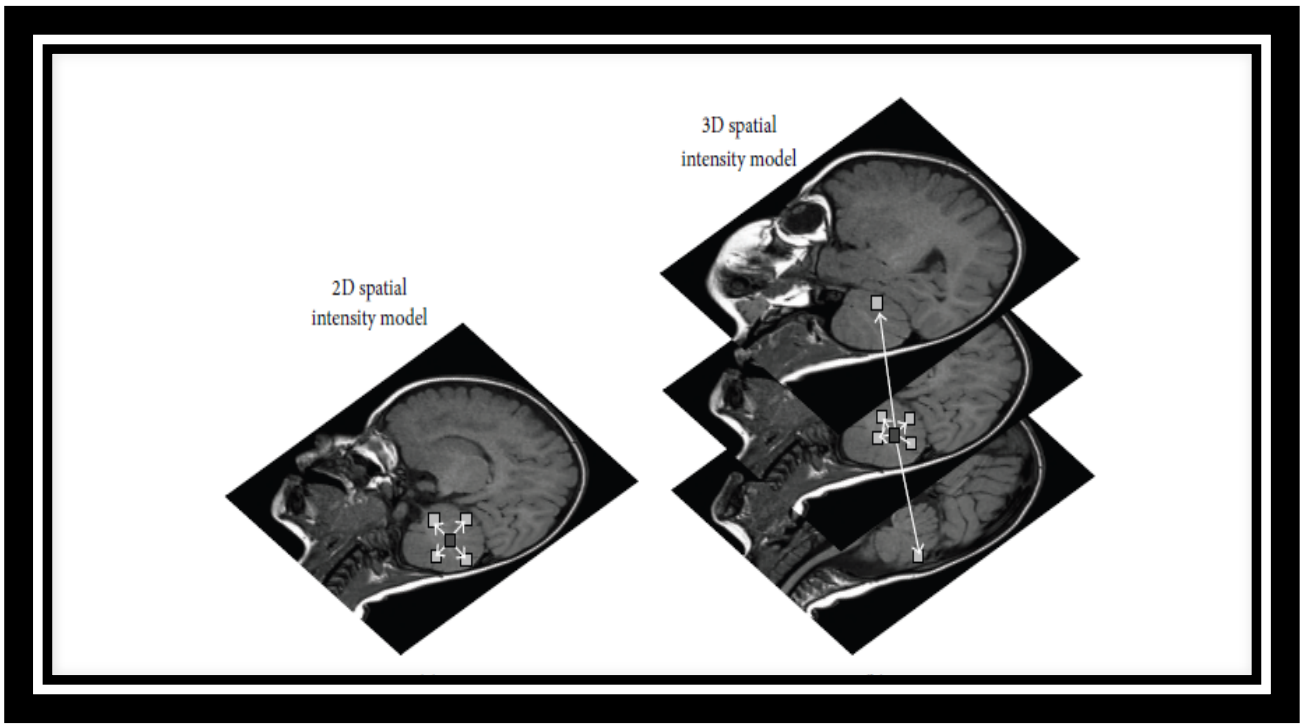

Figure 12: Example of 2D and 3D MR images (modified from (Despotović, Goossens, & Philips, 2015)).

To each of these elements is assigned a single value based on the resonance features of the tissue corresponding to that element. The size of the element defines the spatial resolution, which in turn determines the level of detail that can be appreciated in the image. Voxel size varies according to the sequence parameters, the magnetic field strength and other factors. The images used for brain

tissue segmentation in MRI have usually a voxel size equal or lower than 1x1x1mm^3. The image segmentation in its main components is carried out, on 3D volumetric images, on each individual slice, with a “slice-to-slice" technique. To properly understand image segmentation, some concepts need to be defined, including the spatial environment, the imaging features and the intensity distribution.

The concept of spatial environment and the information from neighboring regions is of utmost importance for MRI brain segmentation. In fact, the intensity of each voxel depends upon the signal intensity of neighboring regions’ voxels. The Markov Random Field (MRF) theory provides the basis to model the image local properties, as global brain properties depend on local interactions. MRF models have been successfully integrated in several MR brain segmentation methods to avoid misclassification errors induced by image noise (Pham, Xu, & Prince, 2000; Zhang, Brady, & Smith, 2001).

Image features can be defined as object/structure distinctive elements. The segmentation result depends on an appropriate selection and extraction of relevant features. Typically, in MR a statistical approach is used to classify the relevant features of a tissue. Such features are based on first and second order statistics of grey intensity.

First order feature derive from the histogram of the gray value of the image, and include intensity, mean, median and standard deviation of the values within each pixel. As these metrics do not contain any information on the spatial distribution of the pixel values, they are usually combined with second order features, used to describe the image texture, which are usually computed via a co-occurrence matrix of grey levels (Haralick, Shanmugam, & Dinstein, 1973). Finally, it has to be noted that brain tissue intensity is one of the most relevant features for segmentation. However, when intensity values are not reliable, as a consequence of artifacts such as the image noise, the partial volume effect (PVE) or the effect of the polarization field, the segmentation algorithm based on intensity might incur in tissue misclassification. In order to overcome this issue, a preliminary preprocessing of the image is often required, with the application of specific steps detailed below.

BiasField correction and Brain Extraction (removal of non-brain tissue) represent the two main preprocessing steps required prior to the application of different segmentation algorithm, in order to obtain image segmentation in GM, WM and cerebrospinal fluid (CSF). The polarization field (BiasField), also called intensity inhomogeneity, is a low frequency MR artifact, spatially inconstant, that causes a slight variation of the signal intensity within tissues that share the same physical properties. The polarization field is generated by the spatial inhomogeneity of the magnetic field, by variations in the receiving coil sensitivity end by the interaction between the magnetic field and the body. The Bias Field also depends upon the strength of the magnetic field, with a direct linear relationship. Indeed, when the images are acquired at low field (i.e. 0.5 T), the Bias Field is almost invisible and can be overlooked. This does not hold true when the images are acquired at higher magnetic field (e.g. 1.5T or higher). In fact, in this case, the polarization field notably influences the analysis. To overcome this issue, several segmentation algorithms have been proposed that model and estimate the Bias Field in an iterative process (Ashburner & Friston, 2005; Pohl, Fisher, Grimson, Kikinis, & Wells, 2006; Zhang et al., 2001). Alternatively, the polarization field can be estimated and the image corrected before further processing steps are conducted (Sled, Zijdenbos, & Evans, 1998).

During the acquisition of the brain volume, also non-brain tissues are imaged (i.e. skin, fat, bone, meninges). The intensity of these tissues might overlap with the brain tissue intensity, determining misclassification errors, and overestimation of some tissues. Therefore, it is advisable to remove these tissues from the considered volume, extracting only brain tissue before applying segmentation algorithms.

This step, called Brain Extraction, is preliminarily conducted classifying each voxel as pertaining (“brain”) or not pertaining (“not brain”) to brain tissue, and removing those not belonging to the parenchyma. The result of brain extraction is an image containing only "brain" voxels (GM, with matter and CSF).

An example of the described preprocessing steps is provided in Figure 13.

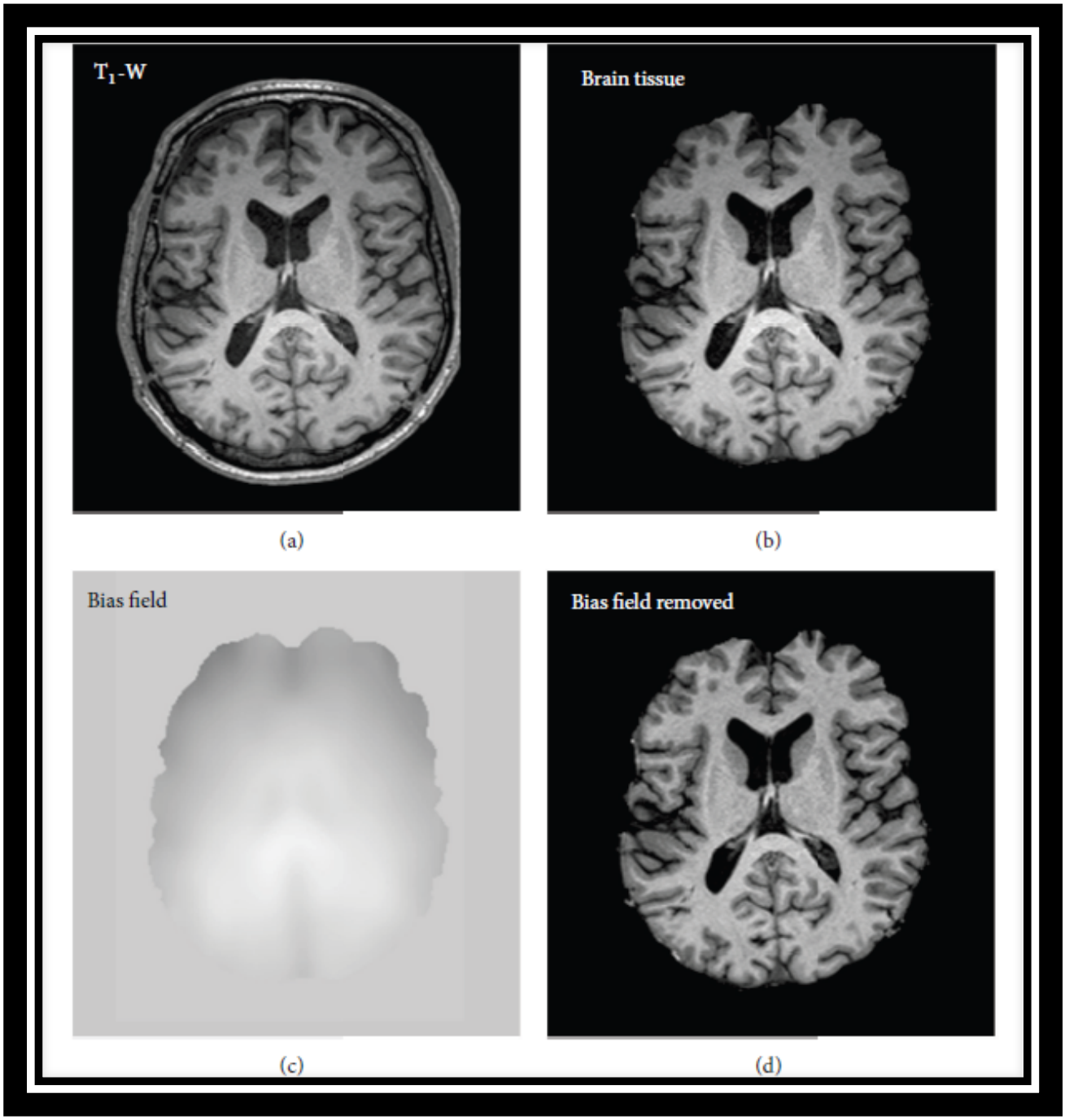

Figure 13: Brain MR preprocessing steps: (a) native T1-weighted volume (b) results of the Brain Extraction; (c) Bias Field correction; (d) final image obtained after skull-stripping and bias correction (modified from (Despotović et al., 2015)).

Regarding the segmentation techniques, the model assumption is that MR images are constituted by a finite number of distinct tissue types (cluster) composed by a finite number of voxels. The voxel

intensity of each voxel pertaining to each cluster are distributed according to a normal distribution, that can be described by a mean, a median, a variance and by the number of voxels which are part of the distribution.

Since the images are referred to a known stereotaxic space, the a priori probability of each voxel to belong to GM, WM or CSF is also known. This information is stored in probability images (provided by the Montreal Neurological Institute – MNI (Evans et al., 1992)), obtained from brain volumes acquisitions from 152 healthy controls (HC). These probability images contain values ranging from 0 to 1, which represent the a priori probability for each voxel to belong to one of the three classes (GM, WM or CSF) after the image normalization to the same space. Before segmentation, the images are therefore registered to the a priori probability images via an affine registration. After the registration, an iterative algorithm is applied, starting from the allocation of initial estimates for the different parameters. The initial estimate for the modulation field is usually homogeneous, and is based on the probability images previously described. Every subsequent iteration allows the estimation of cluster parameters obtained on the native images (not corrected for bias field) and the allocation of each tissue to a certain class (attributing a probability value to each class). The algorithm is then reiterated, recomputing the probability that the specific tissue was correctly classified. At each iteration, the parameters describing the distributions reach a better adaptation and the probability expressing tissue classification slightly change to reflect the new distributions. This process is iterated until the convergence criteria are met. Parameters describing clusters corresponding to the a priori probability images tend to converge faster than the others, due to the better initial estimates. The final classification values are comprised between 0 and 1, with the majority if the values being close to one of the two extremes.

An example of brain segmentation in its three main components is shown in Figure 14.

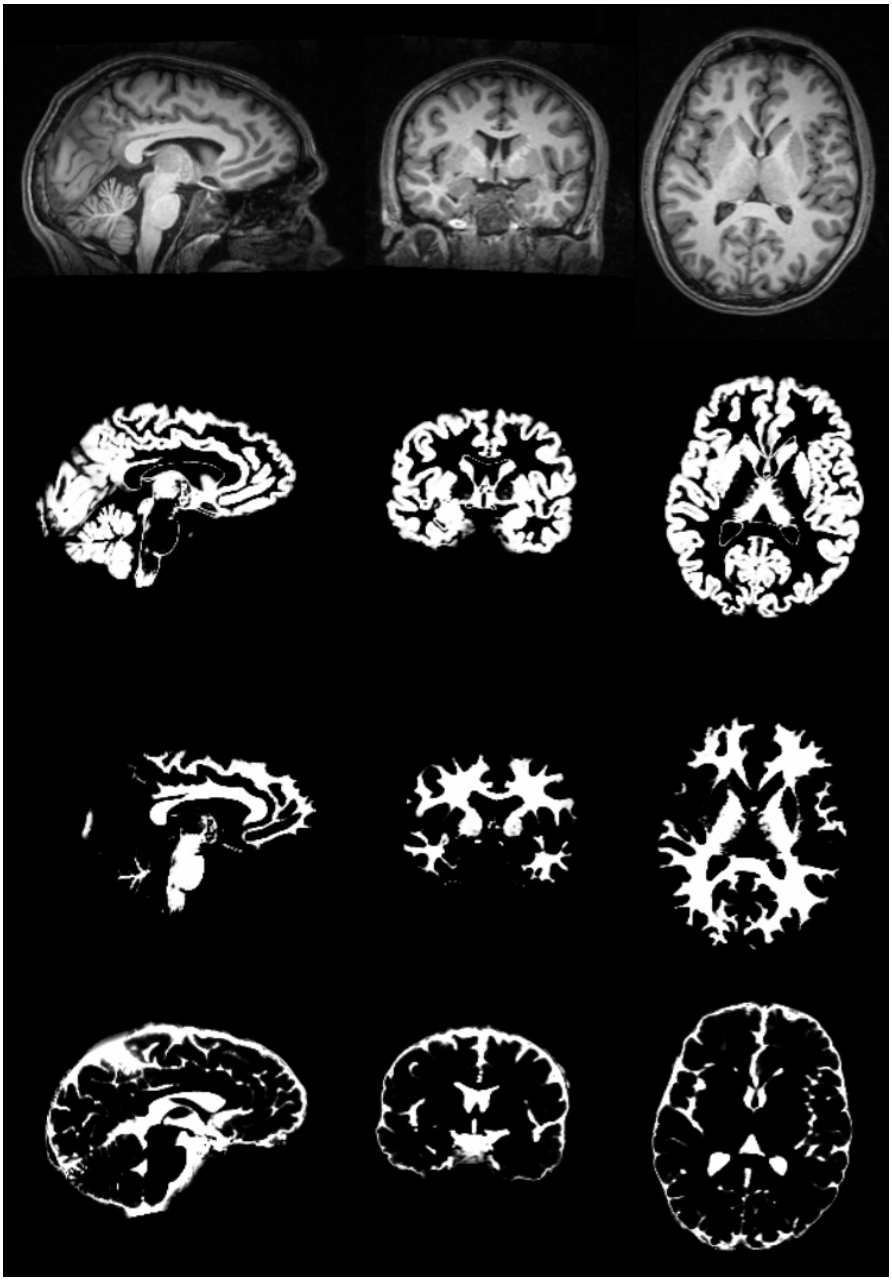

Figure 14: Segmentation of a brain volume (in the native space, first row) in its three main components: GM (second row), WM (third row) e CSF (last row).

2.1.2 Voxel based morphometry

Voxel Based Morphometry (VBM) is an advanced MRI technique that allows the between-group comparison of grey matter local concentration (Ashburner & Friston, 2000). More specifically, VBM is a fully automated morphometric technique that, comparing voxel-wise T1 weighted images, is able to identify local structural abnormalities, e.g. minimal differences in grey matter density that are not detectable with a qualitative evaluation of MR images with conventional techniques. Of note, VBM density does not refer to the cellular density measured by cytoarchitectonic methods. The VBM procedure requires the spatial normalization of all images to the same stereotaxic space, the isolation of grey matter from normalized images through a segmentation procedure and finally the execution of a statistical analysis to localize and analyze differences in grey matter concentration (which is function of the volume) between groups. The final result of this processing is a statistical parametric map that shows regions with statistically different grey matter concentration between the compared groups (Figure 15).

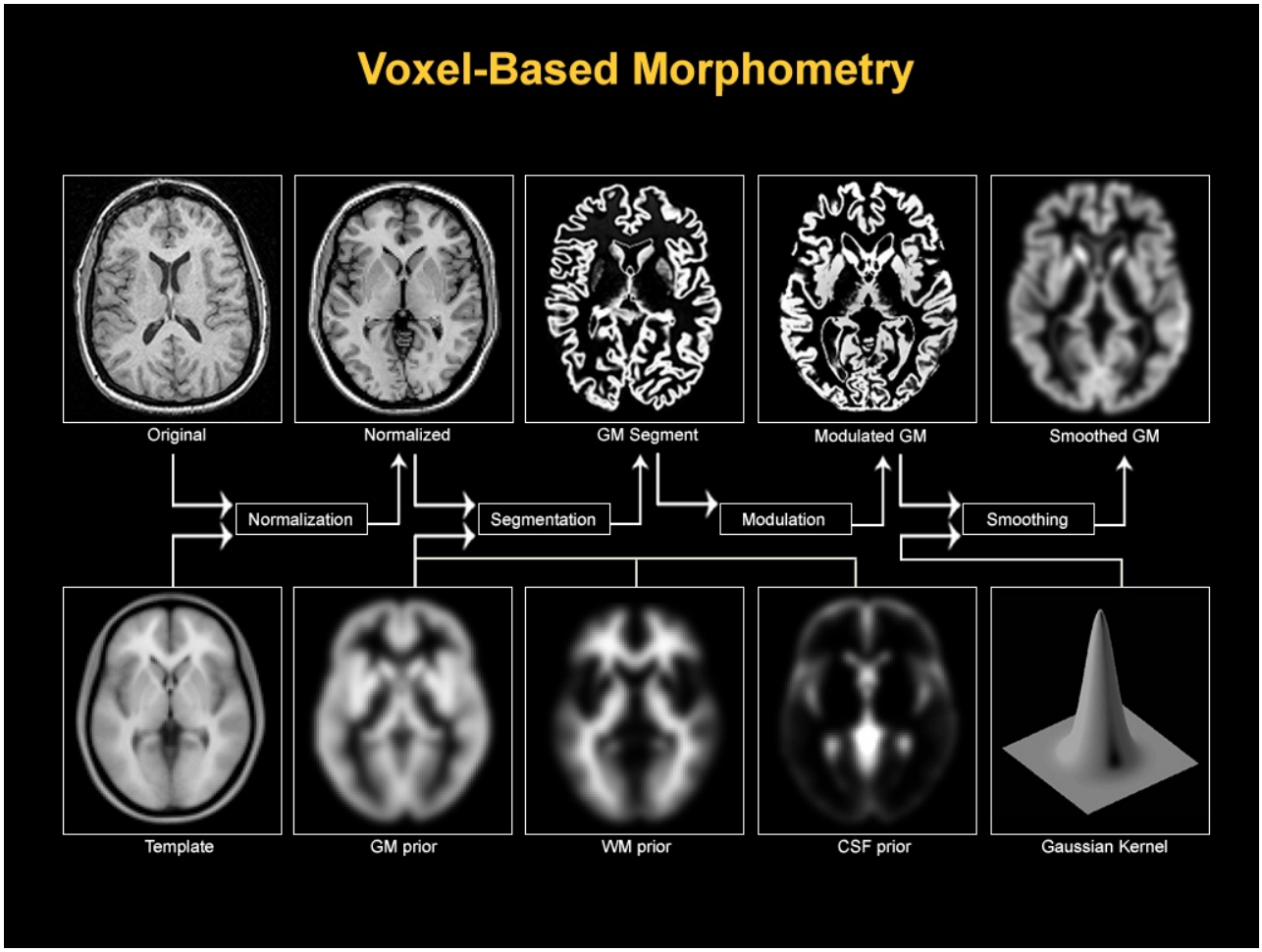

Figure 15: Schematic representation of the VBM processing (modified from (Matsunari et al., 2007)).

The spatial normalization step achieves the transformation of individual MR images to the same stereotaxic space, in order to correct global differences in size and shape of different brains and thus allow the between-group comparison. Typically, spatial normalization requires not only image translation and rotation but also nonlinear warping, to minimize individual regional anatomic variations by registering individual brains to a standard brain template such as the Talairach-Tournoux or the MNI. In the first step of spatial normalization, affine transformation parameters are computed to allow modifications in global dimensions and location of the brain volume, through linear deformations along the 3 axes (Ashburner & Friston, 1997). In the second step parameters of elastic deformation are computed, in order to account for differences in shape between individual brains and the reference brain. Applying nonlinear transformations, the correspondence between

each anatomical structure of individual brains and the template brain is achieved (Ashburner & Friston, 1999). Given the impact of spatial normalization on the following steps of the analysis, the choice of an adequate template is of paramount importance.

The segmentation procedure allows the classification and isolation of specific components of an MR image. In the VBM processing, normalized images are segmented in GM, WM and CSF. More specifically, each voxel is attributed a probability to belong to a specific tissue class and segmented accordingly based on its intensity and spatial location (i.e. a voxel is segmented as GM if it shows an high probability to belong to a region were GM is expected on the basis of the reference template and if it has a signal compatible with GM) (Ashburner & Friston, 2005).

Following segmentation the images are modulated in order to preserve local volumes. In fact, as the normalization procedure induces compressions and expansions within the image, possibly modifying the GM local concentration, a modulation step, based on the Jacobian determinants derived from the normalization step, is required to correct the intensity value of each voxel according to the modifications undergone during normalization.

Finally, normalized and modulated images undergo a smoothing step where the absolute value of each voxel is substituted with the mean value of its neighboring voxels, in order to increase the signal to noise ratio and reduce the impact of normalization errors. Smoothing is usually achieved via image convolution with a Gaussian function with amplitude of 4 to 6mm FWHM (Full Width at Half Maximum – a measure of the image resolution degradation induced by smoothing, which is equal to the Gaussian function amplitude measured at half of its maximum value).

The statistical analysis is conducted applying voxel by voxel the general linear model (GLM) (Friston et al., 1995), thus performing an analysis of covariance that accounts for covariates of no interest that could affect the result (e.g. age or sex). The analysis is then corrected for multiple comparisons (deriving from the number of voxels constituting the brain volume) with techniques that account for the image resolution, in order to limit the significance loss induced by such

corrections (with the most used technique based on the Gaussian field theory) (Worsley et al., 1996).

These techniques are specifically suited for the simultaneous analysis of huge number of comparisons (i.e. the hundred thousands of voxels the constitute the GM volume), as they allows a local correction for multiple comparisons, whereas a correction based on all the voxels of the considered volume (i.e. a Bonferroni correction) would set an unreasonably high threshold.

All the above-mentioned techniques are implemented in different software, such as the Statistical Parametric Mapping software (http://www.fil.ion.ucl.ac.uk/spm).

2.1.3 Cerebellar segmentation methods

Manual segmentation of the cerebellum, although still considered as the gold-standard procedure, has several problems, including but not limited to being a very slow and error-prone procedure, with consistency between operators that is also difficult to achieve (Cardenas et al., 2014).

In the literature, different approaches have been described to segment the cerebellum. However, among the fully automated and publicly available methods to segment the MRI images of the cerebellum, only few software provide a parcellation of cerebellar lobules, which are here listed and briefly described.

One of the most widely used approaches in literature is the Spatially Unbiased InfraTentorial (SUIT) method (http://www.diedrichsenlab.org/imaging/suit.htm). This is a toolbox working under the SPM software, based on global segmentation and isolation of the cerebellum-brainstem tissues using priors on their spatial distribution at low resolution, followed by nonlinear coregistrations of input MRI images to a $1mm^3$ isotropic cerebellar atlas (Figure 16).

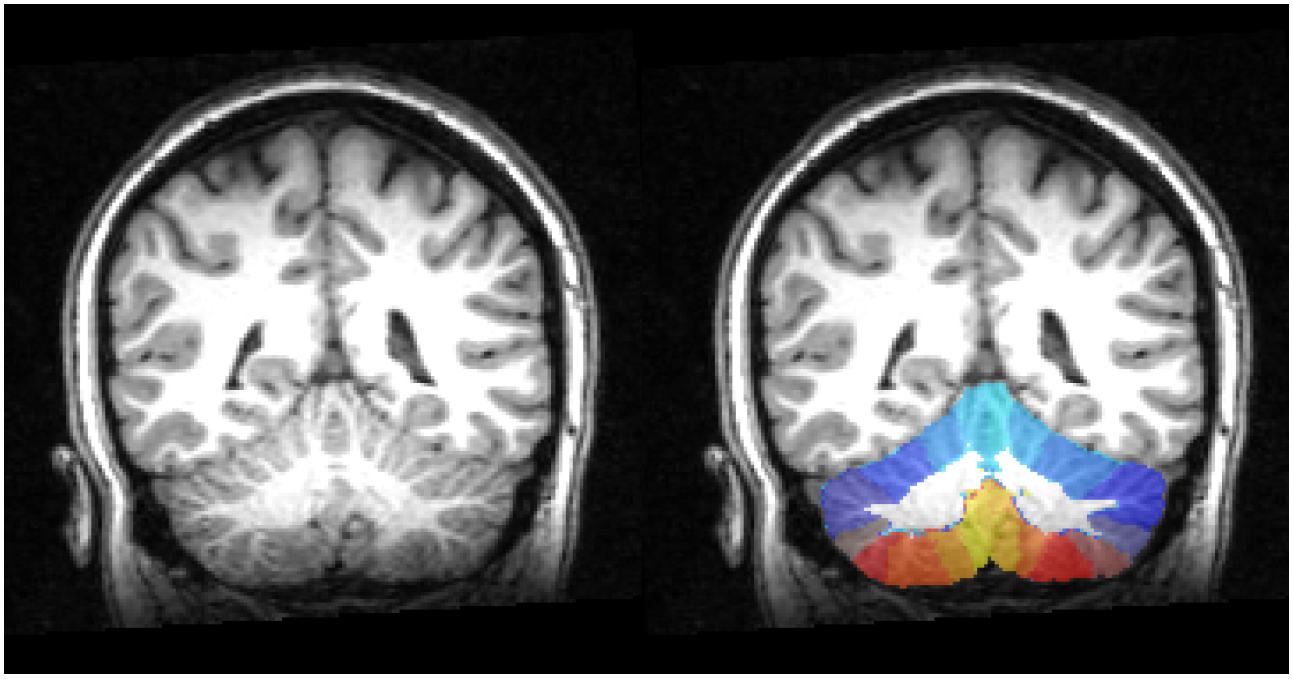

Figure 16: Application of the SUIT pipeline to obtain cerebellar lobule volumes in a 43 years old healthy subject.

SUIT, which is specifically designed to process standard resolution dataset acquired at 3T MRI, has been widely used to study cerebellar involvement in several neurological disorders such as neurodegenerative, neuroinflammatory and psychiatric disorders (Cierpka et al., 2017; Cocozza et al., 2017; D'Mello, Crocetti, Mostofsky, & Stoodley, 2015; O'Callaghan et al., 2016; Wolf et al., 2015).

On the other hand, another approach that has been used in literature is the cerebellar segmentation obtained from FreeSurfer (http://surfer.nmr.mgh.harvard.edu/). This software assigns a neuroanatomical label automatically to each voxel of an individual MRI volume based on probabilistic information estimated from a manually labeled training set. The procedure is relatively time consuming (more than 10 hours per subject), requiring manual editing to correct the volume-based stream outputs.

Noteworthy to be mentioned is the cerebellum parcellation obtained with the Convolutional Neural Networks (CNN) approach (http://www.iacl.ece.jhu.edu/index.php/Cerebellum_CNN), which is based on learning a set of nonlinear filters producing feature maps of local to global information to segment the image. This segmentation procedure, validated on five 1 mm isotropic images acquired at 3T, uses first a locating network to predict a bounding box around the cerebellum, then a parcellating network to parcellate the cropped-out cerebellum.

On the other hand, the CEREbellum SEgmentation (CERES) method (https://volbrain.upv.es/index.php) consists of a multiatlas patch-based nonlocal label fusion technique that produces segmentations using a library of manually annotated cases. Nevertheless, the method scripts are not publicly available, with images that can be processed only via a web interface that can process a very limited number of dataset (10 dataset per day and per user). Furthermore, the method has been validated only on $1mm^3$ isotropic images acquired on 1.5T scanners

The Multiple automatically Generated Templates (MaGeT) brain segmentation algorithm (http://cobralab.ca/software/MAGeTbrain/) produces lobular parcellation using a multiatlas voting procedure based on a template library generated from the input images Despite a high accuracy, especially compared to other algorithms, **t**his method is very time consuming, due to its use of multiple nonlinear registrations. Furthermore, as for CERES, the method has been validated only on 1 mm isotropic images acquired on 1.5T scanners

Finally, the Rapid Automatic Segmentation of the human Cerebellum And its Lobules (RASCAL) (Weier, Fonov, Lavoie, Doyon, & Collins, 2014) approach has to be mentioned, which combines patch-based label-fusion and a template library of manually labeled cerebella obtained from 16 HC.

2.2 Functional MRI

2.2.1 Principles

Functional Magnetic Resonance Imaging (fMRI) is an MRI technique that indirectly measures brain activity through the detection of modifications in the cerebral blood flow (CBF), allowing the investigation of anatomical structures activated during the execution of specific tasks or following the application of a specific stimulus. The theoretical basis of fMRI relays in the neurovascular coupling, (i.e. the relationship between local neural activity and subsequent changes in CBF).

In normal conditions, CBF is 750-1000 ml/min, with higher distribution (4x) in the grey matter than in the WM (Kandel, Schwartz, Jessell, Siegelbaum, & Hudspeth, 2012). Brain function depends upon a steady supply of glucose through the blood flow and therefore glucose consumption, with secondary oxygen consumption, represents a valuable index of brain activity (Phelps et al., 1979). In 1986, through the application of nuclear medicine techniques, Fox and Raichle described how CBF glucose consumption was followed by a non-proportional increase in oxygen consumption (P. T. Fox & Raichle, 1986). Subsequently it has been shown how deoxyhemoglobin concentration depends upon oxygen consumption but also brain volume and CBF velocity. Specifically, a CBF increase following an increase in CBF velocity determines a sensible reduction in neuronal oxygen extraction, inducing a reduction in deoxyhemoglobin concentration (Bereczki et al., 1993; Villringer, Them, Lindauer, Einhäupl, & Dirnagl, 1994).

The CBF increase not associated to a parallel increase in oxygen extraction causes an increase in oxyhemoglobin concentration and a relative reduction in deoxyhemoglobin concentration (Kato, Kamei, Takashima, & Ozaki, 1993; Malonek & Grinvald, 1996; Meek et al., 1995). Modifications of deoxyhemoglobin concentration represent the physiological basis of fMRI (Ogawa et al., 1992) (Figure 17).

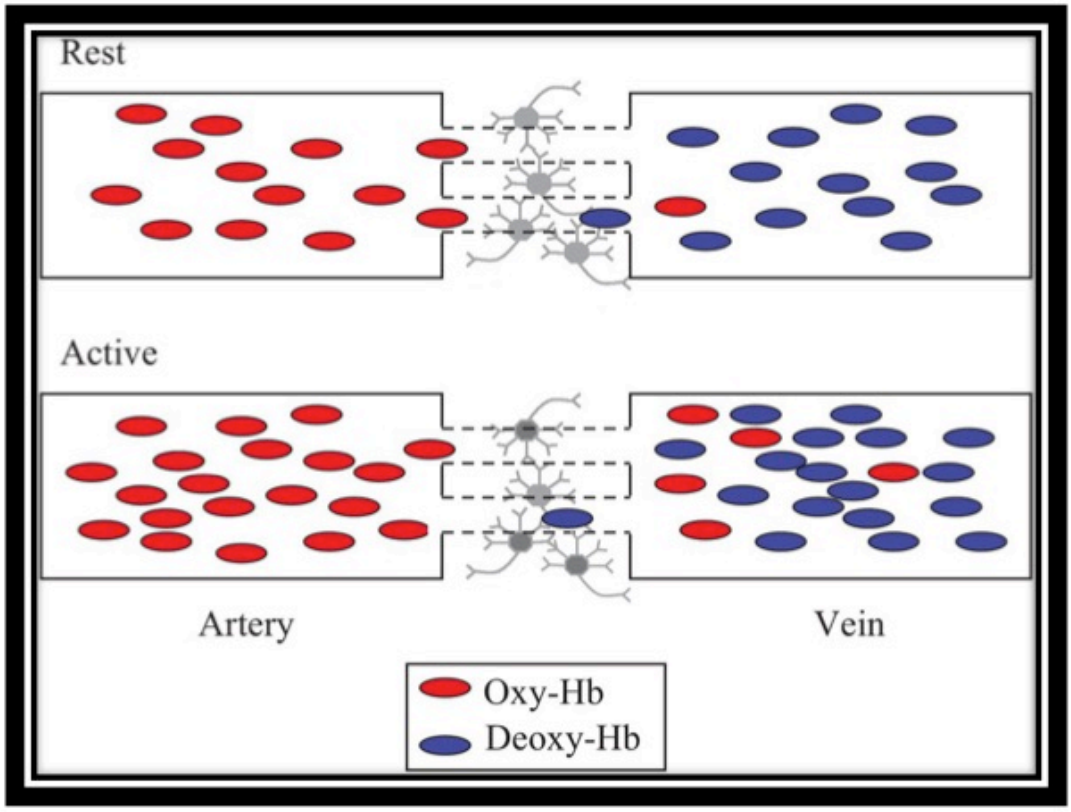

Figure 17: Schematic representation of microvascular cerebral blood flow modifications in response to a task (modified from (McRobbie, Moore, Graves, & Prince, 2017))

fMRI contrast is based on the BOLD (Blood Oxygen Level Dependent) effect. BOLD contrast derives from variations in the magnetic susceptibility of blood due to variations in the concentration of deoxyhemoglobin secondary to brain activity. The first description of the BOLD effect dates back to 1990, when Ogawa analyzed murine brain at high magnetic field after the inhalation of oxygen 100% and after the inhalation of a mixture of oxygen and carbon dioxide 10%. Ogawa described how, after the inhalation of pure oxygen, a strong natural contrast could be detected in the brains as hypointense striae in the vicinity of veins, which were not detectable after the inhalation of the mixture containing carbon dioxide. Carbone dioxide, in fact, by inducing vasodilation, was determining an increase in CBF, a reduction in deoxyhemoglobin concentration and therefore a modification of the magnetic field. Ogawa named this phenomenon BOLD effect (Ogawa, Lee, Kay, & Tank, 1990; Ogawa et al., 1992). Following these first description in the rat brain, the

BOLD effect was tested and confirmed in humans (Bandettini, Wong, Hinks, Tikofsky, & Hyde, 1992; Kwong et al., 1992).

As previously described, the modifications in the magnetic field responsible for the BOLD effect are driven by deoxyhemoglobin paramagnetic properties (Pauling & Coryell, 1936), which, in turn, depend upon its molecular structure. Indeed, the iron molecules that are part of deoxyhemoglobin composition present 4 electrons on their most external orbital, conferring to the molecule a high spin state that explains its behavior of paramagnetic agent. Considering its paramagnetic properties, it follows that the relative reduction in deoxyhemoglobin concentration determines a reduction of the magnetic field inhomogeneity, with consequent increase of the T2* signal intensity, which is highly sensitive to field inhomogeneity. In summary, CBF modifications indirectly induce magnetic field perturbations that modify the natural contrast of fMRI images (Boxerman, Hamberg, Rosen, & Weisskoff, 1995; Kennan, Zhong, & Gore, 1994; Yablonskiy & Haacke, 1994).

2.2.2 fMRI data analysis methods

From a technical standpoint, the image acquisition relies on T2* weighted echo planar sequences (gradient echo sequences in which every section is acquired independently using a single echo train or single shot), with most of the scanners that are able to obtain a single volume with a slice thickness of approximately 3mm in 20-30ms (S. Chen & Li, 2012).

The choice of echo planar imaging for fMRI relies on the following considerations:

i) the signal to noise ratio is directly proportional to the acquisition time (and therefore the temporal resolution) and to the voxel size (and therefore the spatial resolution)

ii) the BOLD signal has a latency of about 3 seconds with respect to the brain activation, and an intensity lasting about 10 seconds, with a peak at 5-6 seconds.

For this last reason, in order to analyze events occurring while the BOLD signal is detectable, it is necessary to minimize the image acquisition time. To achieve an increase in temporal resolution, which is the main limiting factor in an fMRI analysis, it is necessary to trade off spatial resolution. This translates in an increase in voxel size, in order to maintain the signal to noise ratio within reasonable values. The signal to noise ratio issue could also be solved increasing the magnetic field (i.e. 7T scanners), which would allow the acquisition of images with high temporal resolution without compromising the spatial resolution (Shmuel, Yacoub, Chaimow, Logothetis, & Ugurbil, 2007).

In order to evaluate modifications induced by the execution of a task, the fMRI sequence acquires brain volumes for its entire duration. During the acquisition the subject is asked to alternate active periods (i.e. the task execution) and rest periods during which no task is executed (Glover, 2011).

Theoretically, this acquisition technique would allow the direct comparison of the images acquired under the two conditions (task execution and rest) to evaluate brain areas undergoing activation. Unfortunately this is not possible as the BOLD effect induces slight signal variations (about 1%), which are further masks by the images intrinsic noise (related to physiological – head movements,

breath related movements, heart beat – and technical factors) (Birn, Smith, Jones, & Bandettini, 2008; Chang & Glover, 2009).

For this reason, the acquired images require the application of specific processing steps, with the aim to reduce the images intrinsic noise and optimize temporal and spatial resolution (Bandettini et al., 1992). Specifically, when we model the data at each voxel we assume that all of the slices were acquired simultaneously. As this is not the case, and the delta between the acquisition time of the first and last slice can be up to 2 seconds, in the first step of the fMRI processing the time-series for each slice are shifted back in time by the duration it took to acquire that slice, through temporal interpolation of adjacent time points.

Afterwards, in order to remove the confounding effects introduced by the subject head movements, each volume is spatially registered to the exam's first time point, through a rigid-body volume registration, which applies rotation and translation parameters obtained for the three main axes to overlay the two volumes (Cox & Jesmanowicz, 1999). Temporally and spatially normalized images are then despiked, substituting outlier values within the image with the mean voxel value computed from all the exam's acquisitions, in order to remove artifacts. The despiked images are then spatially smoothed via Gaussian function and filtered with the application of high-band low-band filters. The high-band filter removes signal variations that are too slow, such as those induced by non-physiologic phenomena such as temperature variations in the scanner room, while the low-pass filter removes variations in the signal that are to fast, related for example to the cardio-respiratory cycle. Finally, a mean of all volumes is computed. From this mean image are estimated the coregistration and deformation parameters necessary to normalize and overlay the volume to the MNI template provided in SPM (Ashburner & Friston, 1999). The fMRI normalized volume means undergo a smoothing step with a Gaussian convolution matrix (usually with a 6 or 8mm FWHM) to compute a local EPI template which represents the reference for time series normalization.

fMRI techniques, originally developed to explore the activation of specific brain regions following a stimulus or during the execution of a task, have been more widely applied to investigate

functional connections between brain regions. Indeed, the brain is functionally composed by networks of interconnected areas that can be characterized thanks to fMRI.

Functional connectivity can be defined as the synchronous activation of brain areas not directly interconnected (Aertsen, Gerstein, Habib, & Palm, 1989), and can be explored analyzing the temporal variation (Time-Activity Curve - TAC) of the BOLD signal in a brain area ("seed") rather than the temporal evolution of the executed task or the administered stimulus. Time-activity curves present time on the x-axis and signal intensity on y-axis, allowing the estimation of the degree of activation of a single voxel at a specified time. Since TAC introduction, functional connectivity is defined as the degree of co-activation (and therefore overlap) of anatomically secluded areas. Among the different techniques that can be applied for the investigation of functional connectivity, in Resting State-fMRI RS-fMRI) has gained an increasing attention over time (Biswal, Van Kylen, & Hyde, 1997; Lowe, Dzemidzic, Lurito, Mathews, & Phillips, 2000).

Indeed, it has been demonstrated how at rest brain networks present a spontaneous, synchronous activity (Buckner, Andrews-Hanna, & Schacter, 2008; Greicius, Supekar, Menon, & Dougherty, 2009). In order to reflect the rest condition, during the acquisition subjects are asked to keep their eyes closed and relax without falling asleep, as some network activity is modified by the sleep/wake condition (Sämann et al., 2011).

Many processing techniques have been developed over the years for the analysis of fMRI data, and they can be coarsely classified as model-dependent and model-independent methods (van den Heuvel & Hulshoff Pol, 2010).

An example of model-dependent method is the Seed-Based analysis, which entails the identification of an area of interest (or "seed") and the evaluation of TACs that covary with that region. The seed can be chosen a priori, in order to test an hypothesis, or a posteriori, for example selecting the area which is most active during a task execution. Evaluation all TACs covarying with the seed region it is possible to build a connectivity map, which contains all regions functionally connected with our region of interest (ROI). The downside of this method is the impossibility to describe maps of

functional connectivity for regions that do not relate to the seed (Biswal et al., 1997; Cordes et al., 2000).

An example of model-independent method is the independent component analysis (ICA), which allows the investigation of brain networks over the entire brain volume, identifying different networks on the basis of the different TACs and classifying them in distinct clusters. Historically, the ICA has been considered the solution to the "cocktail party problem", as this method is able to identify several networks in an highly confounding setting characterized by the simultaneous activity of distinct cerebral areas pertaining to different functional networks (situation similar to a party where many people are involved in several independent talks, which might be difficult to isolate if examined simultaneously). Nevertheless ICA results have to be interpreted with caution, given the degree of noise of the analysis (M. D. Fox & Raichle, 2007).

Regardless from the specific analysis technique, both model-dependent and model-independent methods allowed the identification of several Resting-State Networks (RSNs), whose activity increases in rest conditions; among these the Default Mode Network (DMN), the Sensory-Motor Network, the Salience Network and the Executive Network (Damoiseaux et al., 2006).

CHAPTER 3

Ultra-high field cerebellar segmentation method development

3.1 Background

The advent of high and ultra-field MRI has significantly improved the investigation of infratentorial structures, such as cerebellum and brainstem, allowing the acquisition of high-resolution images (below 1mm^3 voxel resolution) with better signal-to-noise and contrast-to-noise ratios (Batson, Petridou, Klomp, Frens, & Neggers, 2015; Sclocco, Beissner, Bianciardi, Polimeni, & Napadow, 2018).

However, as previously described in Chapter 2.1.2, only a few methods are available for the analysis of regional or lobular cerebellar structures, with most of these methods that are validated on datasets acquired with a 1mm^3 voxel resolution, Furthermore, there were no available methods that provided segmentation of all infratentorial structures, namely cerebellar lobules, cerebellar WM and brainstem, limiting their application only to the evaluation of possible cerebellar involvement. The objective of our study was to improve the accuracy of cerebellar volume estimation and provide a tool for the simultaneous segmentation of cerebellum and brainstem by implementing a new algorithm named SUIT for Enhanced Resolution (SUITer). We validated the results obtained from SUITer segmentation against manual segmentation, as well as against those obtained using with the widely available, state-of-the-art software for cerebellar segmentation (namely, SUIT, FreeSurfer, CNN), also showing possible SUITer application to different resolution images (0.7 and 1mm^3 of voxel resolution).

3.2 Methods

Outline

SUITer pipeline includes the following steps:

(i) Brain MR images segmentation into tissue types (ie, GM, WM and CSF) using the computational anatomy toolbox (CAT12) (http://www.neuro.uni-jena.de/cat/)

(ii) Cerebellum and brainstem isolation, achieved by using the inverse warping field generated by CAT12 to transpose the standard brain brainstem-cerebellum mask back in the subject space and applying it to both GM and WM tissues segmented with CAT12

(iii) Cerebellar lobules segmentation obtained by customizing the available SUIT algorithm to allow its application to high-resolution datasets

(iv) WM and brainstem segmentations, obtained masking cerebellar lobules from the isolated cerebellum-brainstem resulting from step (ii)

The proposed method was first validated on publicly available images of five HC acquired at 3T MRI against manual segmentation (considered as the gold standard) and standard SUIT processing (validation analysis). Since both the cerebellum and the brainstem show high left-right symmetry, we increased the size of the validation dataset flipping the original five MR images.

After validation, the feasibility of SUITer was tested both in HC and pathological brains. Specifically, SUITer was tested in 10 multiple sclerosis (MS) patients, a condition characterized by the presence of cerebellar and brainstem atrophy (Mormina et al., 2017) and 10 HC MRI data acquired at both 3 and 7T magnetic fields (application analysis).

Participants

For the validation analysis, images of five HCs (3 females, age range = 29-57 years, mean age = 37 years) were obtained from a publicly available dataset (http://imaging-genetics.camh.ca/cerebellum).

For the application analysis, 10 MS patients (7 females, age range=38-61 years, mean age=49 years, disease duration (DD) range=4-37 years, mean=19 years) and 10 HCs (8 females, age range=27-52 years, mean age=39 years), were randomly selected from an internal MRI database. Subjects underwent two separate MRI sessions (3 and 7T) on the same day at the Icahn School of Medicine at Mount Sinai, New York, USA.

MRI Data Acquisition

Datasets used in the validation analysis were acquired on a 3T scanner (GE Discovery MR 750, General Electric) using an 8-channel head coil. Volumetric images were obtained by acquiring a high-resolution 3D T1-weighted inversion-prepared fast spoiled gradient-recalled echo sequence (FSPGR-BRAVO), with the following parameters: voxel size=0.6x0.6x0.6mm^3; field of view (FOV)=220mm; TR/TE/TI=9.2/4.3/650ms; flip angle=8°; 2NEX. ZIPX2 and ZIP512 reconstruction filters were used to upsample data to 0.3mm^3 voxels.

Datasets used in the application analysis were acquired on a 3 and 7T scanners.

Datasets (3T) were acquired on MAGNETOM Skyra (Siemens Healthineers) using a 32-channels head and neck coil. A T1-weighted magnetization prepared rapid gradient echo (MPRAGE) sequence was acquired with the following parameters: voxel size=0.8x0.8x0.8mm^3; FOV=256×256mm²; 224 sagittal slices; TR/TE/TI=3,000/2.47/1,000ms; flip angle=7°; generalized autocalibrating partially parallel acquisition (GRAPPA) with an acceleration factor R=2.

Datasets (7T) were acquired on MAGNETOM (Siemens Healthineers) using a 32-channels head coil, with an MPRAGE sequence with the following parameters: voxel size=0.7x0.7x0.7mm^3; FOV= 224×224mm²; 240 sagittal slices; TR/TE/TI=2,200/2.95/1,050ms; flip angle=7°; GRAPPA with acceleration factor R=2.

SUITer Pipeline

SUITer processing pipeline was implemented in Matlab language (R2015b version) and ran on a Mac OS X 10.9.5 workstation equipped with a 64-bit 3.5 GHz 6-Core Intel Xeon ES processor and 64 GB 1866 MHz DDR3 RAM memory.

Brain Segmentation

Brain 3D T1-weighted images were segmented using CAT12, an extension of the Unified Segmentation approach in SPM12. For the current analysis, the default parameters were used for CAT12 segmentation except for sampling distance, which was set to 2 instead of 3 in order to obtain a better delineation of brain tissues. Briefly, the CAT12 segmentation approach is based on an adaptive maximum a posterior technique that accounts for image intensity inhomogeneities, noise, local variations of intensity, and PVE within each voxel (Manjón, Coupé, Martí-Bonmatí, Collins, & Robles, 2010), thus providing a more accurate segmentation than SPM12. An additional improvement offered by CAT12 over SPM12 approach is the integration of the diffeomorphic anatomical registration using exponentiated lie algebra (DARTEL) normalization to an existing T1-weighted template in MNI space (Ashburner, 2007), generated using 555 HC subjects of the IXI-database (IXI555) with 1.5mm isotropic resolution instead of the 2 mm MNI152 template available in SPM12 (http://www.brain-development.org).

Isolation

In order to create a standard mask, the cerebellum and the brainstem were manually isolated on the T1-weighted IXI555 template, part of CAT12 toolbox. Manual segmentation was made by a trained rater and reviewed by an experienced rater, based on the Harvard-Oxford subcortical structural and the SUIT cerebellum atlases (Diedrichsen, 2006). During CAT12 segmentation, single subject structural data were aligned to the IXI555 template using the DARTEL normalization (Ashburner, 2007). Two warping fields were produced by CAT12; the direct warping field that aligns the single subject structural data to the IXI555 template and the inverse warping field (aligns the IXI555 template to subject structural data). The resulting inverse warping field was then used to

transpose the infratentorial mask back to the native space. Of note, the IXI555 infratentorial mask contains two labels, the cerebellum (label 1) and brainstem (label 2). The transposed mask was binarized then applied to both GM and WM CAT12 brain segmentations to isolate infratentorial segmentations in the subject space.

Cerebellum and Brainstem Segmentation

Both the cerebellum-brainstem mask and the isolated GM and WM obtained from the above mentioned steps were aligned to the SUIT atlas template via an affine transformation, followed by DARTEL registration (Ashburner, 2007). The linear and nonlinear transformations derived from the previous coregistration step were inverted. By applying the inverted transformations, the SUIT atlas was then realigned in the native subject space. Lobules segmentation was further corrected by masking for the WM and CSF obtained from the CAT12 segmentation (threshold of 0.8). Brainstem segmentation resulting from the isolation step (label 2) was corrected from residual CSF. WM segmentation was obtained by masking cerebellar lobules and brainstem from the transposed binarized infratentorial mask in the subject space (see Figure 18 for a flowchart of the method).

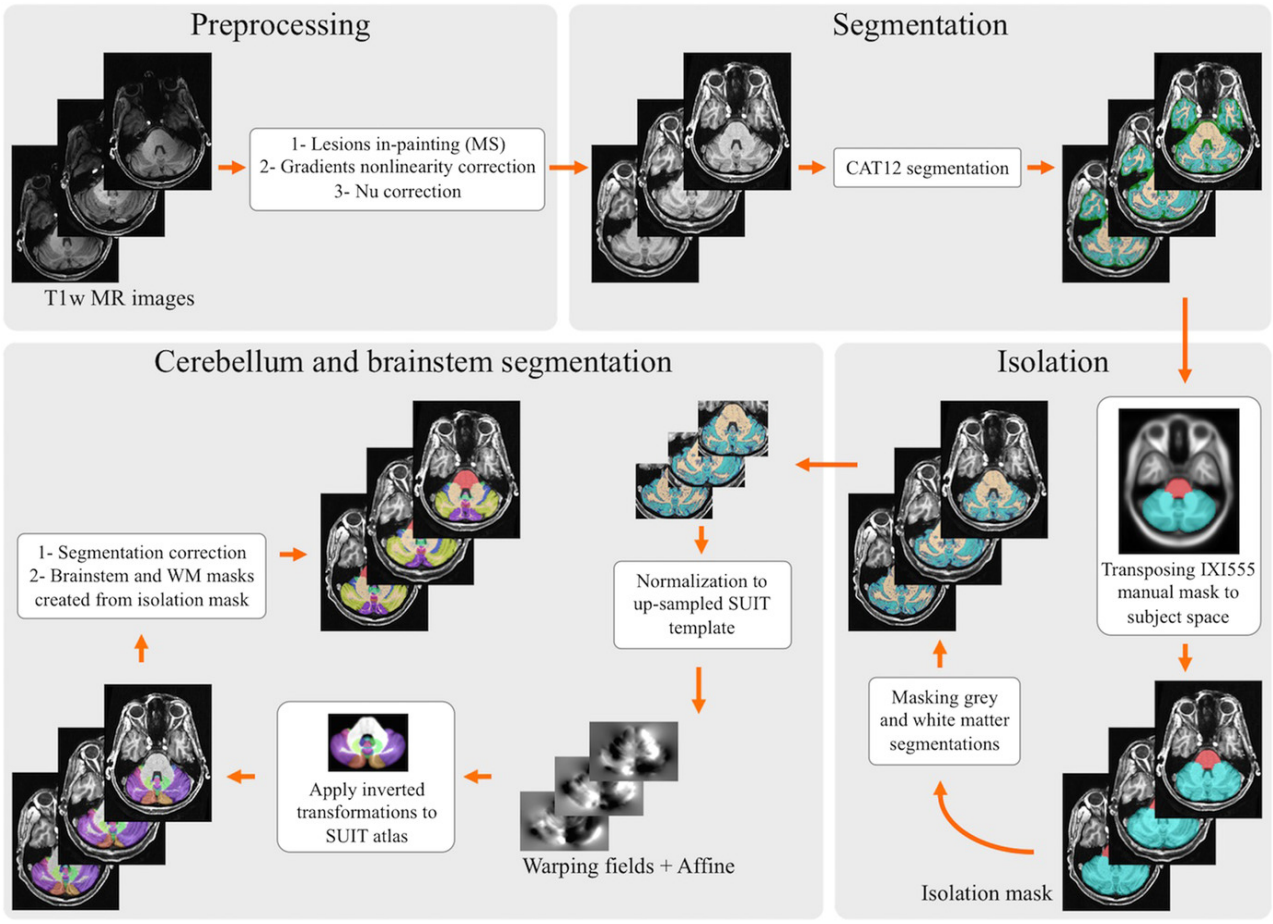

Figure 18: Overview of preprocessing and SUITer pipeline steps. Nu = nonuniformity intensity.

The SUIT template and atlas were resampled to avoid image blurring to the same resolution as the input data using a spline interpolation and nearest neighbors, respectively. Considering that the standard SUIT processing pipeline is optimized to process data with a 1mm isotropic resolution, SUIT scripts were modified accordingly to take into account for the upsampled resolution of both the SUIT template atlas and the input data.

SUIT Customization

Methodological differences between SUIT and SUITer are highlighted below:

(i) Brain segmentation: CAT12 toolbox25 was used to segment brain tissues instead of the unified segmentation approach in SPM12, part of standard SUIT pipeline (Diedrichsen, 2006). The CAT12 segmentation approach is based on an adaptive maximum posterior technique that accounts for

image intensity inhomogeneities, noise, local variations of intensity, and PVE within each voxel, thus, providing a more accurate segmentation than SPM12

(ii) Isolation: Infratentorial tissues isolation was computed using CAT12. During CAT12 segmentation, single subject structural data were aligned to the IXI555 template, part of CAT12 toolbox, using the DARTEL algorithm (Ashburner, 2007). Two warping fields were produced by CAT12: the direct warping filed that aligns the single subject structural data to the IXI555 template and the inverse warping field (aligns the IXI555 template to subject structural data) and the inverse warping field was used to transpose the IXI555 infratentorial manual mask back in the native space. The transposed mask, that is, cerebellum-brainstem mask, was finally applied to both GM and WM tissues segmented with CAT12 to isolate infratentorial GM and WM segmentations in the subject space.

In the SUIT standard pipeline, the unified segmentation approach in SPM12 and the spatial proximity of GM voxels to either cerebral or cerebellar WM are used to isolate infratentorial WM and GM segmentations (Diedrichsen, 2006). This approach could lead to tissue overestimation at standard resolution, or miss segmentation when high-resolution MRI data are processed (Park et al., 2014)

(iii) DARTEL normalization: Data were normalized to SUIT space while preserving its native resolution. To that aim, SUIT atlas and templates (1mm isotropic) were resampled to match the native data resolution and SUIT-DARTEL script was modified to enable high-resolution normalization to SUIT atlas

(iv) Lobules segmentation: SUIT lobules segmentation was corrected from residual CSF, which increases lobules segmentation accuracy

(v) WM and brainstem segmentation: Cerebellar WM and brainstem segmentations are provided, which are not produced by the standard SUIT pipeline

As a result of these customized steps, SUITer segmentation accuracy depends on CAT12 segmentation accuracy, DARTEL normalization to the IXI555 template accuracy and DARTEL normalization to SUIT template accuracy, and the correction step at the end of pipeline that excludes residual CSF from cerebellar lobules parcellation.

Validation and Application Analyses

The standard SUIT was applied to 1mm isotropic resolution images to calculate cerebellar lobule volumes, FreeSurfer was run on both 1 and 0.7mm isotropic resolution images to calculate cerebellar GM, WM, and brainstem volumes, CNN was run on 1 and 0.7mm isotropic resolution images to calculate cerebellar lobule and WM volumes, while SUITer was applied on both validation (1 and 0.7mm isotropic resolution images) and application datasets (3 and 7T MR images) to calculate cerebellar lobule, WM, and brainstem volumes.

Validation Analysis

Manual segmentations used in the validation analysis were derived from publicly available datasets (cerebellum) or in-house segmentation (brainstem). As reported in (Park et al., 2014), cerebellar lobules (from I to X) have been manually segmented by two expert operators, based on the Schmahmann definition (Schmahmann et al., 1999), providing corresponding cerebellar atlases. MR images and cerebellar atlases were resampled to 0.7mm isotropic resolution to match with data resolution obtained by the last generation of MRI scanners.

The brainstem was manually delineated by a trained operator, and reviewed by an expert one, on the T1-weighted images resampled to an isotropic resolution of 0.7mm using spline interpolation. Manual segmentation of the brainstem was based on the Harvard-Oxford subcortical structural atlas and the 7.0T MRI brain atlas (Cho, 2010; Iglesias et al., 2015).

Both atlases (cerebellar and brainstem) were then resampled to an isotropic resolution of 1 mm using the nearest neighbors interpolation.

Application Analysis

WM lesions in MS patients, for both 3 and 7T datasets, were segmented by one experienced observer using a semiautomatic segmentation technique (Jim 7, Xinapse Systems, Northants, UK). To avoid tissue misclassifications during the segmentation, WM lesions were filled with a distribution of signal intensity values equivalent to those in normal-appearing WM in the image (lesions inpainting) (Battaglini, Jenkinson, & De Stefano, 2012). Then, data from both 3 and 7T scans were corrected for gradient nonlinearity induced geometric distortion using the "gradient unwarp" package provided by the Human Connectome Project with the default parameters (Glasser et al., 2013; Jovicich et al., 2006), except for the minimum (maximum) extent of the grid, where spherical harmonics are evaluated = −0.2 m (0.2 m). After this step, 3T MRI data were corrected for intensity inhomogeneity using the nonparametric nonuniform intensity normalization N3 (Sled et al., 1998), while 7T data were corrected using the "Segment" module in SPM12 (Ashburner & Friston, 2005) using an optimized set of input parameters (bias regularization = 0.001; FWHM of Gaussian smoothness of bias = 30mm cutoff; sampling distance = 2; default values for the remaining parameters) (Ashburner & Friston, 2005; Ganzetti, Wenderoth, & Mantini, 2016; Uwano et al., 2014).

Statistical Analysis

For the validation analysis, methods' accuracy was evaluated using five different approaches:

1) The difference in volumes estimation among the manual segmentation at the native resolution, SUIT, FreeSurfer, CNN, and SUITer.

2) The Dice similarity coefficient (DSC), which evaluates the performance of method segmentation by measuring their spatial overlaps.37 The DSC is defined as follows:

$$2 \times |GT \cap S| \, (|GT| + |S|)$$

where |GT| and |S| are the infratentorial structure volume in mm^3 obtained by the manual segmentation and the segmentation method to be evaluated (SUIT, FreeSurfer, CNN, and SUITer), respectively. |GT ∩ S| is the volume in mm^3 common to both segmentation results. A DSC value higher than 80% indicates a very good agreement (Dice, 1945).

3) Linear regression (intercept I, slope S, root mean square error (RMSE), and goodness-of-fit R-squared R^2) of infratentorial volumes obtained by manual segmentation, SUIT, FreeSurfer, CNN, and SUITer.

4) The intraclass correlation coefficient (ICC) among the infratentorial volumes obtained by manual segmentation, SUIT, FreeSurfer, CNN, and SUITer.

5) Cohen's d coefficient among the infratentorial volumes obtained by manual segmentation, SUIT, FreeSurfer, CNN, and SUITer.

Lobules I-II, III, and IV in manual segmentations were combined to match those from SUIT and SUITer. Due to some labeling differences between MaGeT, SUIT and SUITer, lobules laterality, as well as Crus I and Lobule IX volumes were not taken into account in the validation analysis. Of note, we did not evaluate the accuracy of SUITer, FreeSurfer cerebellar WM segmentation because the arbor vitae was not included in the manual segmentation of WM mask (Park et al., 2014).

For the application analysis, cerebellar lobules, WM and brainstem were segmented using SUITer for both 3 and 7T datasets. The agreement in terms of infratentorial volumes/segmentations between the two scanners was evaluated using the difference in volumes estimation, the DSC, linear regression, ICC, and Cohen's d coefficient. To quantify the DSC between 3 and 7T segmentations, 7T MR images were linearly aligned to 3T MR images using a 12 degrees of freedom affine FLIRT registration and the resulting transformation matrix was applied to 7T segmentations (Jenkinson, Beckmann, Behrens, Woolrich, & Smith, 2012). Figure 19 shows the results of alignment between 3 and 7T images from an MS patient and a HC. Statistical analyses were conducted with Matlab software (R2015b version). Values are expressed as mean ± SD, unless otherwise indicated.

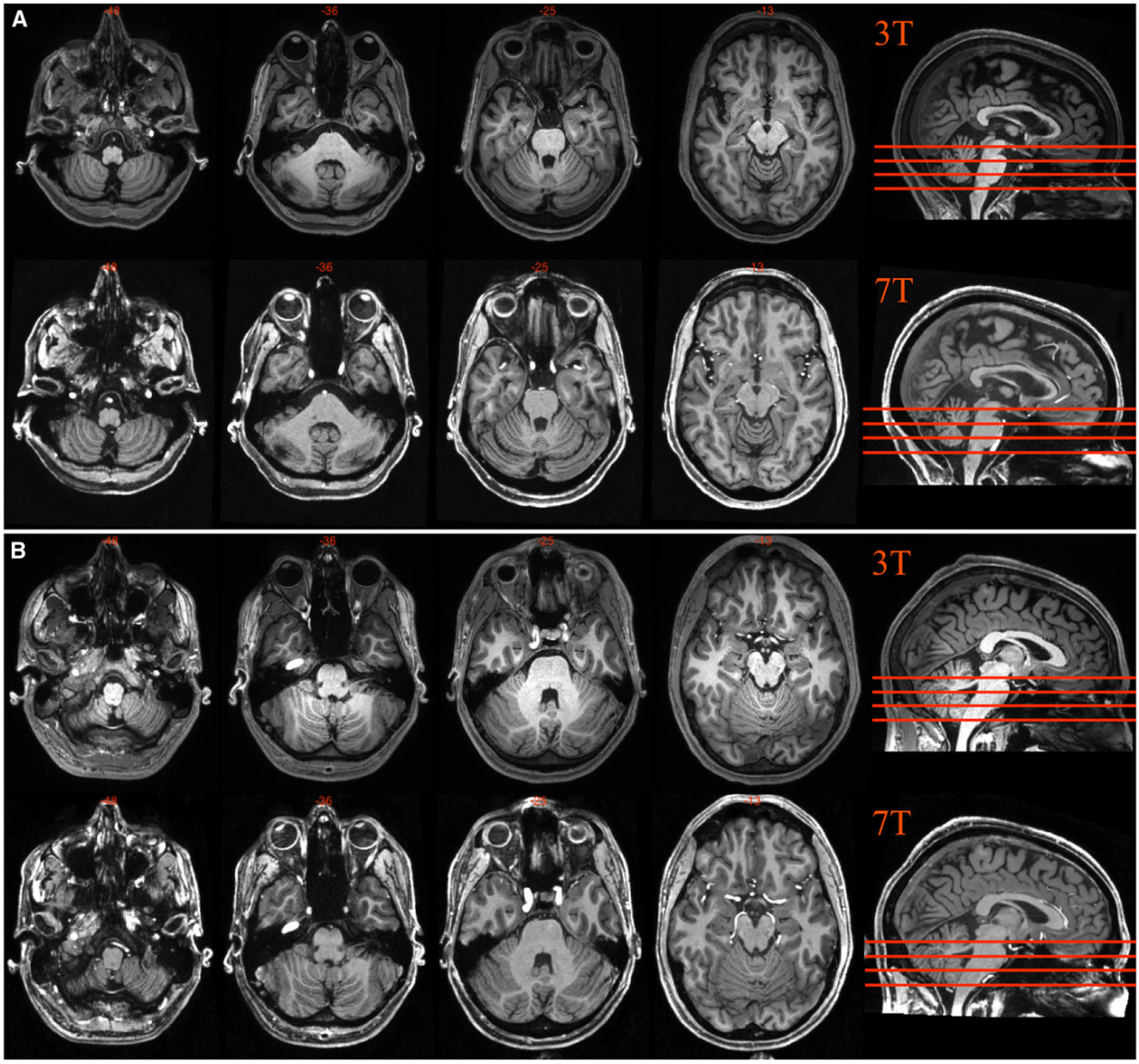

Figure 19: Example of alignment between 3 and 7T data. Results of linear registration between 3 and 7T images from an MS patient (panel A) and a HC (panel B).

3.3 Results

Computational Time

The computational time of the standard SUIT to process a T1-weighted volume at 1mm isotropic resolution was 6.10 minutes. The computational times of the SUITer pipeline on 1 and 0.7mm isotropic resolution T1-weighted volume were 16.8 and 29.9 minutes, respectively. The computational time of the CNN pipeline on 1 and 0.7mm isotropic resolution T1-weighted volumes were 7.6 and 10.9 minutes, respectively. Finally, the computational time of the FreeSurfer pipeline on 1 and 0.7mm isotropic resolution T1-weighted volume were 10 hours 38.5 minutes and 17 hours 2.8 minutes, respectively.

Validation Analysis

Infratentorial volumes obtained from manual segmentation, SUIT, FreeSurfer, CNN, and SUITer methods are summarized in Table 1, while accuracy measurements are summarized in Tables 2 and 3.

	Validation dataset								Application dataset	
	Manual	**SUIT**	**CNN 0.7 mm**	**CNN 1 mm**	**Freesurfer 0.7 mm**	**Freesurfer 1 mm**	**SUITer 0.7 mm**	**SUITer 1mm**	**SUITer 3T**	**SUITer 7T**
Lobule I-IV	5.94 (0.80)	7.36 (0.83)	7.99 (0.71)	8.46 (1.16)	-	-	5.86 (0.44)	6.10 (0.48)	6.28 (0.93)	5.95 (0.99)
Lobule V	7.59 (1.39)	8.92 (0.89)	6.95 (0.73)	6.92 (1.31)	-	-	7.75 (0.46)	7.97 (0.52)	8.62 (1.27)	7.96(1.09)
Lobule VI	15.45 (2.49)	20.51 (2.64)	19.71 (2.02)	19.46 (2.34)	-	-	18.01 (2.10)	19.15 (2.34)	19.65 (2.95)	18.00 (2.85)
Crus I*	22.96 (4.80)	28.17 (3.17)	24.27 (3.52)	24.52 (3.40)	-	-	25.09 (3.68)	27.05 (3.75)	26.40 (4.34)	24.75 (4.17)
Crus II	15.59 (3.48)	20.38 (2.40)	16.61 (2.38)	16.79 (2.20)	-	-	17.23 (2.27)	18.12 (2.30)	17.70 (2.58)	16.10 (2.33)
Lobule VIIb	8.72 (1.46)	10.95 (1.38)	11.66 (1.74)	11.53 (2.17)	-	-	9.16 (1.36)	9.86 (1.43)	9.26 (1.43)	8.83 (1.43)
Lobule VIIIa	10.30 (3.85)	11.99 (1.61)	9.62 (1.03)	9.66 (1.34)	-	-	9.32 (1.34)	10.16 (1.53)	9.26 (1.17)	8.93 (1.34)
Lobule VIIIb	7.00 (1.00)	9.54 (1.09)	6.27 (0.92)	6.40 (0.94)	-	-	7.27 (0.84)	8.06 (0.89)	7.35(0.95)	7.17 (1.02)
Lobule IX*	6.73 (1.12)	7.59 (1.05)	6.83 (1.14)	6.88 (1.18)	-	-	6.05 (0.99)	6.30 (1.00)	6.64 (1.02)	6.37 (1.01)
Lobule X	1.35 (0.18)	1.80 (0.20)	1.12 (0.08)	1.15 (0.10)	-	-	1.39 (0.21)	1.44 (0.25)	1.54 (0.24)	1.34 (0.20)
Cerebellar GM	101.58 (13.58)	130.81 (15.27)	111.01 (11.26)	111.76 (12.16)	105.05 (14.12)	105.04 (14.78)	107.14 (12.77)	114.20 (13.44)	112.68 (15.13)	105.39 (14.94)
Cerebellar WM	15.47 (1.34)	-	11.01 (1.53)	11.17 (1.52)	24.00 (2.97)	24.44 (2.10)	27.12 (3.76)	24.60 (3.07)	29.66 (4.04)	28.28 (3.70)
Brainstem	30.86 (4.00)	-	-	-	24.89 (2.96)	24.82 (3.09)	29.16 (3.18)	29.21 (3.19)	30.47 (2.78)	28.86 (2.64)

Table 1: Infatentorial volumes calculated with manual segmentation, SUIT, CNN, Freesurfer and SUITer
Volumes are expressed as mean (SD) in milliliter. *Difference in definition between manual, SUITer and SUIT methods for the **Validation dataset**. CNN, convolutional neural network; GM, gray matter; SUIT, Spatially Unbiased Infratentorial;SUITer, Spatially Unbiased Infratentorial for enhanced resolution; WM, white matter.

Comparison	Cerebellar GM					Cerebellar WM					Brainstem				
	VD (ml)	DSC (%)	Linear regression (S,I,RSME,R^2)	ICC	Cohen's d	VD	DSC	Linear regression (S,I,RMSE,R^2)	ICC	Cohen's d	VD	DSC	Linear regression (S,I,RMSE,R^2)	ICC	Cohen's d
SUIT *vs* Manual	29.23 (4.64)	83.26 (1.35)	0.81,-3.73,3.71,0.92	0.30	2,07	-	-	-	-	-	-	-	-	-	-
CNN 0.7 mm *vs* Manual	9.43 (3.19)	89.69 (1.29)	1.11,-21.18,3.14,0.95	0.74	0.78	-4.46 (1.01)	76.42 (4.32)	0.47,10.33,1.10,0.32	0.09	3.18	-	-	-	-	-
CNN 1 mm *vs* Manual	10.17 (4.14)	89.58 (1.71)	1.00,-9.69,4.39,0.89	0.71	0.82	-4.30 (1.35)	77.31 (4.70)	0.45,10.41,1.13,0.29	0.09	3.08	-	-	-	-	-
Freesurfer 0.7 mm *vs* Manual	3.56 (1.76)	86.19 (0.49)	0.90,6.73,1.15,0.99	0.96	0.26	-	-	-	-	-	5.95 (0.91)	86.72 (0.74)	1.26,-0.54,0.53,0.98	0.38	1.76
Freesurfer 1 mm *vs* Manual	3.47 (3.08)	86.73 (0.64)	0.85,11.97,2.32,0.97	0.95	0.25	-	-	-	-	-	6.02 (0.86)	86.69 (1.31)	1.20,0.95,0.62,0.98	0.38	1.75
SUITer 0.7 mm *vs* Manual	5.56 (3.80)	83.46 (1.71)	0.96,-1.05,3.99,0.914	0.88	0.43	-	-	-	-	-	1.70 (0.75)	93.25 (0.48)	1.18,-3.43,0.52,0.98	0.88	0.49
SUITer 1 mm *vs* Manual	12.62 (3.85)	83.77 (1.72)	0.91,-2.59,3.89,0.92	0.66	0.96	-	-	-	-	-	1.65 (0.72)	93.26 (0.47)	1.17,-3.34,0.51,0.98	0.88	0.47
SUITer 0.7 mm *vs* 1 mm	7.07 (0.88)	91.54 (0.49)	1.05,1.54,0.61,1.00	0.87	0.54	2.52 (0.89)	85.82 (1.44)	0.81,2.76,0.53,0.97	0.76	0.73	0.05 (0.06)	96.55 (0.42)	1.00,-0.09,0.06,1.00	1.00	0.01
SUITer 3T *vs* 7T	7.29 (1.68)	87.44 (1.27)	1.01,6.62,1.70,0.99	0.89	0.48	1.38 (1.77)	74.81 (2.26)	0.98,1.89,1.66,0.81	0.85	0.36	1.61 (0.40)	94.20 (0.76)	1.04,0.33,0.37,0.98	0.84	0.59

Table 2: Comparisons and correlations analyses between manual segmentation, SUIT, CNN, Freesurfer and SUITer.

Values are expressed as mean (SD), unless otherwise indicated. CNN, convolutional neural network; DSC, Dice similarity coefficient; GM, grey matter; I, intercept; ICC, intraclass correlation coefficient; R2, r-squared; RMSE, root mean square error; SUIT, Spatially Unbiased Infratentorial; SUITer, Spatially Unbiased Infratentorial for enhanced resolution; VD, volume difference; WM, white matter.

	Validation dataset (DCS)				
SUIT	**CNN 0.7 mm**	**CNN 1 mm**	**SUITer 0.7 mm**	**SUITer 1mm**	
Lobule I-IV	75.25 (2.87)	80.10 (6.69)	78.71 (8.61)	78.57 (2.96)	79.85 (2.46)
Lobule V	68.91 (4.44)	72.97 (3.29)	72.31 (6.49)	72.32 (3.01)	71.77 (3.11)
Lobule VI	77.78 (3.15)	82.74 (2.85)	83.28 (2.84)	80.13 (2.81)	79.12 (3.07)
Crus I*	76.52 (5.18)	85.99 (3.47)	84.76 (5.26)	77.94 (3.26)	76.20 (3.61)
Crus II	69.64 (6.42)	77.89 (5.04)	77.30 (5.20)	68.28 (4.75)	69.33 (4.64)
Lobule VIIb	55.11 (7.91)	65.33 (11.70)	64.66 (11.22)	50.82 (9.51)	53.32 (9.01)
Lobule VIIIa	62.95 (4.30)	70.84 (8.60)	70.59 (7.69)	59.16 (6.11)	60.95 (5.60)
Lobule VIIIb	67.45 (2.32)	80.16 (4.23)	79.81 (3.22)	62.53 (3.76)	66.73 (3.90)
Lobule IX*	77.07 (2.65)	89.63 (0.56)	89.39 (1.36)	77.02 (1.37)	79.25 (1.19)
Lobule X	63.27 (3.54)	76.11 (3.47)	76.36 (3.54)	71.76 (1.73)	72.68 (3.01)

Table 3: Dice similarity coefficient between manual segmentation, SUIT, CNN and SUITer.

Figure 20 shows an example of segmentation of infratentorial structures obtained by manual, SUIT, FreeSurfer, CNN, and SUITer methods.

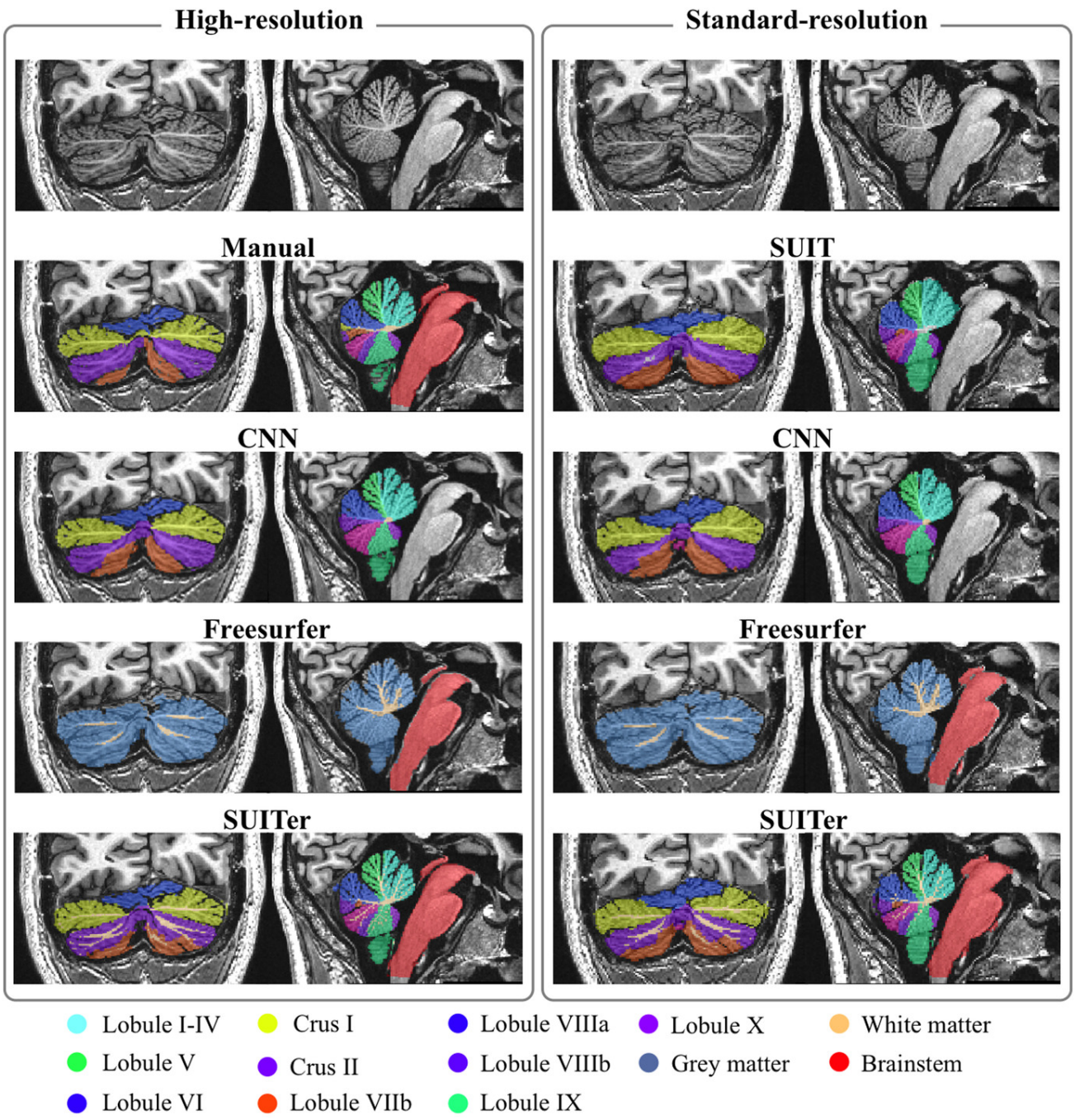

Figure 20: Example of cerebellar lobules, WM, and brainstem structures segmentation on the validation dataset obtained by manual segmentation, CNN, FreeSurfer, and SUITer at high and standard resolutions (0.7 and 1mm isotropic resolutions), SUIT at standard resolution.

Of note, SUIT method does not provide cerebellar WM and brainstem segmentations; therefore, for this method only cerebellar lobule segmentations were taken into account. FreeSurfer method does not provide cerebellar lobule segmentations; therefore, for this method only cerebellar GM, WM, and brainstem volumes were taken into account. CNN method does not provide brainstem

segmentations; therefore, for this method only cerebellar lobule, cerebellar GM, and WM segmentations were taken into account in our validation analysis. Manual segmentation was considered as the ground truth.

Cerebellar GM

SUIT overestimated cerebellar GM volume by 29.23 ± 4.64mL. CNN, FreeSurfer and SUITer methods overestimated cerebellar GM volume by 9.43 ± 3.19, 3.56 ± 1.76, and 5.56 ± 3.80mL, respectively, for 0.7mm isotropic resolution data and by 10.17 ± 4.14, 3.47 ± 3.08, and 12.62 ± 3.85mL, respectively, for 1mm isotropic data.

The overlap between SUIT and manual segmentations was DSC = 83.26 ± 1.35%. CNN, FreeSurfer, and SUITer segmentations were highly overlapping with manual segmentation for 0.7 mm isotropic resolution data (DSC = 89.69 ± 1.29, 86.19 ± .49, and 83.46 ± 1.71%, respectively) as well as for 1 mm isotropic data (DSC = 89.58 ± 1.71, 86.73 ± .64, and 83.77 ± 1.72%, respectively). Results of the overlap between SUIT, CNN, FreeSurfer, SUITer, and manual segmentations for the individual cerebellar lobules are summarized in Table 3 (on page 60).

ICC between CNN, FreeSurfer, and SUITer estimated cerebellar GM volumes and manual volumes for 0.7 mm isotropic resolution data were 0.74, 0.97, and 0.88, respectively. While for 1mm isotropic resolution data, ICC were 0.3, 0.71, 0.95, and 0.66 for SUIT, CNN, FreeSurfer, and SUITer, respectively.

Cohen's d between CNN, FreeSurfer, and SUITer estimated cerebellar GM volumes and manual volumes for 0.7mm isotropic resolution data were 0.78, 0.26, and 0.43, respectively. While for 1mm isotropic resolution data, Cohen's d were 2.07, 0.82, 0.25, and 0.96 for SUIT, CNN, FreeSurfer, and SUITer, respectively.

Linear regression analysis showed a strong correlation between cerebellar GM volumes measured by manual segmentation and those obtained by SUIT (R^2 = 0.92 for 1mm dataset), CNN (R^2 = 0.95 and 0.89 for 0.7 and 1 mm datasets, respectively), FreeSurfer (R^2 = 0.99 and 0.97 for 0.7 and 1mm datasets, respectively) and SUITer (R^2 = 0.91 and 0.92 for 0.7 and 1mm datasets, respectively),

with SUITer showing an almost perfect agreement across resolutions (R^2 = 1.00). Results of the linear regression analysis for cerebellar lobules are shown in Figure 21.

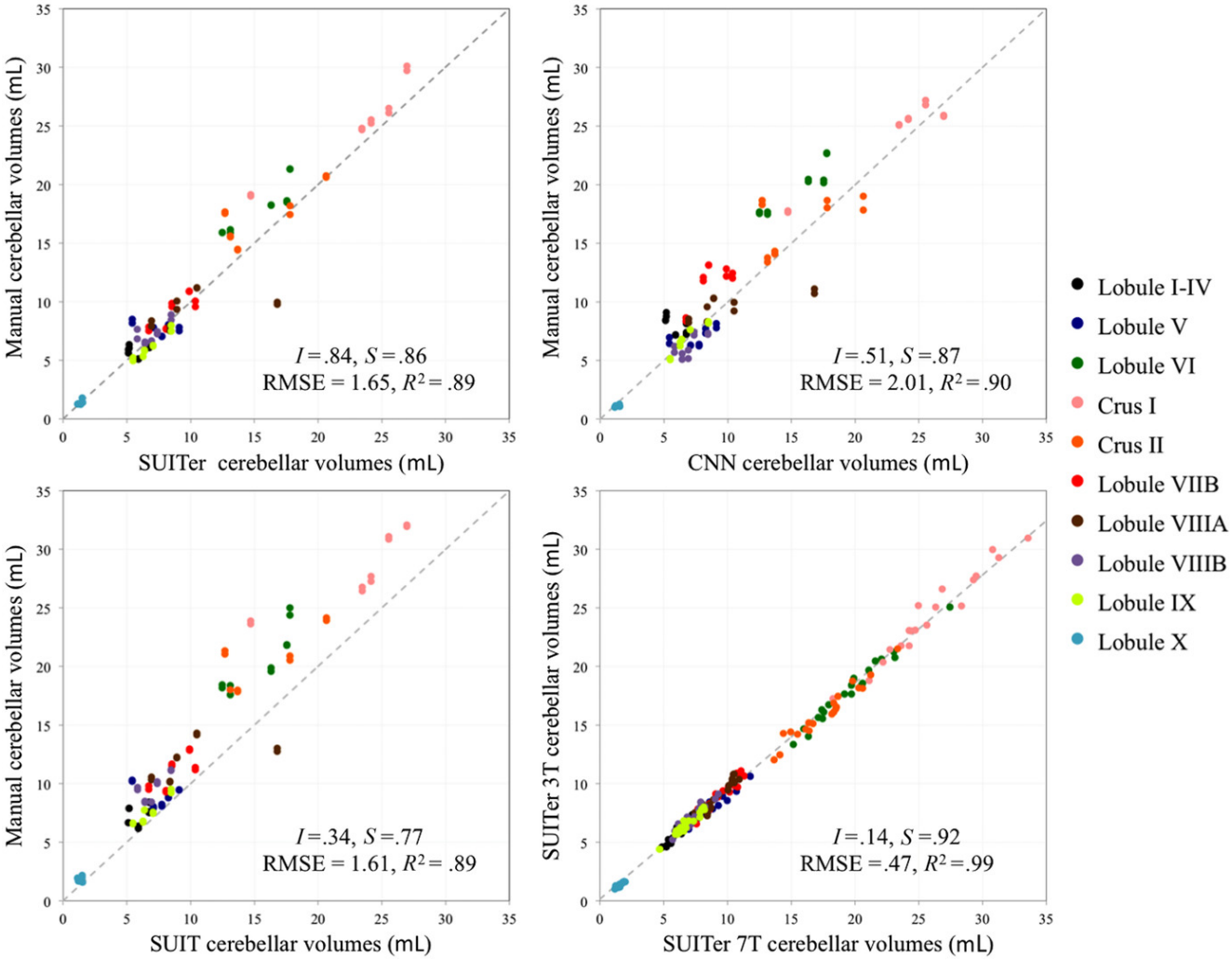

Figure 21: Scatterplots of the linear regression between cerebellar lobules volumes obtained from manual segmentation, SUIT, CNN, and SUITer on the validation dataset and SUITer on the application dataset. Due to some labeling differences between MaGeT, SUIT, and SUITer, lobules laterality, as well as Crus I and Lobule IX volumes were not taken into account for the linear regression. The difference in cerebellar WM definition between SUIT/SUITer and MaGeT segmentations explains the observed discrepancy in subject V5 for lobule VIIIa volume. I = intercept; S = slope; R^2 = goodness-of-fit R-squared; RMSE = root mean square error.

Cerebellar WM

We did not compared directly SUITer WM segmentation with that obtained with manual segmentation because the MaGeT atlas used for the validation does not include the arbor vitae, which instead is included in SUITer and Freesurfer cerebellar WM segmentations.

CNN underestimated cerebellar WM volume by −4.46 ± 1.01 and −4.30 ± 1.35mL for 0.7 and 1mm isotropic resolution datasets. The difference between cerebellar WM volume estimated by SUITer for 0.7 and 1mm data was 2.52 ± 0.89mL.

The DSC showed a moderate agreement between manual segmentation and CNN segmentation for 0.7 mm isotropic resolution data (DSC = 76.42 ± 4.32%) as well as for 1mm isotropic data (DSC = 77.31 ± 4.70%). In addition, the DSC showed a high agreement between SUITer on 0.7 and 1mm datasets (DSC = 85.82 ± 1.44%).

Linear regression analysis showed weak correlations between cerebellar WM volumes measured by manual and CNN (R^2 = 0.32 and 0.29 for 0.7 and 1mm datasets, respectively), with SUITer showing a very high agreement across resolutions (R^2 = 0.97).

ICC between CNN and manual cerebellar WM volumes was 0.09 for both 0.7 and 1 mm isotropic resolution data. ICC was 0.76 for SUITer on 0.7 and 1mm datasets.

Cohen's d between CNN and manual WM volumes for 0.7 and 1mm isotropic resolution datasets were 3.18 and 3.08, respectively. Cohen's d was 0.73 for SUITer on 0.7 and 1mm datasets.

Brainstem

Compared to the manual segmentation, FreeSurfer underestimated brainstem volume by 5.95 ± .91 mL for 0.7 mm and 6.02 ± 0.86 mL for 1 mm data. SUITer slightly underestimated brainstem volume by 1.70 ± 0.75mL for 0.7mm and 1.65 ± 0.72mL for 1mm data. The DSC showed a high agreement between FreeSurfer, SUITer, and manual segmentations across resolutions, with a mean value of 86.72 ± 0.74 for FreeSurfer and 93.25 ± 0.48% for SUITer at 0.7 mm and 86.69 ± 1.31 for FreeSurfer and 93.26 ± 0.47% for SUITer using 1 mm datasets. In addition, the DSC showed a very high agreement between SUITer on 0.7 and 1 mm datasets (DSC = 96.55 ± 0.42%).

Finally, the linear regression analysis also showed an almost perfect correlation between brainstem volumes obtained by FreeSurfer, SUITer, and manual segmentation at both 0.7 and 1mm (R^2 = 0.98) as well as between SUITer on 0.7 and 1mm datasets (R^2 = 1.00).

Application Analysis

Cerebellar GM, WM, and brainstem volumes obtained by SUITer method from 3 and 7T MR images are summarized in Table 1, while accuracy measurements are summarized in Tables 2 and 3.

Figure 22 shows an example of segmentation of cerebellar lobules, WM, and brainstem structures obtained by SUITer on 3 and 7T MRI datasets.

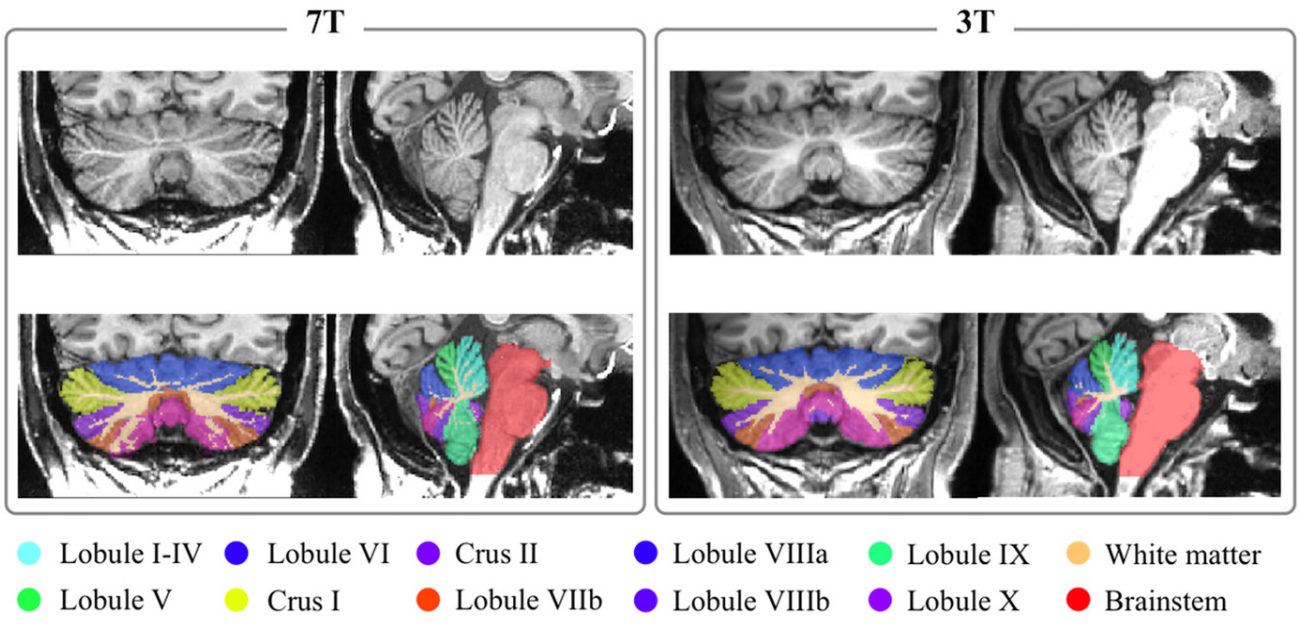

Figure 22: Example of segmentation of cerebellar lobules, WM, and brainstem structures obtained by SUITer on the 3 and 7T MRI data of an MS patient (application dataset).

Cerebellar GM

The difference between cerebellar GM volume estimated by SUITer from 3 and 7T images was 7.29 ± 1.68mL (with 112.68 ± 15.13mL calculated at 3T and 105.39 ± 14.94mL at 7T), with data showing a high overlap, a strong correlation and a medium effect size (DSC = 87.44 ± 1.27%, R^2 =

0.99, ICC = 0.89, and Cohen's d = 0.48). Results of the linear regression analysis for cerebellar lobules are shown in Figure 21.

Cerebellar WM

SUITer estimated a mean cerebellar WM volume of 29.66 ± 4.04mL on datasets acquired at 3T, while the mean value obtained from 7T images was of 28.28 ± 3.70mL, providing a difference of 1.38 ± 1.77mL. The DSC, R^2, ICC and Cohen's d between SUITer segmentations of images acquired at 3 and 7T were 74.81 ± 2.26%, 0.81, 0.85, and 0.36, respectively.

Brainstem

The difference between brainstem volumes estimated by SUITer at 3 and 7T was 1.61± 0.40mL, with a mean volume of 30.47 ± 2.78mL obtained from images at 3T and 28.86 ± 2.64mL provided by the analysis of 7T data. Similarly to what proved for cerebellar GM and WM volumes, also brainstem volumes showed a strong correlation and medium effect size between 3 and 7T data (R^2 = 0.99, ICC = 0.84, and Cohen's d = 0.59). The DSC demonstrated a very high overlap between 7 and 3T segmentations (94.20 ± 0.76%).

Between-group comparisons

SUITer showed similar cerebellar GM volume differences between MS patients and HC at both 3 and 7T (7.69 and 7.76mL, respectively). SUITer showed also similar volume differences between MS patients and HC at 3 and 7T for cerebellar WM (2.72 and 2.04mL, respectively) and brainstem (1.69 and 1.82mL, respectively).

3.4 Discussion

SUITer offers a cerebellar GM segmentation that is close to the best fitting provided by FreeSurfer, with the advantage of computing also cerebellar lobules. For lobular segmentation, SUITer showed a better to similar accuracy than SUIT, but a lower accuracy than CNN. CNN performs poorly for cerebellar WM segmentation. For the brainstem segmentation, SUITer outperforms FreeSurfer. SUITer has the advantage, when compared with SUIT, CNN, and FreeSurfer, to provide good GM segmentation, with lobules parcellation comparable to CNN, together with WM segmentation and excellent brainstem segmentation.

When SUITer performance was compared to that reported in literature for other methods, it provided overall similar results in terms of accuracy. In particular, SUITer showed slightly better results than those reported for RASCAL, with a median DSC of 83% compared to the 82% achieved by the latter (Weier, Fonov, et al., 2014).

SUITer method showed a lower accuracy in cerebellar GM segmentation than that reported by MaGeT (mean SUITer DSC 84% compared to 92%). Similarly, SUITer showed a lower accuracy than that of cerebellum lobules segmentation (CERES) method, which has the highest accuracy among the publicly available methods (SUIT, CNN, FreeSurfer, MaGeT, and RASCAL) (Romero et al., 2017).

Despite their higher accuracy in cerebellar GM segmentation compared to SUITer, different points should be kept in mind when considering MaGeT, CERES, FreeSurfer, and CNN approaches. Indeed, it should be noted that MaGeT and CERES pipelines have been only validated on 1.5T images with a standard resolution (1mm isotropic resolution), while SUITer has been specifically implemented for high-resolution images acquired at ultra-high-field. Furthermore, MaGeT demands higher computational times compared to SUITer. Indeed, MaGeT requires up to 6 hours to process standard resolution data compared to less than 30 minutes employed by SUITer to process a high-resolution data, thus, reducing its feasibility to process large high-resolution datasets.

Similarly, FreeSurfer requires a very high computational time to process both standard and high-resolution data and does not provide cerebellar lobules segmentation. CNN is a very fast pipeline and showed a higher accuracy than SUITer. However, CNN does not provide brainstem segmentation.

There was a very good agreement in WM segmentation performed on images acquired at different spatial resolution ($R^2 = 0.97$) and a good agreement on images acquired at different magnetic field strengths ($R^2 = 0.81$). Unfortunately, we were not able to compare directly SUITer WM segmentation with that obtained with manual segmentation because the MaGeT atlas used for the validation does not include the arbor vitae (Park et al., 2014), which instead is included in SUITer cerebellar WM segmentation. However, the correlation and overlap between SUITer and manual segmentations for the whole cerebellum ($R^2 = 0.93$; DSC = 90.46%) (data not shown) and a visual inspection of SUITer WM segmentation supports the adequacy of WM segmentation. For instance, the WM definition in MaGeT segmentations explains the discrepancy in subject V5 for lobule VIIIa volume estimated by SUIT, FreeSurfer, and SUITer methods (as previously shown in Figure 21, on page 63).

Unlike cerebellar WM volumes, brainstem volumes derived from manual segmentation were available, and there was a strong agreement between SUITer-derived volumes and those obtained with manual segmentation ($R^2 = 0.98$). In addition, the DSC showed a very high agreement between manual segmentation and SUITer (DSC = 93.25%), showing a higher accuracy than the one for the FreeSurfer segmentation as well as the one reported in the literature (Iglesias et al., 2015). However, it is important to bear in mind that SUITer does not provide subsegmentations of pons, midbrain, and medulla oblongata.

As shown in the application analysis, SUITer measurements demonstrated strong correlations between 3 and 7T datasets, supporting its possible use in HC and pathological conditions, on images acquired at different spatial resolution and MR field strengths. Furthermore, when

comparing cerebellar GM volumes between MS patients and HC, SUITer showed on average higher volume differences at both 3 and 7T (7.69 and 7.76mL, respectively) than SUIT (5.37 and 3.75mL, respectively) (data not shown). However, it should be noted that volumes estimated by SUITer in the application analysis were slightly different between 3 and 7T datasets. A potential explanation could be the different preprocessing pipelines, especially intensity nonuniformity correction, used for the high and ultra-high-field datasets (N3 and SPM12 "Segment" module, respectively) (Ganzetti et al., 2016; Sled et al., 1998; Uwano et al., 2014). Additionally, it should be noted that cerebellar lobule volumes were systematically lower at high-resolution compared to those obtained at lower and standard resolutions, in line with the results reported when cortical thickness was evaluated at different magnetic fields as consequence of the reduced PVE (Lüsebrink, Wollrab, & Speck, 2013).

One of the main advantages of the proposed method is that SUITer not only provides lobular parcellation with an overall accuracy comparable to those achievable by many of the available methods at standard and high resolution acquired at 3 and 7T, but it also provides cerebellar WM and brainstem segmentations. None of the above-mentioned cerebellar segmentation methods (SUIT, CNN, MAGeT, Rascal, and CERES) provide any information about all infratentorial compartment, namely cerebellar lobules, WM, and brainstem, limiting their application only to the evaluation of possible cerebellar involvement (Carass et al., 2018). FreeSurfer on the other hand provides WM and brainstem segmentations but does not offer the possibility to quantify lobular volumes. Additionally, SUITer is the first infratentorial segmentation pipeline optimized for high resolution, ultra-high-field data.

The main limitation of our method relates to the brainstem segmentation. The isolated brainstem tissue in 7T data included voxels from the basilar artery, which have high contrast values on 7T MR images. Brainstem segmentations at 7T could be potentially corrected by setting a threshold that

excludes voxels with high contrast values from masked MR images, a possibility that has to be taken into account for future implementation of the method.

In conclusion, we have presented a newly implemented method that provides accurate cerebellar lobules segmentation in HCs and pathological conditions, from standard and high-resolution MR images acquired at both high and ultra-high magnetic fields. SUITer represents a versatile and comprehensive tool for infratentorial structures' analysis, providing simultaneously cerebellar lobules, cerebellar WM, and brainstem segmentations in a reasonable processing time with standard computational resources.

CHAPTER 4

Cerebellar cortex involvement in Friedreich's Ataxia

4.1 Background

Friedreich's ataxia (FRDA), the most frequent genetically determined ataxia, is caused by the decreased expression of frataxin protein due to an abnormal trinucleotide intronic repeat expansion in the FXN gene on chromosome 9 (Campuzano et al., 1996). FRDA originally affects dorsal root ganglia and spinal dorsal columns, with consequent trans-synaptic degeneration of spinocerebellar tracts and cerebellar sub-structures, with only late appearance of a significant cortico-spinal tracts atrophy (Koeppen & Mazurkiewicz, 2013).

Regarding cerebellar GM, both pathological and imaging studies demonstrated that DN are the most affected structures, with a subtle mitochondrial iron accumulation preceding degeneration and atrophy of these deep GM relay stations (Solbach et al., 2014; Ward et al., 2019). Although being long considered as spared by atrophy (Mascalchi, 2013; Ormerod et al., 1994), the cerebellar cortex has been also proved to be affected by neurodegeneration in FRDA, as shown by the presence of GM atrophy, coupled to a reduced cortical thickness of specific cerebellar GM areas in these patients (Della Nave, Ginestroni, Giannelli, et al., 2008; Selvadurai et al., 2016; Vavla et al., 2018). This suggests the presence of a more profound involvement of cerebellar structures extending beyond the exclusive involvement of DN.

All these alterations result in the development, not only of motor manifestations (Pandolfo, 2009), but also of the more inconstant, although significant, neuropsychological symptoms occurring in FRDA (Cocozza et al., 2018). Indeed, beyond motor control and perception, the cerebellum plays a modulating role in cognitive and affective processes (Noroozian, 2014), with an active contribution to a wide variety of composite functions, including evidence-guided decision-making, modulation

of behavior and personality, inner speech neural mechanisms, and cognitive processes underlying action control (Deverett, Koay, Oostland, & Wang, 2018; Koziol et al., 2014; Stoodley & Schmahmann, 2010).

Although a precise localization of different functions clearly does not respect the anatomy of individual cerebellar lobules, recent evidences showed a correlation between neuropsychological deficits and atrophy of specific cerebellar lobules in different neurodegenerative and neuroinflammatory disorders (Y. Chen et al., 2018; Cocozza et al., 2017; Kansal et al., 2017; Olivito et al., 2018; Yang et al., 2019). Nevertheless, information regarding the relation between cerebellar lobular atrophy and cognitive deficits in FRDA is not available. For this reason, we aimed to confirm if cerebellar global and lobular atrophy could occur in FRDA patients, and to investigate the possible correlation between cerebellar volume loss and cognitive performances.

4.2 Methods

Participants

Nineteen patients with genetically confirmed FRDA were included in this study (M/F:13/6; mean age: 28.4±14.1), together with a group of 20 HC of comparable age and sex (M/F:11/9; mean age: 29.4±9.7). FRDA diagnosis was carried out by performing conventional genetic test with short and long triplet repeat primed polymerase chain reaction. Patients were included if their binocular visual acuity was of at least 9/10 with the best correction available.

All patients underwent within one week from the MRI scan a neuropsychological examination, obtaining cognitive tests related to cerebellar functions (i.e. visuo-perception and visuo-spatial functions, visuo-spatial memory and working memory): 10/36 Spatial Recall Test (SPART), Segment Length Discrimination (SLD), Symbol Digit Modality (SDMT), Brief Stroop Test and Trail Making Test (TMT).

In particular, the SPART measures visuospatial memory using three immediate recall trials, and a delayed one. It is particularly suitable for those patients with moderate to severe movement disorders, as it demands a relatively low motor effort. The SLD is a measure of visual perceptual ability, with patients that are required to judge whether two vertical segments, placed one above the other, are equal or different in length. The SDMT assesses information processing speed and visual scanning. Using a reference key placed on the top of the paper, the patient is asked to pair 9 digits with just as many symbols in 90 seconds. The Brief Stroop Test is a three-trial test used to mainly evaluate sustained attention and the ability to inhibit automatic responses while performing a task based on conflicting stimuli. In the first and second trials the patient has to read black inked words indicating colors and name the color of given dots, respectively, while in the third trial (interference condition) the subject has to name the color of the ink of words indicating conflicting colors as quickly as possible. Time and errors are calculated based on the three performances. Finally, the TMT evaluates different cognitive processes as divided attention, visual scanning and set shifting.

In the “A” trial, the subject has to draw lines to connect numbers in sequential order (i.e., 1, 2, 3, etc.), while in the “B” part the subject draws lines connecting numbers and letters in an alternating numeric and alphabetic sequence (i.e., 1-A-2-B, etc.) as rapidly as possible.

Along with the neuropsychological battery, we administered to all patients the Scale for the Assessment and Rating of Ataxia (SARA), the 9 Hole Pegboard Test (9HPT) and PATA rate test (PRT) (Criscuolo et al., 2005; Pane et al., 2018; Schmitz-Hubsch et al., 2008). TMT-A and -B were corrected for dominant hand disability using the 9HPT, while SDMT was corrected for dysarthria using the PATA rate, as previously described (Sacca et al., 2018).

MRI data acquisition and analysis

All subjects included in the study underwent a brain MRI scan with an 8-channel head coil on the same 3T machine (Trio, Siemens Medical Systems, Erlangen, Germany). The acquisition protocol included a T1-weighted MPRAGE sequence, used for the volumetric analysis (160 axial slices; voxel size=1x1x1mm^3; TR=1900ms; TE=3.4ms; TI=900ms; Flip Angle=9°), along with a Fluid Attenuated Inversion Recovery (FLAIR) sequence (25 axial slices; voxel size=1x1x4mm^3; TR=8500ms; TE=106ms; TI=2500ms). Both sequences were preliminarily evaluated by an experienced radiologist before image processing, to exclude the presence of posterior fossa lesions or malformations.

Global and lobular cerebellar volumes were automatically calculated from the T1-weighted volumes using SUIT, as follows: the infratentorial area was isolated and segmented in the principal components to obtain a GM cerebellar mask. This isolated segmented cerebellar GM mask was then normalized to the SUIT cerebellar atlas space. Finally, applying an inverse transformation matrix derived from the previous coregistration step, the atlas was aligned to the native subject space to compute the global cerebellar volume, along with the 10 lobular volumes for each subject as the sum of their hemispheric and vermian portions. The results of each processing steps were visually inspected by an experienced neuroradiologist, to evaluate the quality of the procedure.

Furthermore, to investigate possible cerebellar regional GM differences between the two groups, a VBM analysis was performed. With this aim, the segmented GM cerebellar masks were modulated during the coregistration to the SUIT atlas template, in order to preserve for total cerebellar GM volume, and images were smoothed using a 4-mm FWHM isotropic Gaussian kernel.

Finally, whole brain 3D T1-weighted volumes were segmented using SPM12 to obtain GM, WM and CSF volumes, that were summed to obtain the total intracranial volume (ICV), subsequently used in the analyses to normalize cerebellar volumes for head size.

Statistical analysis

Differences between FRDA and HC for age and sex were tested via an independent t-test and Chi-squared test, respectively, while differences in neuropsychological scores were analyzed via the Mann-Whitney U test, with a statistical threshold for $p<0.05$.

Possible differences between the two groups in terms of cerebellar volumes were investigated using an ANCOVA, age, sex and ICV corrected, with a significance level set for $p<0.005$, Bonferroni corrected for multiple comparisons (0.05/10, as the number of tested cerebellar lobules), while differences in terms of regional GM cerebellar areas, investigated via VBM analysis, were tested using the General Linear Model (GLM, implemented in SPM12) including age, sex and ICV as covariates, with a significance level set for $p<0.05$,corrected for the Family-Wise Error at cluster level. For the VBM analysis, both contrasts (FRDA < HC and FRDA > HC) were probed.

Finally, to study the relationship between impaired clinical variables and cerebellar volume loss, lobular volumes that resulted different between FRDA and HC were entered in an age and sex corrected partial correlation analysis. Similarly, when regional GM differences emerged between the two groups, the corresponding first eigenvariate was extracted from the cluster and adjusted for age, sex and ICV. The so obtained residuals were standardized and their relationship with clinical data was assessed via correlation analysis. For both analyses, the statistical threshold was set for $p<0.05$.

All statistical analyses, with the exception of the between-groups differences for the VBM analysis, were carried out using Statistical Package for Social Science (SPSS, Version 24.0, IBM Corp.,Armonk, NY.).

4.3 Results

FRDA patients showed an overall impairment in all cognitive tests measuring working memory and visuospatial functions compared to HC, with significant differences that emerged also for PRT and 9HPT, measuring dysarthria and upper limbs dexterity, respectively. A complete list of clinical and demographical information of both groups is available in Table 4.

	FRDA	**HC**	**p-value**
Age *(years; mean* ± SD)	28.4 ±14.1 (range: 14-62)	29.4 ± 9.7 (range: 14-62)	n.s.
Sex (M/F)	13/6	11/9	n.s.
GAA1	719±292.3	n.a.	n.a.
GAA2	960±288.6	n.a.	n.a.
SARA	17±6.7	n.a.	n.a.
PRT	19.7±4.2	32±5.9	<0.001*
9HPT - DH	75.1±64.8	19±9.2	<0.001*
SPART	19.2 ± 5.8	24±3.2	0.034*
SPART-D	6.7 ± 2.3	9±1.7	0.013*
SLD	26.7 ± 2	29±1.5	0.003*
SDMT	36.4 ± 9.1	57±14.4	<0.001*
TMT-A	46.2 ± 25	68±17.9	0.002*
TMT-B	125 ± 61.1	32±3.2	<0.001*

Table 4: Clinical and demographic information of all subjects included in the FRDA study.

FRDA: Friedreich's Ataxia; HC: Healthy Controls; SD, Standard Deviation; SARA: Scale for the Assessment and Rating of Ataxia; PATA rate; 9HPT - DH: 9 Hole Pegboard Test for Dominant Hand; SPART: 10/36 Spatial Recall

Test; SPART-D: 10/36 Spatial Recall Test - Delayed; RAVLT,SLD: Segment Length Discrimination; SDMT: Symbol Digit Modalities Test; TMT: Trail Making Test.*Mann-Whitney Test

Compared to controls, FRDA patients showed a significant reduction of the total cerebellar volume (p=0.004), with the mean volume of all the cerebellar lobules that proved to be lower in FRDA patients, although not always reaching the significance after Bonferroni correction. Indeed, when possible lobular differences were probed, we found a significant reduction of the Lobule IX in FRDA patients (p=0.001), with a borderline volumetric reduction of Crus I and Crus II (both with p=0.009). A complete list of the volumetric analysis is reported in Table 5.

Volumes (mean ± SD)	**FRDA**	**HC**	**p-value**
Total cerebellum	111.5 ± 12.1	125.4 ± 11.9	**0.004**
Lobules I-IV	8.2 ± 0.8	9.1 ± 1.0	0.02*
Lobule V	9.3 ± 0.9	10.2 ± 1.0	0.01*
Lobule VI	19.6 ± 2.1	22.0 ± 2.3	0.01*
Crus I	22.4 ± 3.0	27.3 ± 2.9	0.009*
Crus II	16.7 ± 1.9	19.0 ± 2.0	0.009*
Lobule VIIb	9.1 ± 1.1	10.2 ± 1.0	0.03*
Lobule VIIIa	9.8 ± 1.2	10.9 ± 0.9	0.01*
Lobule VIIIb	7.4 ± 1.0	8.3 ± 0.7	0.01*
Lobule IX	6.0 ± 0.9	7.1 ± 0.9	**0.001**
Lobule X	1.1 ± 0.1	1.2 ± 0.1	0.02*

Table 5: Cerebellar volumes for all subjects included in the analysis.

Volumes are expressed in ml, as mean ± SD.

Significant differences are reported in bold, while the * indicates comparisons not significant after Bonferroni correction.

Interestingly, the VBM analysis showed a pattern of cerebellar atrophy in FRDA patients compared to controls that substantially overlapped with the results of the lobular analysis. Indeed, when the FRDA < HC contrast was probed, a significant cluster of reduced GM density encompassing the entire lobule IX was found (p=0.003), while no differences emerged when the FRDA > HC contrast was tested. Results of the VBM analysis are shown in Figure 23 and Table 6, respectively.

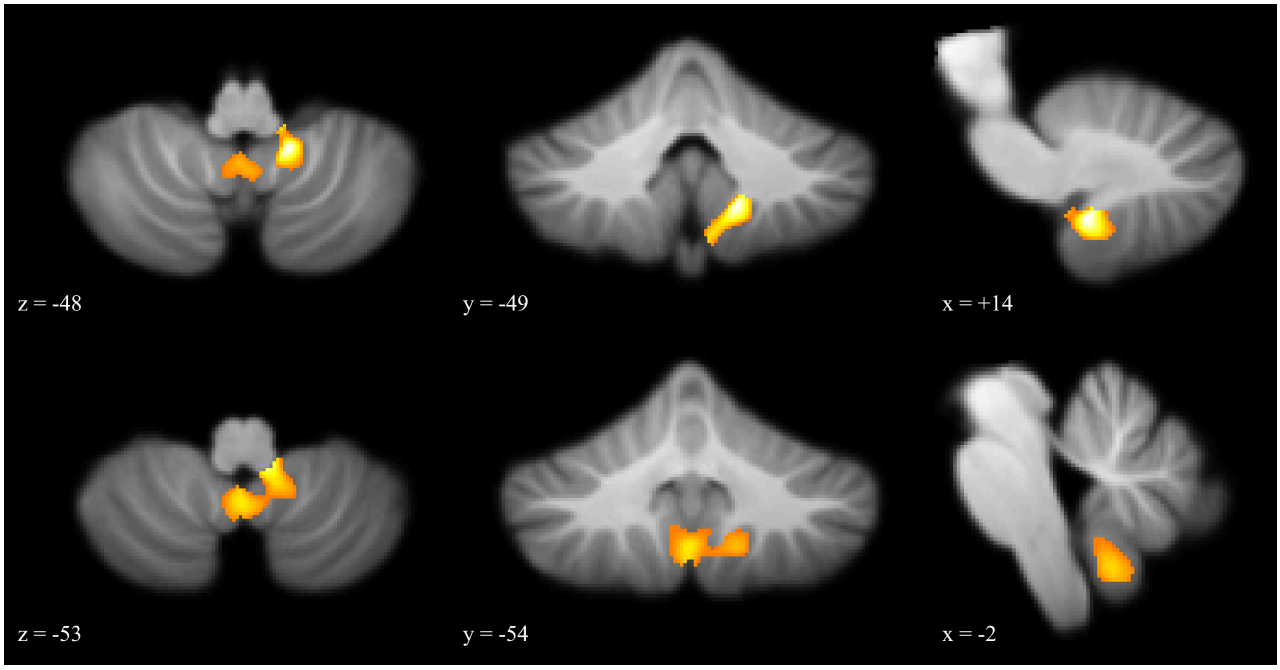

Figure 23: Results of the VBM analysis. The cluster of reduced GM density in FRDA patients compared to HC is superimposed on (from left to right) axial, coronal and sagittal reconstructions obtained from the SUIT T1-weighted cerebellar template. Coordinates refer to millimeters from the anterior commissure in MNI space, with anatomical labeling according to (Tzourio-Mazoyer et al., 2002).

Cluster Volume (ml)	T	$p_{FWE-corr}$	MNI X (mm)	MNI Y (mm)	MNI Z (mm)	Anatomical Label (% Cluster)
1.6	6.16	0.003	14	-49	-48	Right Lobule IX (70%) Left Lobule IX (22%)

Table 6: Results of the VBM analysis.

The cluster of reduced GM density in FRDA patients compared to HC is presented, along with maximum T value and significance level (FWE-corrected at cluster level). No significant differences emerged when testing the FRDA> HC contrast. Coordinates refer to mm from the anterior commissure in MNI space, with anatomical labeling according to (Tzourio-Mazoyer et al., 2002).

When possible correlations between cerebellar lobules volume loss and both motor and cognitive variables were probed, a direct correlation between Lobule IX volume and SLD scores was found (r=0.580, p=0.02). A similar direct correlation was found between the results obtained at the SLD test and the cluster of reduced GM density obtained from the VBM analysis (r=0.520; p=0.03). A scatterplot of the results of both correlation analyses is available in Figure 24. No correlations between MRI data and the remaining clinical variables were found.

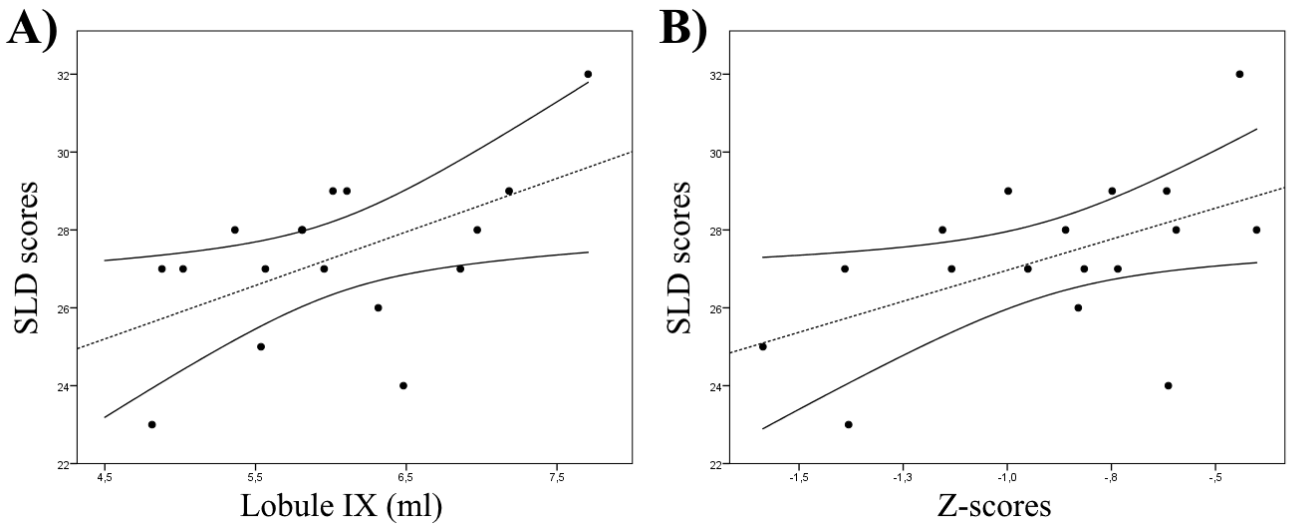

Figure 24: Scatterplot of the correlations between Segment Length Discrimination (SLD) test scores and Lobule IX volume (a) and age- and sex-adjusted z scores extracted from the cluster of reduced GM density obtained at the VBM analysis (b), respectively. Lobule IX volume is expressed in milliliters, while SLD and z scores are dimensionless quantities.

4.4 Discussion

We demonstrated for the first time a direct correlation between cognitive deficits and cerebellar atrophy in FRDA, measured with two different although complementary techniques (D'Mello et al., 2015). In particular, we found a significant and consistent volume loss mainly affecting the posterior lobules of the cerebellum, with a major involvement of the Lobule IX, showing a direct correlation with SLD scores.

FRDA has long been considered a disorder affecting mainly the spinal cord and the DN, with a relative sparing of cerebellar and cerebral hemispheres (Koeppen & Mazurkiewicz, 2013). Nevertheless, a more pronounced CNS involvement in this condition has been recently reassessed by different neuroimaging studies, suggesting a widespread degree of supra- and infratentorial involvement in FRDA (Clemm von Hohenberg et al., 2013; Della Nave et al., 2011; Della Nave, Ginestroni, Tessa, et al., 2008; Harding, Corben, et al., 2016; Harding, Raniga, et al., 2016; Rezende et al., 2016; Selvadurai, Harding, Corben, & Georgiou-Karistianis, 2018; Selvadurai et al., 2016; Stefanescu et al., 2015; Vavla et al., 2018). With particular reference to the occurrence of GM atrophy, previous works demonstrated the presence of a significant volume loss affecting the cerebrum, with clusters of reduced cortical volumes in different prefrontal areas, as well as in the supplementary motor area and in the precuneus (Selvadurai et al., 2016). Furthermore, clusters of reduced GM density have been also described at the level of other supratentorial areas, such as the occipital cortex, the precentral gyrus and the middle temporal gyrus (Rezende et al., 2016).

Along with supratentorial regions, a significant atrophy of the cerebellar cortex has also been demonstrated in FRDA, with progressive GM loss mainly involving the posterior lobe of the cerebellum (Selvadurai et al., 2016; Vavla et al., 2018), with a relatively minor involvement of the anterior cerebellar regions (Della Nave, Ginestroni, Giannelli, et al., 2008). Our results are in line with previous studies showing a more pronounced atrophy occurring in posterior cerebellar regions, and in particular of the Lobule IX. This region, although mainly contributing to the execution of

different non-motor tasks, as demonstrated in both animals and humans studies (Deluca et al., 2014; Handel, Thier, & Haarmeier, 2009; Jokisch, Troje, Koch, Schwarz, & Daum, 2005; Salmi et al., 2010), takes also part in the dynamic control of attentive processes, being embed in the delicate interaction between ventral/dorsal attentive network and oculomotor circuits. In particular, Lobule IX seems to be specifically involved in the oculomotor error tracking and motor reorientation to unexpected events (Stephen, Elizabeth, & Christophe, 2018). It is therefore understandable how, although not completely damaged, visuo-spatial abilities could be at least in part compromised in case of loss of Lobule IX integrity. This hypothesis has further been confirmed by Lupo and colleagues, who reported a case in whom a ruptured cerebellar arteriovenous malformation damaged the posterior vermis including part of Lobule IX, with subsequent attention and visuo-spatial domains impairment (Lupo et al., 2018). Similarly, as reported in a different range of congenital pathologies affecting the vermis (e.g. fragile X syndrome, William's syndrome, Dandy-Walker spectrum), alterations in Lobule IX often result in defective attentive and learning processes (Steinlin, 2008).

An involvement of Lobule IX, correlating to the presence of cognitive symptoms, is also observed in different hereditary ataxias. A significant volume loss has been reported in Spinocerebellar Ataxia (SCA) Types 1 (Jacobi et al., 2013), 2 (Cocozza et al., 2015; Jung et al., 2012; Olivito et al., 2018), 3 (Hernandez-Castillo, Diaz, Campos-Romo, & Fernandez-Ruiz, 2017), 7 (Hernandez-Castillo, King, Diedrichsen, & Fernandez-Ruiz, 2018; Rub et al., 2008) and 17 (Reetz et al., 2012), showing some degree of correlation with disease severity (Hernandez-Castillo et al., 2018), motor impairment (Hernandez-Castillo et al., 2017) and cognitive scores (Olivito et al., 2018). Whereas spatial degeneration pattern can be used for differential diagnosis and traced back to specific SCA subtypes (Hernandez-Castillo et al., 2018), differences in clinical symptoms are still more controversial with highly variable phenotypes. Finally, similar considerations can be also applied to Ataxia-Teleangiectasia patients (Hoche et al., 2014), with the difference that cerebellar structural

correlates of visuo-spatial dysfunctions are still largely unknown in this condition, and valuable of future research.

All these evidences can be partly explained considering that the posterior lobe is involved in visual computation, as shown by studies documenting a severe impairment in global motion discrimination task, independent from fixation disturbances, in patients with posterior cerebellar lesions (Handel et al., 2009). Similarly, subjects with focal posterior cerebellar lesions show a reduction in visual perceptual learning (Deluca et al., 2014). These findings could be at least in part explained by the inter-connections between the posterior cerebellum and frontal, prefrontal and parietal regions, including the dorso-lateral prefrontal area and the intraparietal sulcus, as these areas are known to be involved in the decision-making process of visual motion (Gold & Shadlen, 2007; Kelly & Strick, 2003).

As further confirmation of its implication in cognitive processes, different functional connectivity studies have demonstrated a central role of Lobule IX in cortico-cerebellar and intra-cerebellar circuits. RS-fMRI studies conducted on HC showed that this cerebellar lobule is part of the DMN (Habas et al., 2009; Sang et al., 2012). Interestingly, Lobule IX was suggested to be not only a part of the DMN, but also part of other networks, such as the Visual Network, the Sensorimotor Network and the Dorsal Attention Network (Liu et al., 2017; Sang et al., 2012), with the latter known to contribute to saccade planning, modulation of externally oriented attention and to visual working memory (Jerde, Merriam, Riggall, Hedges, & Curtis, 2012). A recent study by Guell and colleagues showed that Lobule IX, as part of the third non-motor representation, seems to be functionally located to a less extreme level of information processing and unfocused task (Guell, Schmahmann, Gabrieli, & Ghosh, 2018). This could explain why Lobule IX volumes correlate with performances on SLD but not with any other test, as these latter need to engage different cerebro-cerebellar areas to be performed.

These hypotheses concerning the involvement of Lobule IX in the development of the clinical phenotype in FRDA patients are part of a more complex framework and previous works

demonstrated that global cerebellar volume in FRDA does not significantly differ from HC, although mild grey matter lobular atrophy develops beyond normal aging. The pattern of lobular alteration is still largely undetermined, with some evidences suggesting a prominent atrophy of lobule VI (Lindig et al., 2019), whereas other evidences suggest a more pervasive volume reduction in vermis, dentate, and posterior lobes (Della Nave, Ginestroni, Giannelli, et al., 2008; Selvadurai et al., 2016), with functional rearrangements (Cocozza et al., 2018; Vavla et al., 2018). For these reasons, future comprehensive studies investigating atrophy pattern, functional and structural changes are warranted.

Visual perception has been poorly investigated in FRDA, with few conducted studies that led to conflicting results. Nachbauer and colleagues found no differences between FRDA and HC on two subtests of Visual Object and Space Perception (VOSP) test, one requiring the identification of incomplete letters and the other requiring the discrimination of the spatial position of single dots (Nachbauer et al., 2014). However, they found that performances on visual attention cognitive tasks were lower in patients compared to controls, assuming that oculomotor problems could have influenced reaction times. On the other hand, in a different study a widespread involvement of visual perception functions was reported in FRDA patients compared to HC (Cocozza et al., 2018). In the present study we cannot fully establish if the lower performances at the SLD test in FRDA patients rose from impaired oculomotor movements or from a significant cognitive impairment occurring in FRDA. Nieto and colleagues found that performances on Face Recognition Test, but not on Judgment Line Orientation task, were lower in FRDA compared to HC, and that these performances could not be explained based on oculomotor impairments (Nieto et al., 2012). Interestingly, in the present study we observed an opposite cognitive pattern. However, it has to be noted that SLD assesses this function by confronting two segments that frequently differ in a subtle way. This requires both spared abilities of fixation and voluntary control of eye movements to a fine visual discrimination. Given that Lobule IX lesions seem to be associated to head-shaking nystagmus (Huh & Kim, 2011), smooth pursuit and gaze-holding impairments (Lee et al., 2014),

atrophy of this cerebellar lobule may contribute to the development of eye movements alterations, which in turn could lead to the low performances at specific cognitive tests. Similarly, perceptive and attentional skills are required, regardless of eye movements integrity. For these reasons, future studies should both measure oculomotor deficits and introduce tests difficulty gradients in the tests, as reported in (Nieto et al., 2012), and should correlate these features in order to better appreciate the involvement of motor and cognitive components.

In this work we failed to find any significant correlation between motor scores and MRI results. Nevertheless, the lack of correlation between Lobule IX volume loss and motor scores it is not surprising, as such clinical scale cannot be immediately linked to cerebellar atrophy, but may be more related to dorsal root ganglion degeneration, or to other more complex functional links.

An additional limitation of the present study is the relatively small sample size of patients, as often occurs when dealing with rare diseases. Furthermore, no information about microstructural cerebellar integrity were available, which are known to occur in this condition (Della Nave, Ginestroni, Tessa, et al., 2008; Vavla et al., 2018). Integration with cerebellar volumetric and microstructural data is needed, to assess not only the relation between these altered MRI metrics, but also their possible different contribution to the development of cognitive dysfunctions. Finally, to further confirm the possible central role of Lobule IX atrophy in determining cognitive alterations in FRDA, future studies directly comparing cerebellar volumes between these subjects and ataxia patients showing a relative cognitive preservation (i.e. SCA6) are also warranted.

Although characterized by these limitations, this study demonstrates the presence of a significant volume loss occurring in the posterior cerebellar lobe of FRDA patients, consistent across by two different image analysis techniques and involving the Lobule IX. Atrophy of this specific cerebellar region correlates with worse visuo-spatial abilities as measured with the SLD test, further expanding our knowledge about the complex physiopathology of cognitive deficits in FRDA.

CHAPTER 5

Cerebellar cortex involvement in Idiopathic Cervical Dystonia

5.1 Background

Idiopathic Cervical Dystonia (ICD) is a chronic neurologic disorder characterized by involuntary sustained contractions of cervical musculature resulting in abnormal movements or postural changes of the head, neck and shoulders (Albanese et al., 2011). Considered as a disorder of motor programs controlling semiautomatic movements or postures (Kaji, Bhatia, & Graybiel, 2018), it represents the most common of the adult-onset focal dystonias (Defazio, Abbruzzese, Livrea, & Berardelli, 2004). Despite the number of investigations on ICD pathogenesis has grown considerably over the past decades, its exact physiopathological substratum remains largely unknown (Bologna & Berardelli, 2017; Kaji et al., 2018). Originally classified as a basal ganglia disease, it is now regarded as a network disorder due to abnormalities not only in the basal ganglia, but also in other interconnected structures including the cerebral cortex and the cerebellum (Bologna & Berardelli, 2017; Esposito et al., 2017; Kaji et al., 2018; Shakkottai et al., 2017). Preliminary evidences from animal models and human clinic-pathological observations have been confirmed by a growing number of experimental neurophysiological and neuroimaging investigations which demonstrated the association between dystonia and alterations of cerebellar activity, connectivity and structure (Bologna & Berardelli, 2017; Esposito et al., 2017; Kaji et al., 2018; Shakkottai et al., 2017). Regarding structural abnormalities, VBM studies reported variable volumetric changes in the cerebellum of dystonic patients (Draganski, Thun-Hohenstein, Bogdahn, Winkler, & May, 2003; Piccinin, Piovesana, et al., 2014; Piccinin, Santos, et al., 2014). However, to date, a consistent pattern of cerebellar morphometric alterations in ICD patients has not yet been established. Furthermore, no data exist on the distinct involvement of specific cerebellar lobules and

of cerebellar peduncles, which could explain the role of different morphofunctional subunits in ICD pathophysiology, thus helping unravel the nature of cerebellar pathology in these patients.

From this background, aim of our study was to investigate the presence of volumetric alterations of cerebellar GM and WM in ICD patients using both ROI-based and voxel-based approaches, as well as their possible contribution to clinical impairment in this condition.

5.2 Methods

Participants

In this prospective cross-sectional study right-handed patients with ICD (Albanese et al., 2011) along with age- and sex-comparable right-handed HC were enrolled from the University "Federico II" (Naples, Italy - Site 1) and the IRCCS "Fondazione Don Gnocchi" (Milan, Italy - Site 2). Exclusion criteria included: age<18 years and the presence of any other relevant neurologic/psychiatric disease or systemic condition that could affect the CNS. All patients were receiving botulinum neurotoxin (BoNT) injections following standard treatment regimens (Albanese et al., 2011) and underwent the MRI examination during the wearing-off phase, before receiving the treatment. Within one week from MRI, patients were clinically assessed, and the following variables were obtained: total Tsui score (Tsui, Eisen, Stoessl, Calne, & Calne, 1986) as an overall measure of the severity of symptoms, DD and duration of BoNT treatment.

MRI data acquisition and analysis

All images were acquired using two different MRI scanners (3T Trio and 1.5T Avanto, Siemens Healthineers). The acquisition protocol included, for Site 1 a 3D MPRAGE (TR=1900ms; TE=3.4ms; TI=900ms; Flip Angle=9°; resolution=1x1x mm^3; 160 axial slices) and a 2D FLAIR (TR=8500ms; TE=106ms; TI=2500ms; Flip Angle=150°; voxel size=0.9x0.9x4 mm^3; 25 axial slices), while for Site 2 a 3D MPRAGE (TR=1900ms; TE=3.37ms; TI=1100ms; Flip Angle=9°; resolution=1x1x1mm^3; 176 sagittal slices) and a 2D dual-echo sequences (Proton Density-weighted and T2-weighted turbo spin echo sequence; TR=5550ms; TE=23/103ms; resolution=0.8x0.8x3mm^3; 45 axial slices) were acquired.

Before image processing, an experienced preliminarily checked both sequences to exclude the presence of posterior fossa lesions or malformations.

For all subjects included in the analysis, global and lobular cerebellar GM volumes were calculated on 3D T1-weighted images SUIT, with the same procedure reported in Chapter 4.2 (on page 74). A

similar approach was adopted in order to obtain an atlas-based segmentation of cerebellar peduncles using a diffusion MRI-based probabilistic atlas of the cerebellar WM obtained from tractography data of 90 subjects participating in the Human Connectome Project mapped onto a common reference space (SUIT atlas space) (van Baarsen et al., 2016). This atlas provides probability maps of each cerebellar peduncle: each voxel value ranges from 0 to 1 and represents the proportion of subjects in which that same voxel was part of the bundle. Thus, we thresholded the probability of each cerebellar peduncle at 0.5 in order to obtain binary ROIs corresponding to the superior, middle and inferior cerebellar peduncles. Finally, the same inverse transformation matrix derived from the previously described processing steps was used to warp cerebellar peduncles ROIs in each subject's native space and compute individual bilateral peduncular volumes. As a quality check, an expert visually inspected the outcome of the registrations to exclude CSF contamination (Figure 25).

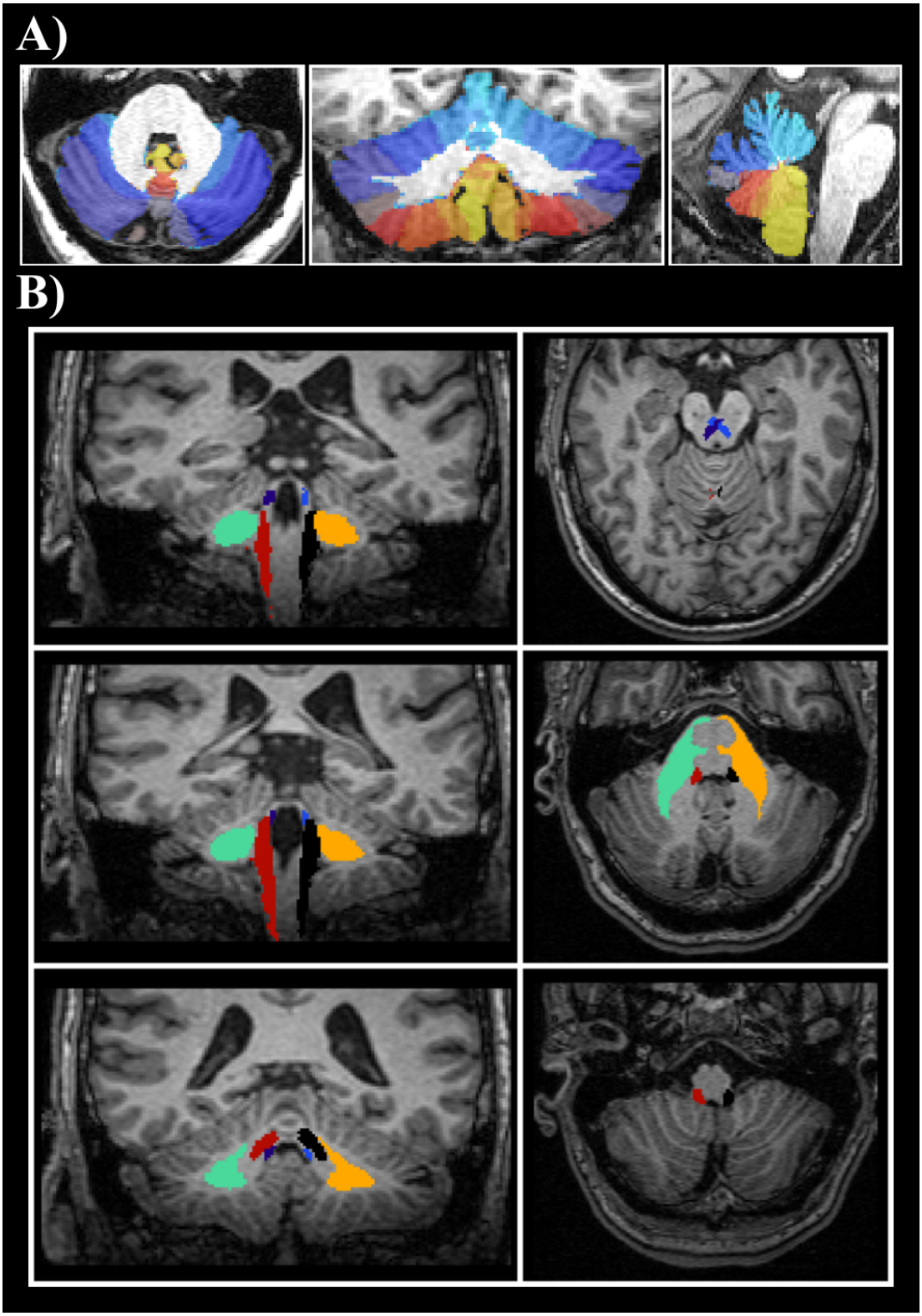

Figure 25: Results of the segmentation of cerebellar lobules and peduncles. (A) In a 53-year-old female patient, the SUIT cerebellar atlas is aligned in the native subject space and superimposed on (from left to right) axial, coronal and sagittal reconstructions obtained from the 3D T1-weighted sequence. (B) In a 54-year-old male patient, atlas-derived cerebellar peduncles ROIs are aligned in the native subject space and superimposed on coronal (left column) and axial (right column) reconstructions obtained from the 3D T1-weighted sequence.

Furthermore, to investigate possible local volume differences at a voxel level, VBM analyses (Ashburner & Friston, 2000) were also carried out. In particular, normalized GM maps were modulated by scaling by the inverse of the amount of the volume changes due to spatial registration, in order to preserve the local GM amount, and then spatially smoothed using a 1mm FWHM isotropic Gaussian kernel (Smith & Nichols, 2009). The same procedure was also applied to normalized WM maps.

Finally, for each subject, the ICV was also estimated using the standard procedure implemented in the CAT12 and used as confound in subsequent statistical analyses in order to correct for the effect of individual head size. To exhaustively investigate the possible effect of scanner field strength on cerebellar volumes, additional image quality assessment and subgroup volumetric analyses were also performed on scans from the two sites. In particular, comparisons of cerebellar volumes (at both ROI-based and voxel-based levels) between ICD patients and HC were repeated separately for each center.

Statistical analysis

Unless otherwise specified, all analyses were carried out using Statistical Package for Social Science (IBM SPSS Statistics 25), with a significance level set at $p \leq 0.05$, corrected for the false discovery rate (FDR) using the Benjamini-Hochberg procedure. Assumptions for parametric tests were preliminarily checked, with normality of continuous variables assessed via the Shapiro-Wilk's test.

Differences between ICD and HC groups in terms of age, sex and scanner's field strength were probed by Student's t and Pearson's χ^2 tests, respectively.

Group differences regarding cerebellar ROI volumes were tested by ANCOVA analyses, including age, sex, scanner and TIV as confounding covariates. The interaction term scanner (1.5T vs 3T) per group (ICD vs HC) was included in the model to test the possible influence of scanner field strength on between-group volume differences. As an ancillary analysis, between-group differences were

also assessed separately for each lobule's right, left and vermian portions, as well as for each peduncle's right and left side, in order to investigate possible lateralized effects.

For the VBM analysis, the normalized, modulated and smoothed GM and WM maps were statistically analyzed to assess local volume differences between the two groups using a nonparametric approach based on permutations applied to the general linear model (Winkler, Ridgway, Webster, Smith, & Nichols, 2014) via SPM's Threshold Free Cluster Enhancement (TFCE) toolbox (http://www.neuro.uni-jena.de/tfce), including age, sex, ICV and scanner as confounding variables. Five thousand permutations were generated, and cluster-like structures were enhanced using the TFCE approach (Smith & Nichols, 2009), with a significance level set at $p \leq 0.05$, corrected for multiple comparisons across space using the family-wise error rate (FWER), and an extent-threshold $k=50$ voxels to avoid false positive results.

When regional differences in terms of local GM or WM volume emerged between the two groups, the corresponding first eigenvariate was extracted from the cluster and corrected for the effect of age, sex, ICV and scanner in HC: for each metric, the linear relationship with these variables was modeled in the HC group and used to compute standardized residuals in all subjects. The relationship between the so obtained Z-scores and clinical variables was assessed via linear (total Tsui score, DD, BoNT treatment duration) and binary logistic (tremor) regression analyses, validated using the bootstrap method with 5000 replications. Likewise, adjusted Z-scores of other cerebellar volumes that emerged as significantly different at the between-group ROI analyses were entered in similar regression analyses. Significance level for regression models was not adjusted for multiple testing given the exploratory nature of the analyses.

5.3 Results

Participants

27 patients with ICD (mean age 50.4±11.3 years, F/M=14/13) and 27 HC of comparable age and sex (mean age 51.7±11.5 years, F/M=14/13) were enrolled in the study from the University "Federico II" (12 ICD: mean age 50.1±14.0 years, F/M=5/7; 12 HC: mean age 50.3±14.3 years, F/M=5/7) and the "Don Gnocchi" Foundation (15 ICD: mean age 50.6±9.0 years, F/M=9/6; 15 HC: mean age 52.8±9.0 years, F/M=9/6). Mean DD for ICD patients was 7.1 years (standard deviation: 6.3), with a median Tsui score of 8 (interquartile range: 5 - 10). Tremor was present in 12 (out of 27) patients.

Between-group comparisons

When investigating possible differences in terms of cerebellar GM volumes, ICD patients showed a significant volumetric reduction of the anterior cerebellum compared to HC (15.4±1.5 vs 16.1±1.5, ICD vs HC; p=0.006, FDR-adjusted p=0.05). At a lobular level, ICD patients demonstrated significant atrophy of cerebellar lobules I-IV (7.0±0.6 vs 7.3±0.7, ICD vs HC; p=0.004, FDR-adjusted p=0.05), V (8.4±0.9 vs 8.8±0.8, ICD vs HC; p=0.01, FDR-adjusted p=0.05) and VI (19.6±2.1 vs 20.5±1.8, ICD vs HC; p=0.009, FDR-adjusted p=0.05) (Table 7).

Volumes	ICD (N=27)	HC (N=27)	Cohen's *d*	Uncorrected *p* (FDR-adjusted *p*)
Cerebellum	121.5±11.0	124.8±9.4	0.62	0.05* (0.12)
Anterior Lobe	15.4±1.5	16.1±1.5	0.87	**0.006 (0.05)**
Posterior Lobe	106.1±9.5	108.7±8.1	0.56	0.07 (0.13)
Lobules I-IV	7.0±0.6	7.3±0.7	0.91	**0.004 (0.05)**
Lobule V	8.4±0.9	8.8±0.8	0.78	**0.01 (0.05)**
Lobule VI	19.6±2.1	20.5±1.8	0.83	**0.009 (0.05)**
Crus I	26.9±2.8	27.5±2.4	0.50	0.11 (0.18)
Crus II	20.0±1.7	20.2±1.7	0.23	0.44 (0.49)
Lobule VIIB	10.3±1.0	10.6±0.9	0.42	0.17 (0.21)
Lobule VIIIA	11.2±1.0	11.5±0.8	0.50	0.11 (0.18)
Lobule VIIIB	9.0±0.8	9.2±0.6	0.45	0.14 (0.19)
Lobule IX	7.4±0.8	7.6±0.7	0.23	0.45 (0.49)
Lobule X	1.8±0.2	1.8±0.1	0.04	0.89 (0.90)
SCP	0.7±0.1	0.7±0.1	0.63	0.04 (0.11)*
MCP	9.5±0.9	9.9±1.1	0.67	0.03 (0.10)*
ICP	3.0±0.3	3.1±0.3	0.59	0.06 (0.13)

Table 7. Volumes for all subjects included in the ICD analysis.

Volumes of cerebellar lobules (considered as the sum of right, left and vermian portions) and peduncles (considered as the sum of right and left components) are presented, along with the effect sizes (Cohen's *d*) and *p*-values of the between-group differences. Cerebellar Volumes (in ml) are expressed as mean ± SD. Significant differences are reported in bold. *Not significant after FDR-correction.

ICD, Idiopathic Cervical Dystonia; HC, Healthy Controls; SCP, Superior Cerebellar Peduncle; MCP, Middle Cerebellar Peduncle; ICP: Inferior Cerebellar Peduncle.

Regarding cerebellar WM tracts, ICD patients showed reduced volume of the bilateral superior (0.7±0.1 vs 0.7±0.1, ICD vs HC; p=0.04) and middle (9.5±0.9 vs 9.9±1.1, ICD vs HC; p=0.03) cerebellar peduncles, which did not retain statistical significance after correcting for multiple comparisons (Table 7). There was no significant effect of the scanner per group interaction term. The ancillary analysis demonstrated nearly symmetrical cerebellar GM and WM atrophy patterns, with slight right-side predominance (data not show).

At the VBM analyses, clusters of reduced GM volume in both right (FWER-corrected p=0.01) and left (FWER-corrected p=0.04) cerebellar lobules IV, V and VI emerged in ICD patients compared to HC (Table 8, Figure 26A), along with small clusters of reduced WM volume in the right cerebellum (FWER-corrected p=0.04) and the left midbrain (FWER-corrected p=0.04) (Table 8, Figure 26B). No significant between-group differences emerged for the ICD>HC contrast.

	Cluster Volume (ml)	*p*-value (FWE-corr)	Cohen's *d*	T	MNI Coordinates (mm)			Anatomical Label
					X	Y	Z	
GM	9.70	0.01	1.33	4.61	25	-72	-20	Right Cerebellar Lobule VI
		0.01	1.38	4.77	14	-52	-13	Right Cerebellar Lobules IV-V
	2.01	0.04	1.00	3.47	-8	-60	-11	Left Cerebellar Lobules IV-V
		0.04	1.02	3.54	-15	-58	-25	Left Cerebellar Lobule VI
WM	0.09	0.04	1.34	4.26	24	-62	-31	Right Cerebellum
	0.39	0.04	1.09	3.76	-12	-18	-13	Left Midbrain

Table 8. Results of the voxel-based analyses.

Clusters of decreased GM and WM volume in ICD patients compared to HC are presented, along with significance level (FWE-corrected) and the corresponding local maxima's effect sizes, T values and anatomical labels. No significant differences emerged when testing the ICD > HC contrast. Coordinates refer to mm from the anterior commissure in MNI space, with anatomical labeling according to (Tzourio-Mazoyer et al., 2002).

GM, Gray Matter; WM, White Matter; ICD, Idiopathic Cervical Dystonia; HC, Healthy Controls.

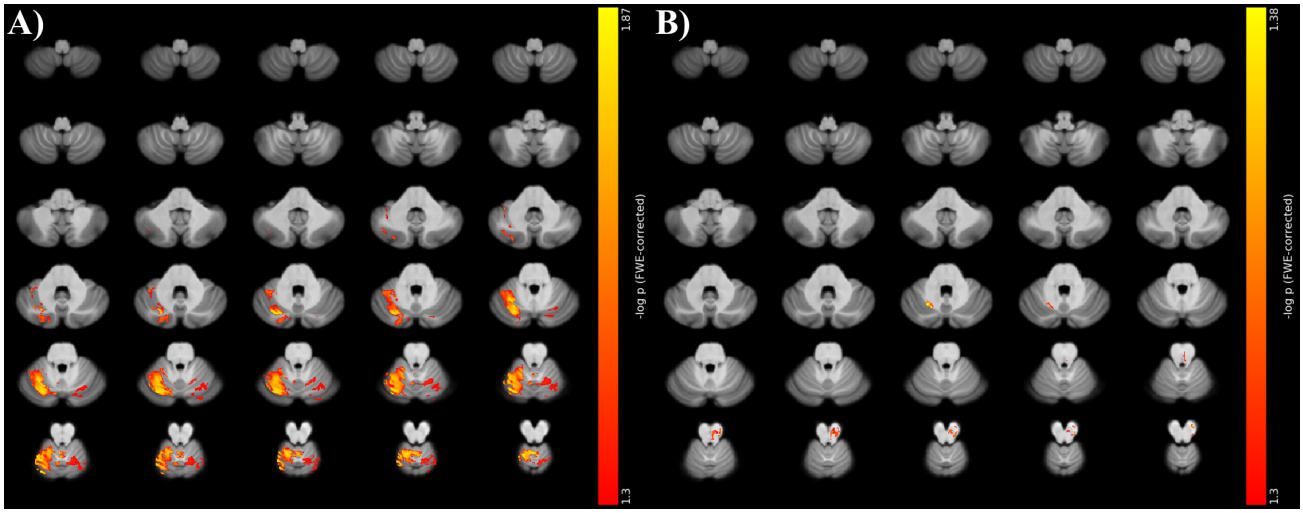

Figure 26: Results of the voxel-based analyses. Thresholded statistical maps (in red-yellow) for the ICD < HC contrast regarding GM (A) and WM (B) volumes are superimposed on the SUIT T1-weighted template in axial planes. ICD, Idiopathic Cervical Dystonia; HC, Healthy Controls.

Relationship between MRI features and clinical data

When exploring the clinical correlates of the observed MRI alterations, no significant relationship was found between MRI metrics and either the total Tsui score, DD or BoNT treatment duration, with an association between the presence of tremor and the bilateral middle cerebellar peduncle volume (Nagelkerke $R^2 = 0.190$, $p = 0.04$; $B = 0.736$ [bias-corrected and accelerated bootstrap 95% confidence interval = - 0.137 to 2.491, $p = 0.04$]).

5.4 Discussion

We investigated the presence of possible structural modifications in the cerebellum of ICD patients, demonstrating a specific spatial pattern of decreased cerebellar GM and (to a lesser extent) WM volumes, resulting from both ROI-based and voxel-based analyses.

In recent years, modifications of cerebellar structure and function have gained increasing attention as a possible physiopathological substratum of primary dystonia, which has been the object of a paradigm shift: from being considered a basal ganglia disease to a complex network disorder involving cerebellar, cortical and subcortical motor (and non-motor) areas, along with their reciprocal connections (Bologna & Berardelli, 2017; Kaji et al., 2018; Shakkottai et al., 2017).

Nevertheless, discordant evidence exists regarding volumetric changes in the cerebellum of dystonic patients, with several structural MRI studies variably reporting increases (Draganski et al., 2003; Obermann et al., 2007; Ramdhani et al., 2014), decreases (Piccinin, Piovesana, et al., 2014; Piccinin, Santos, et al., 2014), or no modifications (Egger et al., 2007; Pantano et al., 2011; Prell et al., 2013) of cerebellar GM volumes, with inconstant spatial patterns. This apparent inconsistency may be attributable to different factors, including small size and heterogeneity of the patient cohorts (often including different types of focal or segmental dystonia (Egger et al., 2007; Obermann et al., 2007; Piccinin, Piovesana, et al., 2014; Piccinin, Santos, et al., 2014; Ramdhani et al., 2014), and methodological differences (with most studies using whole-brain rather than cerebellum-oriented approaches (Draganski et al., 2003; Egger et al., 2007; Obermann et al., 2007; Pantano et al., 2011; Prell et al., 2013; Ramdhani et al., 2014), all severely hindering meaningful comparisons between studies.

In our work, we focused on a homogenous sample of ICD patients, using cerebellum-tailored analyses with complementary ROI-based and voxel-based approaches, both demonstrating consistent volume loss of cerebellar GM at the level of the anterior lobe and lobule VI in patients compared to HC. Of note, these results partially overlap with those of a recent study adopting a

similar cerebellum-oriented approach (Piccinin, Santos, et al., 2014), which has proven to be more sensitive and accurate compared to whole-brain analyses for the characterization of infratentorial structural abnormalities (Diedrichsen, 2006). Interestingly, a slight right-side predominance emerged at both the ROI-based and voxel-based analyses, in accordance with the already reported asymmetry of brain imaging findings in this condition (Draganski et al., 2003; Pantano et al., 2011). According to the topographic organization of the cerebellum, lobules of the anterior lobe and lobule VI contain the representation of sensorimotor functions, participating in the coordination of fine movements of the extremities as well as in the control of posture and gait (Stoodley & Schmahmann, 2010). These regions, densely connected with spinal cord, brainstem and cerebral cortical areas involved in sensorimotor processing, show a precise somatotopic arrangement (Stoodley & Schmahmann, 2010). Interestingly, for both sensory projections carrying cutaneo-kinesthetic information via the trigemino-cerebellar tracts and afferent and efferent branches of the motor cortico-ponto-cerebello-thalamic-cortical loop, the representation of the head/neck and face/mouth lies principally in lobule VI, with some extension into lobules V and IV (Mottolese et al., 2013; Stoodley & Schmahmann, 2010). In this light, the observed volume loss in the cerebellum may express the selective vulnerability of specific cerebellar cortical areas containing the representation of the affected body parts (head/neck for ICD patients), demonstrating a link between cerebellar involvement and the topography of dystonic symptoms (Bologna & Berardelli, 2017; Kaji et al., 2018). However, it remains unclear if cerebellar cortical atrophy represents a primary abnormality or a secondary effect resulting from damage in other salient supratentorial areas and/or in projection tracts interconnecting them, which has been also demonstrated in ICD patients (Lehericy, Tijssen, Vidailhet, Kaji, & Meunier, 2013).

In order to explore the afferent and efferent connections of the cerebellum, we also investigated possible cerebellar WM structural modifications, demonstrating a slight volumetric reduction (not surviving multiple comparisons correction) of the middle and superior cerebellar peduncles, containing the main afferent and efferent branches of the cortico-ponto-cerebello-thalamo-cortical

loop, respectively (Lehericy et al., 2013). These results are in line with previous studies reporting microstructural damage of cerebellar peduncles in dystonic patients (Carbon, Kingsley, Tang, Bressman, & Eidelberg, 2008), and support the hypothesis of a sensorimotor network disorder, underpinned by structural and functional modifications involving different nodes at the level of cerebral cortex, basal ganglia and cerebellum, as well as their reciprocal connections (Bologna & Berardelli, 2017; Kaji et al., 2018; Shakkottai et al., 2017).

When looking at the relationship between the observed structural modifications and clinical variables, a positive correlation emerged between the volume of the bilateral middle cerebellar peduncles and the presence of tremor. These results are in contrast with findings in other tremorous conditions (mainly essential tremor), in which an association between tremor and cerebellar peduncles' macro- and micro-structural damage has been described (Novellino et al., 2016), suggesting that cerebellar involvement contributes to the genesis of tremor in cervical dystonia through distinct physiopathological mechanisms (Hvizdosova et al., 2020). Regarding the relationship with BoNT treatment, which has been anecdotally linked to changes in brain structure (Blood et al., 2006), no significant association between treatment duration and cerebellar atrophy emerged, possibly due to the low variance of BoNT treatment duration in our sample.

Some limitations of the present study need to be acknowledged. Firstly, MRI exams were acquired at different field strengths, introducing a possible source of bias. However, demographic and clinical characteristics of the subjects examined with the two scanners were highly homogeneous, and all statistical analyses included field strength as a confounding variable, thus greatly limiting possible scanner-related bias and even increasing the generalizability of our results. Furthermore, a more extensive clinical examination including finer evaluations of motor, as well as sensory, cognitive, neuropsychiatric and autonomic domains may have allowed for greater insight into the contribution of cerebellar modifications to the development of motor and non-motor symptoms, which are known to occur in dystonic patients (Kuyper, Parra, Aerts, Okun, & Kluger, 2011). The implementation of other advanced MRI techniques focusing on the analysis of brain structural and

functional connectivity could have helped interpret the observed cerebellar modifications in the framework of a more complex network disorder (Bologna & Berardelli, 2017; Kaji et al., 2018; Shakkottai et al., 2017). Finally, a longitudinal evaluation might have provided the means to unravel the causal relationship between cerebellar, cortical, basal ganglia and interconnecting WM tracts abnormalities, as well as to investigate the potential reversibility of brain structural modifications in response to BoNT treatment

In conclusion, these data show evidence of a specific pattern of cerebellar structural abnormalities in ICD patients, with volume loss mainly involving cortical GM of the anterior cerebellum and lobule VI, consistent across both ROI-based and voxel-based approaches and seemingly related to the somatotopic representation of the affected body parts. These results, notwithstanding the abovementioned limitations, may shed novel light on the nature of cerebellar modifications in ICD and their role in the physiopathology of this condition.

CHAPTER 6

Cerebellar cortex involvement in Multiple Sclerosis

6.1 Background

We have discussed how the cerebellum is a complex structure, functionally integrated in several cognitive and behavioral circuits through substantial projections to cerebral association areas. Although classifications of morphologic, phylogenetic and functional order can be applied to characterize the cerebellar structure, according to anatomical and functional studies two main domains can be topographically identified, with the anterior cerebellum involved in motor tasks and the posterior cerebellum responsible for cognitive functions (Stoodley & Schmahmann, 2010). An increasing body of evidence suggests that cerebellar damage impacts high order functions, contributing to cognitive dysfunctions in several psychiatric and neurological disorders (Koziol et al., 2014; Mormina et al., 2017). The cerebellum is a predilection site of pathology in MS patients and contributes not only to the accumulation of physical disability (Inglese et al., 2017) but also to the development of cognitive deficits in both the relapsing (Moroso, Ruet, Lamargue-Hamel, Munsch, Deloire, Coupe, Ouallet, et al., 2017) and progressive phase of the disease (Cocozza et al., 2017; D'Ambrosio et al., 2017; Weier, Penner, et al., 2014).

RS-fMRI is a non-invasive powerful tool that allows for the evaluation of FC between different brain regions when a subject is not performing any specific task. Previous RS-fMRI studies in MS patients have shown the presence of functional disruption in local (Dogonowski et al., 2014) and long-range cerebellar FC not only within the cerebellar network (Cirillo et al., 2016; Rocca et al., 2017; Sbardella et al., 2017) but also in the context of the sensory-motor and attentional/working memory networks (Loitfelder et al., 2012; Petracca et al., 2017; Rocca et al., 2017). Such FC rearrangements have been related to the presence of structural damage (Cirillo et al., 2016;

Dogonowski et al., 2014; Petracca et al., 2017; Rocca et al., 2012; Rocca et al., 2017), and can be interpreted, according to the disease stage, as a sign of cortical plasticity and functional compensation, as a consequence of the exhaustion of such compensatory mechanisms or as a maladaptive rewiring of resting state networks (Cirillo et al., 2016; Petracca et al., 2017; Rocca et al., 2017; Schoonheim, Meijer, & Geurts, 2015). Although it is clear that clinically eloquent modifications of cerebellar FC occur in the posterior cerebellar lobe of patients with MS (Dogonowski et al., 2014; Loitfelder et al., 2012; Petracca et al., 2017; Rocca et al., 2017) and that damage of specific cerebellar lobules differentially contributes to cognitive disability in all disease phenotypes (Cocozza et al., 2017; Grothe, Lotze, Langner, & Dressel, 2017; Moroso, Ruet, Lamargue-Hamel, Munsch, Deloire, Coupe, Charre-Morin, et al., 2017; Moroso, Ruet, Lamargue-Hamel, Munsch, Deloire, Coupe, Ouallet, et al., 2017), no data is available about FC abnormalities of individual cerebellar lobuli and the potential impact on the cognitive status in MS. In the present study we focused on the investigation of patients with progressive MS (PMS), more likely to experience cognitive deficits and cerebellar damage, in order to further understand the physiopathological bases of cognitive deficits in MS. Therefore, the aims of our study were:

(i) to investigate cerebellar lobular FC taking into account the presence of cerebellar structural damage

(ii) to test the relationship between FC rearrangements and cognitive performance.

6.2 Methods

Participants

Thirty-five patients with PMS (mean age 50.7±11.6 years; range 29-72 years; M/F:13/22) were prospectively enrolled along with 22 HC of comparable age and sex (mean age 49.6±8.8 years; range 35-69 years; M/F:11/11).

All patients enrolled had to fulfill the following inclusion criteria: age between 18 and 75 years, MS diagnosis according to the revised McDonald criteria (Polman et al., 2011) with a progressive phenotype (Lublin et al., 2014) and an EDSS score ≤ 7.0. In particular, patients were classified as primary progressive (PP) when showing a clinical progression over a period of at least one year without prior exacerbations, while they were classified as secondary progressive (SP) when showing a clinical progression (also confirmed over a period of at least one year) after a conversion from a relapsing remitting (RR) course. According to the same criteria (Lublin et al., 2014), disease activity and progression over the year preceding the study visit was also evaluated. Exclusion criteria of the present study were: presence of other systemic conditions, alcohol or drug addiction, prior history of head trauma, clinical diagnosis of psychiatric disorders, and, for patients, clinical diagnosis of any other neurological disorder other than MS.

Within 1 week from the MRI scan all patients underwent neuropsychological and clinical examination with evaluation of the Expanded Disability Status Scale (EDSS). The Brief International Cognitive Assessment of Multiple Sclerosis (BICAMS) battery, which includes the following tests: Symbol Digit Modalities Test (SDMT), Brief Visuospatial Memory Test - Revised (BVMT) and California Verbal Learning Test-II (CVLT), was also administered. Neuropsychological raw scores were then converted in z-scores according to (Goretti et al., 2014), and used in the following analyses.

MRI data acquisition

All images were acquired on the same 3T MRI scanner (Trio, Siemens Healthineers). The following sequences were acquired: a T2-weighted sequence (40 axial slices, TE=63.0ms, TR=4500ms, voxel size=1.0x1.0x4.0mm^3) used for the quantification of the lesion volumes, a 3D T1-weighted MPRAGE sequence (224 sagittal slices, TE=2.47ms, TR=3000ms, TI=1000ms, voxel size=1.0x1.0x1.0mm^3) used for the volumetric analyses and a T2*-weighted echo-planar imaging sequence (30 axial slices, TE=40ms TR=2500ms, voxel size=3x3x4mm^3, gap 1 mm, 200 time points) for the RS-fMRI analysis.

During the BOLD acquisition subjects were asked to relax with eyes closed, without falling asleep, while laying supine in the MR scan with their head lightly fixed by straps and foam pads to minimize any possible head movement.

MRI data processing

T2-weighted hyperintense lesions were segmented for all MS patients by experienced observers using a semi-automatic segmentation technique (Jim 7, Xinapse Systems Ltd, Northants, UK), and both entire brain (LV) and the cerebellar (CLV) lesion volumes were derived.

Cerebellar volumes were calculated on lesion-filled 3D T1-weighted images using SUIT, as previously described in Chapter 4.2 (page 7).

Preprocessing of RS-fMRI was conducted using the FC toolbox CONN (McGovern Institute for Brain Research, Massachusetts Institute of Technology, Cambridge; http://www.nitrc.org/projects/conn), which contains libraries for fMRI analysis based on SPM. Briefly, the following pre-processing steps were applied: removal of the first five time points, motion correction, slice timing correction, temporal despiking with a hyperbolic tangent squashing function followed by band-pass filtering (for f between 0.008 Hz and 0.09 Hz) and a spatial smoothing using a 6-mm Gaussian kernel. From the motion correction procedure a computation of the mean displacement of the brain voxels was obtained as the RMS of the translations along the three axes (Van Dijk, Sabuncu, & Buckner, 2012), and those studies showing a mean relative RMS of 0.20 mm or higher, or with more than 2.0 mm displacement along or 2.0 degrees rotation around

any axis were discarded from the analysis. In addition, a "scrubbing" procedure was applied to those time points (along with the preceding and the two following ones) showing a framewise differential of signal intensity >9 z-values, to further suppress the effect of patient movements.

Data sets were then normalized to the standard MNI EPI template and resampled to a voxel size of $2\times2\times2mm^3$. To evaluate the overall accuracy of the processing, an experienced operator assessed quality of the images.

For each subject, BOLD signal time course was calculated for lobules VI, Crus I, Crus II and VIIb using the Harvard-Oxford Atlas available in CONN (Desikan et al., 2006), and correlation map of the BOLD signal across the brain was generated, including in a GLM the time courses of WM and CSF signals, and the six parameters (translations and rotations along the X, Y and Z axes) of spatial transformation, as derived from the coregistration step.

Statistical analysis

Student's t-test was used to test group differences in terms of age, while Chi-squared test was used to test possible differences in terms of gender, with a significance level set for $p<0.05$.

Group differences in terms of cerebellar volumes were tested via multivariate GLM, including ICV as a covariate of no interest to account for head size, with a significance level of $p<0.01$, Bonferroni-corrected for multiple comparisons (0.05/5, as the number of tested variables, namely the total cerebellar and lobules VI, Crus I, Crus II and VIIb volumes). Differences in terms of FC maps were also probed voxel-wise over the whole brain using a GLM, including as confounding covariates age, sex and the average motion, in order to remove potential residual movement effects. This second-level analysis was also carried out including cerebellar structural metrics (namely, CLV and cerebellar lobule volumes) as additional confounding variables in the GLM, in order to test the impact of these metrics on cerebellar FC.

For all RS-fMRI analyses, both contrasts (HC > MS and HC < MS) were probed, and differences were considered significant for $p<0.0125$ (0.05/4 as the number of tested seeds), corrected for the family-wise error at the cluster level.

In order to explore all possible relationships between cerebro-cerebellar abnormalities in FC and cognition, when significant differences emerged for the tested seeds after controlling for specific cerebellar atrophy and CLV, the first eigenvariate of each significant cluster was extracted in SPM12, corrected for age, sex, and RMS, and entered in a nonparametric correlation analysis with all available cognitive scores using the Spearman coefficient, with results considered significant for $p<0.05$.

Analyses were carried out using Statistical Package for Social Science (SPSS Inc, v. 20.0, Chicago, Ill).

6.3 Results

The HC and MS groups were no different in terms of age (p=0.68) and sex (p=0.34). Of the 35 enrolled patients, 12 presented a PP course and 23 a SP course, with 10 subjects showing activity and 8 subjects showing disease progression in the year preceding the study visit.

Due to excessive movements during the RS-fMRI acquisition, six MS patients were excluded and a final population of 29 PMS patients was considered in all subsequent analyses. In the remaining 51 RS-fMRI datasets (29 PMS patients and 22 HC), no difference, no difference in terms of RMS was present between MS patients and HC (0.043 ± 0.036 vs 0.057 ± 0.044 in HC and MS respectively, p=0.22).

Compared to HC, MS patients showed a decrease of total cerebellar volume (p=0.001), as well as a decrease of all investigated cerebellar lobules ($p \leq 0.005$).

When testing FC of cerebellar lobules without taking into account cerebellar structural damage, MS patients showed a cluster of reduced FC between Crus II and right frontal pole (p=0.001) and a similar cluster of reduced FC between Lobule VIIb and the right frontal pole (p=0.002). In addition, MS patients showed increased FC between Lobule VIIb and a cluster located at the level of the right precentral gyrus, partly extending to the ipsilateral superior frontal gyrus ($p<0.001$; Figure 27A).

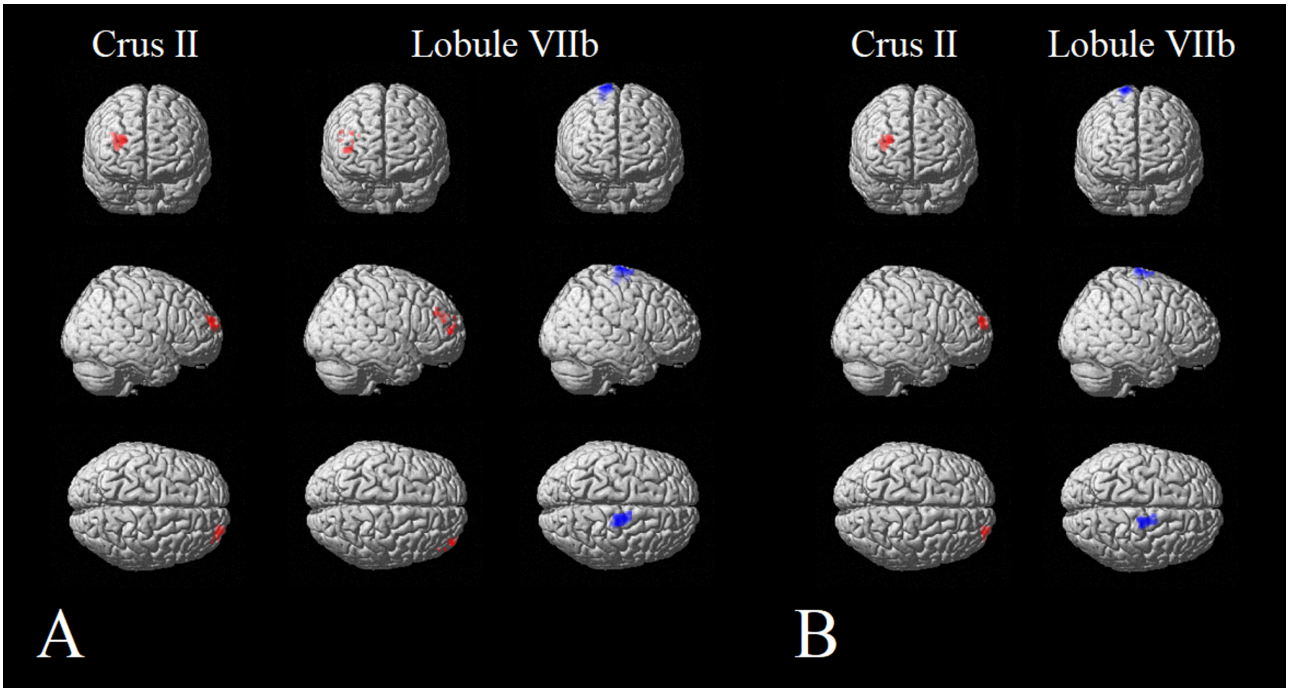

Figure 27: Results of the RS-fMRI analysis without taking into account (a) and after controlling (b) for cerebellar structural damage. Clusters of significant FC decrease in MS patients compared to HCs are shown in red, while clusters of significant FC increase are presented in blue. All results are superimposed on a standard 3D rendering of a brain volume in the Montreal Neurological Institute space (top–bottom: frontal view, lateral right view and upper view).
RS-fMRI resting-state functional MRI, MS multiple sclerosis, HC healthy controls.

When testing cerebellar lobular FC taking into account metrics of cerebellar structural damage, the FC between Crus II and right frontal pole (p=0.005) remained significantly decreased, although to a lesser extent. Similarly, the cluster of increased FC between Lobule VIIb and right precentral gyrus was still significant (p=0.003; Figure 27B). No significant differences emerged for the other tested lobules.

Finally, when testing for possible relationship between clinical scores and clusters of altered FC between cerebellum and cortex, we found an inverse correlation between the cluster of increased FC in MS at the level of the right precentral gyrus and BVMT scores (r=-0.393; p=0.03; Figure 28).

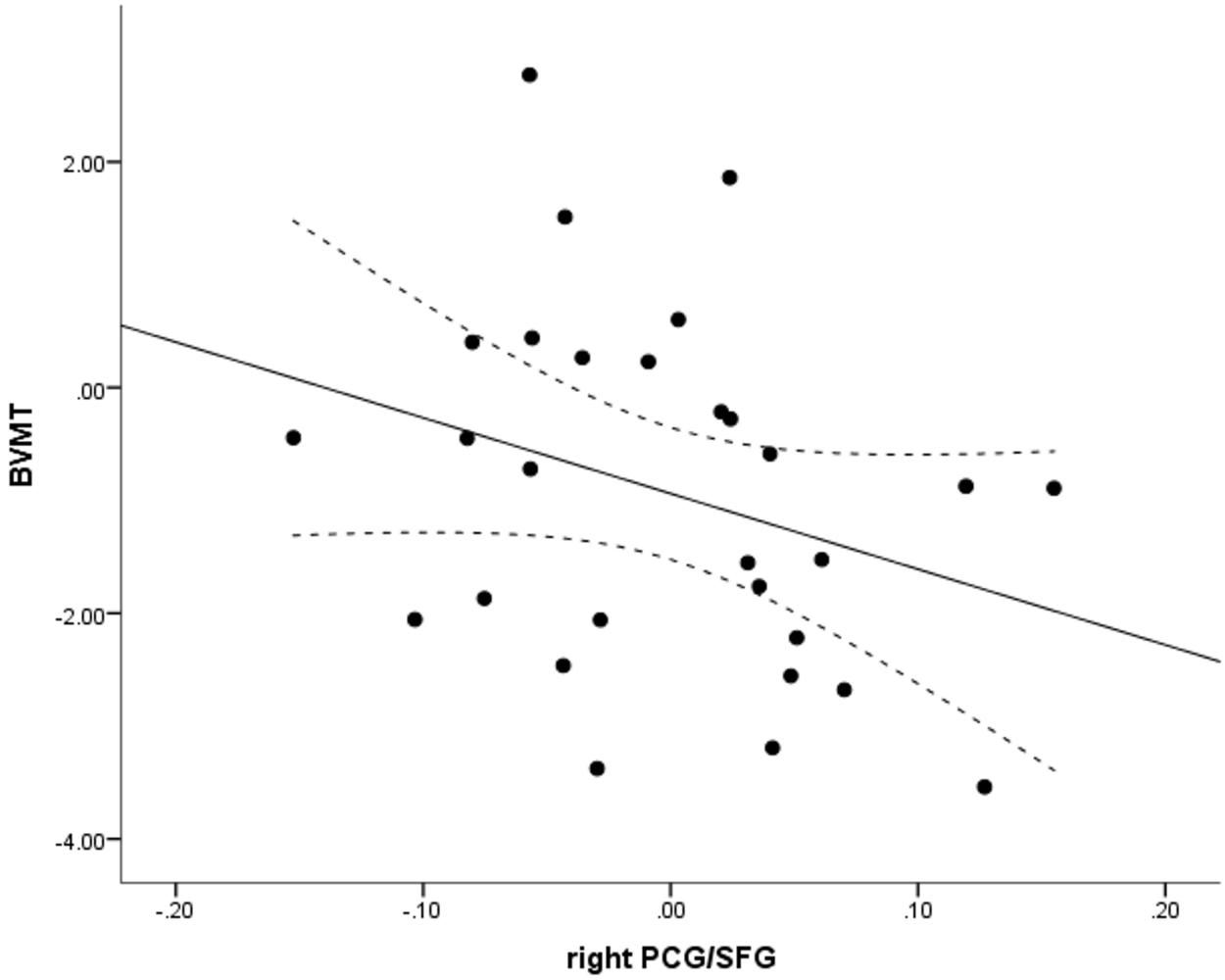

Figure 28: Scatter plot of the correlation between clinical data and the cluster of increased functional connectivity in MS patients compared to HC (r=−0.393; p=0.03) between cerebellar Lobule VIIb and the right PCG (extending to the ipsilateral SFG). Linear fit (middle line) and 95%individual CIs (dashed lines) are shown. BVMT z-scores were calculated according to (Goretti et al., 2014).

MS: multiple sclerosis; HC: healthy controls; PCG: precentral gyrus; SFG: superior frontal gyrus; BVMT: brief visuospatial memory test; CI: confidence interval.

No other significant correlation emerged between the cluster of reduced FC at the level of the right frontal pole and the other clinical variables.

A list of demographic and clinical information of MS patients and HC analyzed in this study is reported in Table 9, while the results of the volumetric analysis are provided in Table 10 and results of the RS-fMRI analysis are showed in Table 10 and Figure 27.

	HC (n=22)	MS (n=29)
Age (mean ± SD)	49.6± 8.8 (range 35-69)	51.2± 11.9 (range 29-72)
Sex (M/F)	11/11	11/18
DD (mean ± SD)	n.a.	16.6± 10.6
EDSS (median)	n.a.	6.0 (range 1.5 - 7.0)
SDMT (mean ± SD)	n.a.	-1.58 ± 1.43
BVMT (mean ± SD)	n.a.	-0.98 ± 1.34
CVLT (mean ± SD)	n.a.	-0.94 ± 1.58

Table 9: Demographics and clinical variables of all subjects included in the MS analysis.

Ages and DD are expressed in years, while cognitive scores are expressed as z-scores obtained according to (Goretti et al., 2014).

MS: multiple sclerosis; SD: standard deviation; DD: disease duration; EDSS: expanded disability status scale; SDMT: symbol digit modalities test; BVMT: brief visuospatial memory test-revised; CVLT: California verbal learning test-II; n.a: not applicable

	HC (n=22)	MS (n=29)	p-values
LV (mean ± SD)	n.a	12.4± 12.6	n.a
CLV (mean ± SD)	n.a	0.1± 0.1	n.a
Total cerebellar volume	137.54 ± 12.14	128.35 ± 13.61	**0.001**
Lobule VI volume	23.76 ± 2.04	21.97 ± 2.42	**<0.001**
Crus I volume	28.03 ± 2.58	26.26 ± 2.88	**0.003**
Crus II volume	19.94 ± 1.99	18.58 ± 2.02	**0.003**
Lobule VIIb volume	10.79 ± 1.16	10.06 ± 1.20	**0.005**

Table 10: MRI metrics for all subjects included in the analysis.

HC: healthy controls; MS: multiple sclerosis; SD: standard deviation; LV: whole brain lesion volume; CLV: cerebellar lesion volume; n.a: not applicable.

Volumes (in milliliters) are expressed as mean ± standard deviation. Significant differences are reported in bold.

				MNI			
			Volume	T	X	Y	Z	
Before controlling for cerebellar structural damage	**HC > MS**							
		Crus II	2.3	5.32	30	62	22	*Right Frontal Pole*
		Lobule VIIb	2.1	4.73	38	58	28	*Right Frontal Pole*
	HC < MS							
		Lobule VIIb	2.9	5.67	14	-16	78	*Right Precentral Gyrus*
After controlling for cerebellar structural damage	**HC > MS**							
		Crus II	1.8	5.49	30	62	24	*Right Frontal Pole*
	HC < MS							
		Lobule VIIb	1.9	5.60	14	-16	78	*Right Precentral Gyrus*

Table 11: Results of the RS-fMRI analysis.

Volumes of the cluster of significant differences between the two groups are reported in ml.

RS-fMRI: resting-state functional MRI; MS: multiple sclerosis; HC: healthy controls; MNI: Montreal Neurological Institute

6.4 Discussion

We explored, for the first time, whole-brain FC of the individual cerebellar lobules involved in cognitive functions in PMS patients, demonstrating a functional rearrangement of the physiological connections between posterior cerebellum, frontal pole and areas involved in the task-positive and salience network (M. D. Fox et al., 2005; O'Reilly, Beckmann, Tomassini, Ramnani, & Johansen-Berg, 2010; Sang et al., 2012). Such reconfiguration of cerebellar FC seems to be somehow independent from cerebellar structural damage, as suggested by the results of our two-step analysis. This finding is not completely surprising, considering that structural damage occurring in different regions of the cerebellum-cortex circuits might play a different role in cerebellar FC rewiring. Specifically, in our population the reduction in FC between lobule VIIb and frontal pole is partially accounted for by cerebellar structural damage, while the decreased FC between Crus II and frontal pole is still evident after correction for cerebellar atrophy and lesion volume. The latter finding might also be related to a lower degree of atrophy affecting Crus II, in line with the results of a recent work that showed a relative lower volume loss in Crus II of PMS patients compared with HCs (Cocozza et al., 2017).

Our results partially confirm and expand recent findings about dentate nucleus connectivity in relapsing-remitting and pediatric MS (Cirillo et al., 2016; Sbardella et al., 2017). In both populations, increased cerebellar FC with cortical fronto-parietal regions characterized MS patients in comparison with controls (Cirillo et al., 2016; Sbardella et al., 2017). Since such FC increase was directly correlated with better clinical performance, it was interpreted as a compensatory adaptation. In our study, the presence of both increased and decreased cerebellar FC in patients compared to HC might reflect the more advanced disease stage of our population, and the consequence of a more diffuse and severe structural damage and/or the exhaustion of reserve capacity.

It has been recently suggested that cerebellar function shows similarities across different processing domains, with function prediction and error-based learning constituting the common mechanisms at

the basis of cerebellar involvement in both motor and cognitive control (Sokolov, Miall, & Ivry, 2017). In this functional frame, the posterior cerebellum participates in complex cognitive processes by means of partially overlapping connection to prefrontal and posterior-parietal cortex (O'Reilly et al., 2010). In particular, lobule VI and VIIb are involved in selection of pertinent stimuli through their interaction with the salience network, while Crus I and Crus II are mostly involved in executive control, verbal working memory and language function, together with lobule VI. Furthermore, Lobule VI is also involved in visuospatial processing, while lobule VIIb additionally participates in attention-demanding tasks and social cognition (Sang et al., 2012; Sokolov et al., 2017). Against this background, the inverse relationship we identified between increased FC in precentral gyrus and BVMT scores could be interpreted as an example of maladaptive functional reorganization, or, alternatively, could represent an attempt to maintain adequate cognitive performances, by increasing the connections between posterior cerebellum and areas involved in stimulus selection and level of attention (Sang et al., 2012). Interestingly, the lack of other correlations between cerebellar FC changes and cognitive scores suggests that cerebellar connectivity impairment, although clinically relevant, it is not the only factor driving the development of cognitive impairment in PMS, but it has to be considered in a wider scenario where reconfiguration of different circuits controlling cognition, along with volume loss, contribute to the clinical expression of cognitive deficits in MS (Cocozza et al., 2017; Loitfelder et al., 2012; Petracca et al., 2017; Rocca et al., 2012).

Although all efforts have been made to account for the impact of atrophy and focal lesions on cerebellar FC, a limitation of the present study is the lack cerebellar damage assessment at microstructural level. A further limitation can be found in the small number of subjects falling into each group when categorizing patients according to the disease course (PP/SP), activity (active/inactive) and progression status (progressive/stable), which prevented us from conducting any subgroup comparison. For these reasons, further explorations are warranted in future studies.

In conclusion, our study shows that FC rearrangements occur in PMS patients, somehow independently from cerebellar macroscopic structural damage, and that they are likely to be an expression of a maladaptive functional rearrangement rather than a compensatory mechanisms. Taken together, these results further expand the current knowledge of cerebellar damage in MS, confirming its role in the complex pathophysiology of cognitive deficits.

CONCLUSIONS AND FUTURE PERSPECTIVES

The cerebellum plays a key role in the control of motor and cognitive functions due to the multiple connections to the forebrain, the thalamus, and the spinal cord. However, the cerebellar complex anatomical structure and its location in the posterior fossa represent a challenge for in vivo structural and cerebellar neuroimaging. While conventional MRI is widely used for brain and cerebellar morphologic evaluation, advanced MRI techniques allow the investigation of cerebellar microstructural and functional characteristics. Volumetric analyses, VBM, diffusion MRI based fiber tractography, resting state and task related functional MRI, perfusion, and proton MR spectroscopy are among the most common techniques applied to the study of cerebellum. The recent advancement in MRI hardware and software and the development of more accurate and robust algorithms for image analysis has improved the structural and functional assessment of the cerebellum. We have learned that, beyond the effect of macroscopically evident atrophy, even the microstructural involvement of the cerebellum can result in clinical disability in a variety of neurological disorders and that cerebellar functional reorganization does not necessarily follow the accrual of macrostructural damage, but can somehow occur independently from it, possibly further reflecting the effect of cerebellar and brain microscopic abnormalities.

In conclusion, thanks to the application of advanced imaging sequences and processing techniques, we are now able to investigate in vivo the physiopathology behind several neurodegenerative and neuroinflammatory diseases and to explore the role of MRI measures of cerebellar structure and function as early and sensitive marker of disease progression and treatment response.

BIBLIOGRAPHY

Aertsen, A. M., Gerstein, G. L., Habib, M. K., & Palm, G. (1989). Dynamics of neuronal firing correlation: modulation of "effective connectivity". *J Neurophysiol, 61*(5), 900-917. doi:10.1152/jn.1989.61.5.900

Albanese, A., Asmus, F., Bhatia, K. P., Elia, A. E., Elibol, B., Filippini, G., . . . Valls-Sole, J. (2011). EFNS guidelines on diagnosis and treatment of primary dystonias. *Eur J Neurol, 18*(1), 5-18. doi:10.1111/j.1468-1331.2010.03042.x

Alberstone, C. D., Steinmetz, M. P., Najm, I. M., & Benzel, E. D. (2009). *Anatomic Basis of Neurologic Diagnosis*: Thieme.

Ashburner, J. (2007). A fast diffeomorphic image registration algorithm. *Neuroimage, 38*(1), 95-113. doi:10.1016/j.neuroimage.2007.07.007

Ashburner, J., & Friston, K. (1997). Multimodal image coregistration and partitioning--a unified framework. *Neuroimage, 6*(3), 209-217. doi:10.1006/nimg.1997.0290

Ashburner, J., & Friston, K. J. (1999). Nonlinear spatial normalization using basis functions. *Hum Brain Mapp, 7*(4), 254-266. doi:10.1002/(SICI)1097-0193(1999)7:4<254::AID-HBM4>3.0.CO;2-G

Ashburner, J., & Friston, K. J. (2000). Voxel-based morphometry--the methods. *Neuroimage, 11*(6 Pt 1), 805-821. doi:10.1006/nimg.2000.0582

Ashburner, J., & Friston, K. J. (2005). Unified segmentation. *Neuroimage, 26*(3), 839-851. doi:10.1016/j.neuroimage.2005.02.018

Bandettini, P. A., Wong, E. C., Hinks, R. S., Tikofsky, R. S., & Hyde, J. S. (1992). Time course EPI of human brain function during task activation. *Magn Reson Med, 25*(2), 390-397. doi:10.1002/mrm.1910250220

Batson, M. A., Petridou, N., Klomp, D. W., Frens, M. A., & Neggers, S. F. (2015). Single session imaging of cerebellum at 7 Tesla: obtaining structure and function of multiple motor subsystems in individual subjects. *PLoS One, 10*(8), e0134933. doi:10.1371/journal.pone.0134933

Battaglini, M., Jenkinson, M., & De Stefano, N. (2012). Evaluating and reducing the impact of white matter lesions on brain volume measurements. *Hum Brain Mapp, 33*(9), 2062-2071. doi:10.1002/hbm.21344

Bereczki, D., Wei, L., Otsuka, T., Acuff, V., Pettigrew, K., Patlak, C., & Fenstermacher, J. (1993). Hypoxia increases velocity of blood flow through parenchymal microvascular systems in rat brain. *J Cereb Blood Flow Metab, 13*(3), 475-486. doi:10.1038/jcbfm.1993.62

Birn, R. M., Smith, M. A., Jones, T. B., & Bandettini, P. A. (2008). The respiration response function: the temporal dynamics of fMRI signal fluctuations related to changes in respiration. *Neuroimage, 40*(2), 644-654. doi:10.1016/j.neuroimage.2007.11.059

Biswal, B. B., Van Kylen, J., & Hyde, J. S. (1997). Simultaneous assessment of flow and BOLD signals in resting-state functional connectivity maps. *NMR Biomed, 10*(4-5), 165-170. doi:10.1002/(sici)1099-1492(199706/08)10:4/5<165::aid-nbm454>3.0.co;2-7

Blood, A. J., Tuch, D. S., Makris, N., Makhlouf, M. L., Sudarsky, L. R., & Sharma, N. (2006). White matter abnormalities in dystonia normalize after botulinum toxin treatment. *Neuroreport, 17*(12), 1251-1255. doi:10.1097/01.wnr.0000230500.03330.01

Bologna, M., & Berardelli, A. (2017). Cerebellum: An explanation for dystonia? *Cerebellum Ataxias, 4*, 6. doi:10.1186/s40673-017-0064-8

Boxerman, J. L., Hamberg, L. M., Rosen, B. R., & Weisskoff, R. M. (1995). MR contrast due to intravascular magnetic susceptibility perturbations. *Magn Reson Med, 34*(4), 555-566. doi:10.1002/mrm.1910340412

Buckner, R. L., Andrews-Hanna, J. R., & Schacter, D. L. (2008). The brain's default network: anatomy, function, and relevance to disease. *Ann N Y Acad Sci, 1124*, 1-38. doi:10.1196/annals.1440.011

Campuzano, V., Montermini, L., Molto, M. D., Pianese, L., Cossee, M., Cavalcanti, F., . . . Pandolfo, M. (1996). Friedreich's ataxia: autosomal recessive disease caused by an intronic GAA triplet repeat expansion. *Science, 271*(5254), 1423-1427.

Carass, A., Cuzzocreo, J. L., Han, S., Hernandez-Castillo, C. R., Rasser, P. E., Ganz, M., . . . Prince, J. L. (2018). Comparing fully automated state-of-the-art cerebellum parcellation from magnetic resonance images. *Neuroimage, 183*, 150-172. doi:10.1016/j.neuroimage.2018.08.003

Carbon, M., Kingsley, P. B., Tang, C., Bressman, S., & Eidelberg, D. (2008). Microstructural white matter changes in primary torsion dystonia. *Mov Disord, 23*(2), 234-239. doi:10.1002/mds.21806

Cardenas, V. A., Price, M., Infante, M. A., Moore, E. M., Mattson, S. N., Riley, E. P., & Fein, G. (2014). Automated cerebellar segmentation: Validation and application to detect smaller volumes in children prenatally exposed to alcohol. *Neuroimage Clin, 4*, 295-301. doi:10.1016/j.nicl.2014.01.002

Chang, C., & Glover, G. H. (2009). Effects of model-based physiological noise correction on default mode network anti-correlations and correlations. *Neuroimage, 47*(4), 1448-1459. doi:10.1016/j.neuroimage.2009.05.012

Chen, S., & Li, X. (2012). Functional magnetic resonance imaging for imaging neural activity in the human brain: the annual progress. *Comput Math Methods Med, 2012*, 613465. doi:10.1155/2012/613465

Chen, Y., Kumfor, F., Landin-Romero, R., Irish, M., Hodges, J. R., & Piguet, O. (2018). Cerebellar atrophy and its contribution to cognition in frontotemporal dementias. *Ann Neurol, 84*(1), 98-109. doi:10.1002/ana.25271

Cho, Z. H. (2010). *7.0 Tesla MRI Brain Atlas*: Springer, New York, NY.

Cierpka, M., Wolf, N. D., Kubera, K. M., Schmitgen, M. M., Vasic, N., Frasch, K., & Wolf, R. C. (2017). Cerebellar Contributions to Persistent Auditory Verbal Hallucinations in Patients with Schizophrenia. *Cerebellum, 16*(5-6), 964-972. doi:10.1007/s12311-017-0874-5

Cirillo, S., Rocca, M. A., Ghezzi, A., Valsasina, P., Moiola, L., Veggiotti, P., . . . Filippi, M. (2016). Abnormal cerebellar functional MRI connectivity in patients with paediatric multiple sclerosis. *Mult Scler, 22*(3), 292-301. doi:1352458515592191 [pii]

10.1177/1352458515592191

Clemm von Hohenberg, C., Schocke, M. F., Wigand, M. C., Nachbauer, W., Guttmann, C. R., Kubicki, M., . . . Egger, K. (2013). Radial diffusivity in the cerebellar peduncles correlates with clinical severity in Friedreich ataxia. *Neurol Sci, 34*(8), 1459-1462. doi:10.1007/s10072-013-1402-0

Cocozza, S., Costabile, T., Tedeschi, E., Abate, F., Russo, C., Liguori, A., . . . Sacca, F. (2018). Cognitive and functional connectivity alterations in Friedreich's ataxia. *Ann Clin Transl Neurol, 5*(6), 677-686. doi:10.1002/acn3.555

ACN3555 [pii]

Cocozza, S., Petracca, M., Mormina, E., Buyukturkoglu, K., Podranski, K., Heinig, M. M., . . . Inglese, M. (2017). Cerebellar lobule atrophy and disability in progressive MS. *J Neurol Neurosurg Psychiatry, 88*(12), 1065-1072. doi:10.1136/jnnp-2017-316448

Cocozza, S., Sacca, F., Cervo, A., Marsili, A., Russo, C. V., Giorgio, S. M., . . . Quarantelli, M. (2015). Modifications of resting state networks in spinocerebellar ataxia type 2. *Mov Disord, 30*(10), 1382-1390. doi:10.1002/mds.26284

Cordes, D., Haughton, V. M., Arfanakis, K., Wendt, G. J., Turski, P. A., Moritz, C. H., . . . Meyerand, M. E. (2000). Mapping functionally related regions of brain with functional connectivity MR imaging. *AJNR Am J Neuroradiol, 21*(9), 1636-1644.

Cox, R. W., & Jesmanowicz, A. (1999). Real-time 3D image registration for functional MRI. *Magn Reson Med, 42*(6), 1014-1018. doi:10.1002/(sici)1522-2594(199912)42:6<1014::aid-mrm4>3.0.co;2-f

Criscuolo, C., Mancini, P., Menchise, V., Sacca, F., De Michele, G., Banfi, S., & Filla, A. (2005). Very late onset in ataxia oculomotor apraxia type I. *Ann Neurol, 57*(5), 777. doi:10.1002/ana.20463

D'Ambrosio, A., Pagani, E., Riccitelli, G. C., Colombo, B., Rodegher, M., Falini, A., . . . Rocca, M. A. (2017). Cerebellar contribution to motor and cognitive performance in multiple sclerosis: An MRI sub-regional volumetric analysis. *Mult Scler, 23*(9), 1194-1203. doi:1352458516674567 [pii]

10.1177/1352458516674567

D'Mello, A. M., Crocetti, D., Mostofsky, S. H., & Stoodley, C. J. (2015). Cerebellar gray matter and lobular volumes correlate with core autism symptoms. *Neuroimage Clin, 7*, 631-639. doi:10.1016/j.nicl.2015.02.007

Damoiseaux, J. S., Rombouts, S. A., Barkhof, F., Scheltens, P., Stam, C. J., Smith, S. M., & Beckmann, C. F. (2006). Consistent resting-state networks across healthy subjects. *Proc Natl Acad Sci U S A, 103*(37), 13848-13853. doi:10.1073/pnas.0601417103

Defazio, G., Abbruzzese, G., Livrea, P., & Berardelli, A. (2004). Epidemiology of primary dystonia. *The Lancet Neurology, 3*(11), 673-678. doi:10.1016/s1474-4422(04)00907-x

Della Nave, R., Ginestroni, A., Diciotti, S., Salvatore, E., Soricelli, A., & Mascalchi, M. (2011). Axial diffusivity is increased in the degenerating superior cerebellar peduncles of Friedreich's ataxia. *Neuroradiology, 53*(5), 367-372. doi:10.1007/s00234-010-0807-1

Della Nave, R., Ginestroni, A., Giannelli, M., Tessa, C., Salvatore, E., Salvi, F., . . . Mascalchi, M. (2008). Brain structural damage in Friedreich's ataxia. *J Neurol Neurosurg Psychiatry, 79*(1), 82-85. doi:jnnp.2007.124297 [pii]

10.1136/jnnp.2007.124297

Della Nave, R., Ginestroni, A., Tessa, C., Salvatore, E., Bartolomei, I., Salvi, F., . . . Mascalchi, M. (2008). Brain white matter tracts degeneration in Friedreich ataxia. An in vivo MRI study using tract-based spatial statistics and voxel-based morphometry. *Neuroimage, 40*(1), 19-25. doi:S1053-8119(07)01075-0 [pii]

10.1016/j.neuroimage.2007.11.050

Deluca, C., Golzar, A., Santandrea, E., Lo Gerfo, E., Estocinova, J., Moretto, G., . . . Chelazzi, L. (2014). The cerebellum and visual perceptual learning: evidence from a motion extrapolation task. *Cortex, 58*, 52-71. doi:S0010-9452(14)00156-7 [pii]

10.1016/j.cortex.2014.04.017

Desikan, R. S., Segonne, F., Fischl, B., Quinn, B. T., Dickerson, B. C., Blacker, D., . . . Killiany, R. J. (2006). An automated labeling system for subdividing the human cerebral cortex on MRI scans into gyral based regions of interest. *Neuroimage, 31*(3), 968-980. doi:S1053-8119(06)00043-7 [pii]

10.1016/j.neuroimage.2006.01.021

Despotović, I., Goossens, B., & Philips, W. (2015). MRI segmentation of the human brain: challenges, methods, and applications. *Comput Math Methods Med, 2015*, 450341. doi:10.1155/2015/450341

Deverett, B., Koay, S. A., Oostland, M., & Wang, S. S. (2018). Cerebellar involvement in an evidence-accumulation decision-making task. *Elife, 7*. doi:10.7554/eLife.36781

36781 [pii]

Dice, L. R. (1945). Measures of the Amount of Ecologic Association Between Species. *Ecology, 26*, 297-302.

Diedrichsen, J. (2006). A spatially unbiased atlas template of the human cerebellum. *Neuroimage, 33*(1), 127-138. doi:10.1016/j.neuroimage.2006.05.056

Dogonowski, A. M., Andersen, K. W., Madsen, K. H., Sorensen, P. S., Paulson, O. B., Blinkenberg, M., & Siebner, H. R. (2014). Multiple sclerosis impairs regional functional connectivity in the cerebellum. *Neuroimage Clin, 4*, 130-138. doi:10.1016/j.nicl.2013.11.005

S2213-1582(13)00153-8 [pii]

Draganski, B., Thun-Hohenstein, C., Bogdahn, U., Winkler, J., & May, A. (2003). "Motor circuit" gray matter changes in idiopathic cervical dystonia. *Neurology, 61*(9), 1228-1231. doi:10.1212/01.wnl.0000094240.93745.83

Egger, K., Mueller, J., Schocke, M., Brenneis, C., Rinnerthaler, M., Seppi, K., . . . Poewe, W. (2007). Voxel based morphometry reveals specific gray matter changes in primary dystonia. *Mov Disord, 22*(11), 1538-1542. doi:10.1002/mds.21619

Esposito, M., Dubbioso, R., Peluso, S., Picone, A., Corrado, B., Servodio Iammarone, C., . . . Fasano, A. (2017). Cervical dystonia patients display subclinical gait changes. *Parkinsonism Relat Disord, 43*, 97-100. doi:10.1016/j.parkreldis.2017.07.005

Evans, A. C., Marrett, S., Neelin, P., Collins, L., Worsley, K., Dai, W., . . . Bub, D. (1992). Anatomical mapping of functional activation in stereotactic coordinate space. *Neuroimage, 1*(1), 43-53. doi:10.1016/1053-8119(92)90006-9

Felten, D., O'Banion, M., & Maida, M. *Netter's Atlas of Neuroscience* (3rd ed.): Elsevier.

Fox, M. D., & Raichle, M. E. (2007). Spontaneous fluctuations in brain activity observed with functional magnetic resonance imaging. *Nat Rev Neurosci, 8*(9), 700-711. doi:10.1038/nrn2201

Fox, M. D., Snyder, A. Z., Vincent, J. L., Corbetta, M., Van Essen, D. C., & Raichle, M. E. (2005). The human brain is intrinsically organized into dynamic, anticorrelated functional networks. *Proc Natl Acad Sci U S A, 102*(27), 9673-9678. doi:0504136102 [pii]

10.1073/pnas.0504136102

Fox, P. T., & Raichle, M. E. (1986). Focal physiological uncoupling of cerebral blood flow and oxidative metabolism during somatosensory stimulation in human subjects. *Proc Natl Acad Sci U S A, 83*(4), 1140-1144. doi:10.1073/pnas.83.4.1140

Friston, K. J., Holmes, A. P., Poline, J. B., Grasby, P. J., Williams, S. C., Frackowiak, R. S., & Turner, R. (1995). Analysis of fMRI time-series revisited. *Neuroimage, 2*(1), 45-53. doi:10.1006/nimg.1995.1007

Ganzetti, M., Wenderoth, N., & Mantini, D. (2016). Quantitative Evaluation of Intensity Inhomogeneity Correction Methods for Structural MR Brain Images. *Neuroinformatics, 14*(1), 5-21. doi:10.1007/s12021-015-9277-2

Gatlin, J. L., Wineman, R., Schlakman, B., Buciuc, R., & Khan, M. (2011). Hypertrophic olivary degeneration after resection of a pontine cavernous malformation: a case report. *J Radiol Case Rep, 5*(3), 24-29. doi:10.3941/jrcr.v5i3.603

Glasser, M. F., Sotiropoulos, S. N., Wilson, J. A., Coalson, T. S., Fischl, B., Andersson, J. L., . . . Jenkinson, M. (2013). The minimal preprocessing pipelines for the Human Connectome Project. *Neuroimage, 80*, 105-124. doi:10.1016/j.neuroimage.2013.04.127

Glover, G. H. (2011). Overview of functional magnetic resonance imaging. *Neurosurg Clin N Am, 22*(2), 133-139, vii. doi:10.1016/j.nec.2010.11.001

Gold, J. I., & Shadlen, M. N. (2007). The neural basis of decision making. *Annu Rev Neurosci, 30*, 535-574. doi:10.1146/annurev.neuro.29.051605.113038

Goretti, B., Niccolai, C., Hakiki, B., Sturchio, A., Falautano, M., Minacapelli, E., . . . Amato, M. P. (2014). The Brief International Cognitive Assessment for Multiple Sclerosis (BICAMS): normative values with gender, age and education corrections in the Italian population. *BMC Neurol, 14*, 171. doi:s12883-014-0171-6 [pii]

10.1186/s12883-014-0171-6

Greicius, M. D., Supekar, K., Menon, V., & Dougherty, R. F. (2009). Resting-state functional connectivity reflects structural connectivity in the default mode network. *Cereb Cortex, 19*(1), 72-78. doi:10.1093/cercor/bhn059

Grothe, M., Lotze, M., Langner, S., & Dressel, A. (2017). Impairments in Walking Ability, Dexterity, and Cognitive Function in Multiple Sclerosis Are Associated with Different Regional Cerebellar Gray Matter Loss. *Cerebellum, 16*(5-6), 945-950. doi:10.1007/s12311-017-0871-8

10.1007/s12311-017-0871-8 [pii]

Guell, X., Schmahmann, J. D., Gabrieli, J., & Ghosh, S. S. (2018). Functional gradients of the cerebellum. *Elife, 7*. doi:10.7554/eLife.36652

36652 [pii]

Habas, C., Kamdar, N., Nguyen, D., Prater, K., Beckmann, C. F., Menon, V., & Greicius, M. D. (2009). Distinct cerebellar contributions to intrinsic connectivity networks. *J Neurosci, 29*(26), 8586-8594. doi:29/26/8586 [pii]

10.1523/JNEUROSCI.1868-09.2009

Handel, B., Thier, P., & Haarmeier, T. (2009). Visual motion perception deficits due to cerebellar lesions are paralleled by specific changes in cerebro-cortical activity. *J Neurosci, 29*(48), 15126-15133. doi:29/48/15126 [pii]

10.1523/JNEUROSCI.3972-09.2009

Haralick, R. M., Shanmugam, K., & Dinstein, I. (1973). Textural Features for Image Classification. *IEEE Transactions on Systems, Man, and Cybernetics, SMC-3*(6), 610-621. doi:10.1109/TSMC.1973.4309314

Harding, I. H., Corben, L. A., Storey, E., Egan, G. F., Stagnitti, M. R., Poudel, G. R., . . . Georgiou-Karistianis, N. (2016). Fronto-cerebellar dysfunction and dysconnectivity underlying cognition in friedreich ataxia: The IMAGE-FRDA study. *Hum Brain Mapp, 37*(1), 338-350. doi:10.1002/hbm.23034

Harding, I. H., Raniga, P., Delatycki, M. B., Stagnitti, M. R., Corben, L. A., Storey, E., . . . Egan, G. F. (2016). Tissue atrophy and elevated iron concentration in the extrapyramidal motor system in Friedreich ataxia: the IMAGE-FRDA study. *J Neurol Neurosurg Psychiatry, 87*(11), 1261-1263. doi:jnnp-2015-312665 [pii]

10.1136/jnnp-2015-312665

Hernandez-Castillo, C. R., Diaz, R., Campos-Romo, A., & Fernandez-Ruiz, J. (2017). Neural correlates of ataxia severity in spinocerebellar ataxia type 3/Machado-Joseph disease. *Cerebellum Ataxias, 4*, 7. doi:10.1186/s40673-017-0065-7

65 [pii]

Hernandez-Castillo, C. R., King, M., Diedrichsen, J., & Fernandez-Ruiz, J. (2018). Unique degeneration signatures in the cerebellar cortex for spinocerebellar ataxias 2, 3, and 7. *Neuroimage Clin, 20*, 931-938. doi:S2213-1582(18)30301-2 [pii]

10.1016/j.nicl.2018.09.026

Hoche, F., Frankenberg, E., Rambow, J., Theis, M., Harding, J. A., Qirshi, M., . . . Kieslich, M. (2014). Cognitive phenotype in ataxia-telangiectasia. *Pediatr Neurol, 51*(3), 297-310. doi:S0887-8994(14)00269-0 [pii]

10.1016/j.pediatrneurol.2014.04.027

Huh, Y. E., & Kim, J. S. (2011). Patterns of spontaneous and head-shaking nystagmus in cerebellar infarction: imaging correlations. *Brain, 134*(Pt 12), 3662-3671. doi:awr269 [pii]

10.1093/brain/awr269

Hvizdosova, L., Nevrly, M., Otruba, P., Hlustik, P., Kanovsky, P., & Zapletalova, J. (2020). The Prevalence of Dystonic Tremor and Tremor Associated with Dystonia in Patients with Cervical Dystonia. *Sci Rep, 10*(1), 1436. doi:10.1038/s41598-020-58363-2

Iglesias, J. E., Van Leemput, K., Bhatt, P., Casillas, C., Dutt, S., Schuff, N., . . . Fischl, B. (2015). Bayesian segmentation of brainstem structures in MRI. *Neuroimage, 113*, 184-195. doi:10.1016/j.neuroimage.2015.02.065

Inglese, M., Petracca, M., Mormina, E., Achiron, A., Straus-Farber, R., Miron, S., . . . Sormani, M. P. (2017). Cerebellar volume as imaging outcome in progressive multiple sclerosis. *PLoS One, 12*(4), e0176519. doi:10.1371/journal.pone.0176519

PONE-D-17-06604 [pii]

Jacobi, H., Reetz, K., du Montcel, S. T., Bauer, P., Mariotti, C., Nanetti, L., . . . Klockgether, T. (2013). Biological and clinical characteristics of individuals at risk for spinocerebellar ataxia types 1, 2, 3, and 6 in the longitudinal RISCA study: analysis of baseline data. *Lancet Neurol, 12*(7), 650-658. doi:S1474-4422(13)70104-2 [pii]

10.1016/S1474-4422(13)70104-2

Jenkinson, M., Beckmann, C. F., Behrens, T. E., Woolrich, M. W., & Smith, S. M. (2012). FSL. *Neuroimage, 62*(2), 782-790. doi:10.1016/j.neuroimage.2011.09.015

Jerde, T. A., Merriam, E. P., Riggall, A. C., Hedges, J. H., & Curtis, C. E. (2012). Prioritized maps of space in human frontoparietal cortex. *J Neurosci, 32*(48), 17382-17390. doi:32/48/17382 [pii]

10.1523/JNEUROSCI.3810-12.2012

Jokisch, D., Troje, N. F., Koch, B., Schwarz, M., & Daum, I. (2005). Differential involvement of the cerebellum in biological and coherent motion perception. *Eur J Neurosci, 21*(12), 3439-3446. doi:EJN4145 [pii]

10.1111/j.1460-9568.2005.04145.x

Jovicich, J., Czanner, S., Greve, D., Haley, E., van der Kouwe, A., Gollub, R., . . . Dale, A. (2006). Reliability in multi-site structural MRI studies: effects of gradient non-linearity correction on phantom and human data. *Neuroimage, 30*(2), 436-443. doi:10.1016/j.neuroimage.2005.09.046

Jung, B. C., Choi, S. I., Du, A. X., Cuzzocreo, J. L., Ying, H. S., Landman, B. A., . . . Ying, S. H. (2012). MRI shows a region-specific pattern of atrophy in spinocerebellar ataxia type 2. *Cerebellum, 11*(1), 272-279. doi:10.1007/s12311-011-0308-8

Kaji, R., Bhatia, K., & Graybiel, A. M. (2018). Pathogenesis of dystonia: is it of cerebellar or basal ganglia origin? *J Neurol Neurosurg Psychiatry, 89*(5), 488-492. doi:10.1136/jnnp-2017-316250

Kandel, E. R., Schwartz, J. H., Jessell, T. M., Siegelbaum, S. A., & Hudspeth, A. J. (2012). *Principles of Neural Science* (N. Y. McGraw-Hill Ed. 5th ed.).

Kansal, K., Yang, Z., Fishman, A. M., Sair, H. I., Ying, S. H., Jedynak, B. M., . . . Onyike, C. U. (2017). Structural cerebellar correlates of cognitive and motor dysfunctions in cerebellar degeneration. *Brain, 140*(3), 707-720. doi:aww327 [pii]

10.1093/brain/aww327

Kato, T., Kamei, A., Takashima, S., & Ozaki, T. (1993). Human visual cortical function during photic stimulation monitoring by means of near-infrared spectroscopy. *J Cereb Blood Flow Metab, 13*(3), 516-520. doi:10.1038/jcbfm.1993.66

Kelly, R. M., & Strick, P. L. (2003). Cerebellar loops with motor cortex and prefrontal cortex of a nonhuman primate. *J Neurosci, 23*(23), 8432-8444. doi:23/23/8432 [pii]

Kennan, R. P., Zhong, J., & Gore, J. C. (1994). Intravascular susceptibility contrast mechanisms in tissues. *Magn Reson Med, 31*(1), 9-21. doi:10.1002/mrm.1910310103

Koeppen, A. H., & Mazurkiewicz, J. E. (2013). Friedreich ataxia: neuropathology revised. *J Neuropathol Exp Neurol, 72*(2), 78-90. doi:10.1097/NEN.0b013e31827e5762

00005072-201302000-00002 [pii]

Koziol, L. F., Budding, D., Andreasen, N., D'Arrigo, S., Bulgheroni, S., Imamizu, H., . . . Yamazaki, T. (2014). Consensus paper: the cerebellum's role in movement and cognition. *Cerebellum, 13*(1), 151-177. doi:10.1007/s12311-013-0511-x

Kuyper, D. J., Parra, V., Aerts, S., Okun, M. S., & Kluger, B. M. (2011). Nonmotor manifestations of dystonia: a systematic review. *Mov Disord, 26*(7), 1206-1217. doi:10.1002/mds.23709

Kwong, K. K., Belliveau, J. W., Chesler, D. A., Goldberg, I. E., Weisskoff, R. M., Poncelet, B. P., . . . et al. (1992). Dynamic magnetic resonance imaging of human brain activity during

primary sensory stimulation. *Proc Natl Acad Sci U S A, 89*(12), 5675-5679. doi:10.1073/pnas.89.12.5675

Lee, S. H., Park, S. H., Kim, J. S., Kim, H. J., Yunusov, F., & Zee, D. S. (2014). Isolated unilateral infarction of the cerebellar tonsil: ocular motor findings. *Ann Neurol, 75*(3), 429-434.

Lehericy, S., Tijssen, M. A., Vidailhet, M., Kaji, R., & Meunier, S. (2013). The anatomical basis of dystonia: current view using neuroimaging. *Mov Disord, 28*(7), 944-957. doi:10.1002/mds.25527

Lindig, T., Bender, B., Kumar, V. J., Hauser, T. K., Grodd, W., Brendel, B., . . . Schols, L. (2019). Pattern of Cerebellar Atrophy in Friedreich's Ataxia-Using the SUIT Template. *Cerebellum, 18*(3), 435-447. doi:10.1007/s12311-019-1008-z

10.1007/s12311-019-1008-z [pii]

Liu, J., Wang, Q., Liu, F., Song, H., Liang, X., Lin, Z., . . . Chen, L. D. (2017). Altered functional connectivity in patients with post-stroke memory impairment: A resting fMRI study. *Exp Ther Med, 14*(3), 1919-1928. doi:10.3892/etm.2017.4751

ETM-0-0-4751 [pii]

Loitfelder, M., Filippi, M., Rocca, M., Valsasina, P., Ropele, S., Jehna, M., . . . Enzinger, C. (2012). Abnormalities of resting state functional connectivity are related to sustained attention deficits in MS. *PLoS One, 7*(8), e42862. doi:10.1371/journal.pone.0042862

PONE-D-12-07219 [pii]

Lowe, M. J., Dzemidzic, M., Lurito, J. T., Mathews, V. P., & Phillips, M. D. (2000). Correlations in low-frequency BOLD fluctuations reflect cortico-cortical connections. *Neuroimage, 12*(5), 582-587. doi:10.1006/nimg.2000.0654

Lublin, F. D., Reingold, S. C., Cohen, J. A., Cutter, G. R., Sorensen, P. S., Thompson, A. J., . . . Polman, C. H. (2014). Defining the clinical course of multiple sclerosis: the 2013 revisions. *Neurology, 83*(3), 278-286. doi:WNL.0000000000000560 [pii]

10.1212/WNL.0000000000000560

Lupo, M., Olivito, G., Siciliano, L., Masciullo, M., Bozzali, M., Molinari, M., & Leggio, M. (2018). Development of a Psychiatric Disorder Linked to Cerebellar Lesions. *Cerebellum, 17*(4), 438-446. doi:10.1007/s12311-018-0926-5

10.1007/s12311-018-0926-5 [pii]

Lüsebrink, F., Wollrab, A., & Speck, O. (2013). Cortical thickness determination of the human brain using high resolution 3T and 7T MRI data. *Neuroimage, 70*, 122-131. doi:10.1016/j.neuroimage.2012.12.016

Malonek, D., & Grinvald, A. (1996). Interactions between electrical activity and cortical microcirculation revealed by imaging spectroscopy: implications for functional brain mapping. *Science, 272*(5261), 551-554. doi:10.1126/science.272.5261.551

Manjón, J. V., Coupé, P., Martí-Bonmatí, L., Collins, D. L., & Robles, M. (2010). Adaptive non-local means denoising of MR images with spatially varying noise levels. *J Magn Reson Imaging, 31*(1), 192-203. doi:10.1002/jmri.22003

Manni, E., & Petrosini, L. (2004). A century of cerebellar somatotopy: a debated representation. *Nat Rev Neurosci, 5*(3), 241-249. doi:10.1038/nrn1347

Mascalchi, M. (2013). The cerebellum looks normal in Friedreich ataxia. *AJNR Am J Neuroradiol, 34*(2), E22. doi:ajnr.A3480 [pii]

10.3174/ajnr.A3480

Matsunari, I., Samuraki, M., Chen, W. P., Yanase, D., Takeda, N., Ono, K., . . . Kinuya, S. (2007). Comparison of 18F-FDG PET and optimized voxel-based morphometry for detection of Alzheimer's disease: aging effect on diagnostic performance. *J Nucl Med, 48*(12), 1961-1970. doi:10.2967/jnumed.107.042820

McRobbie, D. W., Moore, E. A., Graves, M. J., & Prince, M. R. (2017). *MRI from Picture to Proton* (3 ed.). Cambridge: Cambridge University Press.

Meek, J. H., Elwell, C. E., Khan, M. J., Romaya, J., Wyatt, J. S., Delpy, D. T., & Zeki, S. (1995). Regional changes in cerebral haemodynamics as a result of a visual stimulus measured by near infrared spectroscopy. *Proc Biol Sci, 261*(1362), 351-356. doi:10.1098/rspb.1995.0158

Mormina, E., Petracca, M., Bommarito, G., Piaggio, N., Cocozza, S., & Inglese, M. (2017). Cerebellum and neurodegenerative diseases: Beyond conventional magnetic resonance imaging. *World journal of radiology, 9*(10), 371-388. doi:10.4329/wjr.v9.i10.371

Moroso, A., Ruet, A., Lamargue-Hamel, D., Munsch, F., Deloire, M., Coupe, P., . . . Brochet, B. (2017). Microstructural analyses of the posterior cerebellar lobules in relapsing-onset multiple sclerosis and their implication in cognitive impairment. *PLoS One, 12*(8), e0182479. doi:10.1371/journal.pone.0182479

PONE-D-16-36159 [pii]

Moroso, A., Ruet, A., Lamargue-Hamel, D., Munsch, F., Deloire, M., Coupe, P., . . . Brochet, B. (2017). Posterior lobules of the cerebellum and information processing speed at various stages of multiple sclerosis. *J Neurol Neurosurg Psychiatry, 88*(2), 146-151. doi:jnnp-2016-313867 [pii]

10.1136/jnnp-2016-313867

Mosconi, M. W., Wang, Z., Schmitt, L. M., Tsai, P., & Sweeney, J. A. (2015). The role of cerebellar circuitry alterations in the pathophysiology of autism spectrum disorders. *Front Neurosci, 9*, 296. doi:10.3389/fnins.2015.00296

Mottolese, C., Richard, N., Harquel, S., Szathmari, A., Sirigu, A., & Desmurget, M. (2013). Mapping motor representations in the human cerebellum. *Brain, 136*(Pt 1), 330-342. doi:10.1093/brain/aws186

Nachbauer, W., Bodner, T., Boesch, S., Karner, E., Eigentler, A., Neier, L., . . . Delazer, M. (2014). Friedreich ataxia: executive control is related to disease onset and GAA repeat length. *Cerebellum, 13*(1), 9-16. doi:10.1007/s12311-013-0513-8

Nieto, A., Correia, R., de Nobrega, E., Monton, F., Hess, S., & Barroso, J. (2012). Cognition in Friedreich ataxia. *Cerebellum, 11*(4), 834-844. doi:10.1007/s12311-012-0363-9

Noroozian, M. (2014). The role of the cerebellum in cognition: beyond coordination in the central nervous system. *Neurol Clin, 32*(4), 1081-1104. doi:S0733-8619(14)00059-0 [pii]

10.1016/j.ncl.2014.07.005

Novellino, F., Nicoletti, G., Cherubini, A., Caligiuri, M. E., Nistico, R., Salsone, M., . . . Quattrone, A. (2016). Cerebellar involvement in essential tremor with and without resting tremor: A Diffusion Tensor Imaging study. *Parkinsonism Relat Disord, 27*, 61-66. doi:10.1016/j.parkreldis.2016.03.022

O'Callaghan, C., Hornberger, M., Balsters, J. H., Halliday, G. M., Lewis, S. J., & Shine, J. M. (2016). Cerebellar atrophy in Parkinson's disease and its implication for network connectivity. *Brain, 139*(Pt 3), 845-855. doi:10.1093/brain/awv399

O'Reilly, J. X., Beckmann, C. F., Tomassini, V., Ramnani, N., & Johansen-Berg, H. (2010). Distinct and overlapping functional zones in the cerebellum defined by resting state functional connectivity. *Cereb Cortex, 20*(4), 953-965. doi:bhp157 [pii]

10.1093/cercor/bhp157

Obermann, M., Yaldizli, O., De Greiff, A., Lachenmayer, M. L., Buhl, A. R., Tumczak, F., . . . Maschke, M. (2007). Morphometric changes of sensorimotor structures in focal dystonia. *Mov Disord, 22*(8), 1117-1123. doi:10.1002/mds.21495

Ogawa, S., Lee, T. M., Kay, A. R., & Tank, D. W. (1990). Brain magnetic resonance imaging with contrast dependent on blood oxygenation. *Proc Natl Acad Sci U S A, 87*(24), 9868-9872. doi:10.1073/pnas.87.24.9868

Ogawa, S., Tank, D. W., Menon, R., Ellermann, J. M., Kim, S. G., Merkle, H., & Ugurbil, K. (1992). Intrinsic signal changes accompanying sensory stimulation: functional brain mapping with magnetic resonance imaging. *Proc Natl Acad Sci U S A, 89*(13), 5951-5955. doi:10.1073/pnas.89.13.5951

Olivito, G., Lupo, M., Iacobacci, C., Clausi, S., Romano, S., Masciullo, M., . . . Leggio, M. (2018). Structural cerebellar correlates of cognitive functions in spinocerebellar ataxia type 2. *J Neurol, 265*(3), 597-606. doi:10.1007/s00415-018-8738-6

10.1007/s00415-018-8738-6 [pii]

Ormerod, I. E., Harding, A. E., Miller, D. H., Johnson, G., MacManus, D., du Boulay, E. P., . . . McDonald, W. I. (1994). Magnetic resonance imaging in degenerative ataxic disorders. *J Neurol Neurosurg Psychiatry, 57*(1), 51-57. doi:10.1136/jnnp.57.1.51

Pandolfo, M. (2009). Friedreich ataxia: the clinical picture. *J Neurol, 256 Suppl 1*, 3-8. doi:10.1007/s00415-009-1002-3

Pane, C., Costabile, T., Salvati, A., Aurisicchio, D. L., Abate, F., Liguori, A., . . . Sacca, F. (2018). Adult normative values for the PATA Rate Test. *J Neurol, 265*(5), 1102-1105. doi:10.1007/s00415-018-8820-0

10.1007/s00415-018-8820-0 [pii]

Pantano, P., Totaro, P., Fabbrini, G., Raz, E., Contessa, G. M., Tona, F., . . . Berardelli, A. (2011). A transverse and longitudinal MR imaging voxel-based morphometry study in patients with primary cervical dystonia. *AJNR Am J Neuroradiol, 32*(1), 81-84. doi:10.3174/ajnr.A2242

Park, M. T., Pipitone, J., Baer, L. H., Winterburn, J. L., Shah, Y., Chavez, S., . . . Chakravarty, M. M. (2014). Derivation of high-resolution MRI atlases of the human cerebellum at 3T and segmentation using multiple automatically generated templates. *Neuroimage, 95*, 217-231. doi:10.1016/j.neuroimage.2014.03.037

Pauling, L., & Coryell, C. D. (1936). The Magnetic Properties and Structure of Hemoglobin, Oxyhemoglobin and Carbonmonoxyhemoglobin. *Proc Natl Acad Sci U S A, 22*(4), 210-216. doi:10.1073/pnas.22.4.210

Petracca, M., Saiote, C., Bender, H. A., Arias, F., Farrell, C., Magioncalda, P., . . . Inglese, M. (2017). Synchronization and variability imbalance underlie cognitive impairment in primary-progressive multiple sclerosis. *Sci Rep, 7*, 46411. doi:srep46411 [pii]

10.1038/srep46411

Pham, D. L., Xu, C., & Prince, J. L. (2000). Current methods in medical image segmentation. *Annu Rev Biomed Eng, 2*, 315-337. doi:10.1146/annurev.bioeng.2.1.315

Phelps, M. E., Huang, S. C., Hoffman, E. J., Selin, C., Sokoloff, L., & Kuhl, D. E. (1979). Tomographic measurement of local cerebral glucose metabolic rate in humans with (F-18)2-fluoro-2-deoxy-D-glucose: validation of method. *Ann Neurol, 6*(5), 371-388. doi:10.1002/ana.410060502

Piccinin, C. C., Piovesana, L. G., Santos, M. C., Guimaraes, R. P., De Campos, B. M., Rezende, T. J., . . . D'Abreu, A. (2014). Diffuse decreased gray matter in patients with idiopathic craniocervical dystonia: a voxel-based morphometry study. *Front Neurol, 5*, 283. doi:10.3389/fneur.2014.00283

Piccinin, C. C., Santos, M. C., Piovesana, L. G., Campos, L. S., Guimaraes, R. P., Campos, B. M., . . . D'Abreu, A. (2014). Infratentorial gray matter atrophy and excess in primary craniocervical dystonia. *Parkinsonism Relat Disord, 20*(2), 198-203. doi:10.1016/j.parkreldis.2013.10.026

Pohl, K. M., Fisher, J., Grimson, W. E., Kikinis, R., & Wells, W. M. (2006). A Bayesian model for joint segmentation and registration. *Neuroimage, 31*(1), 228-239. doi:10.1016/j.neuroimage.2005.11.044

Polman, C. H., Reingold, S. C., Banwell, B., Clanet, M., Cohen, J. A., Filippi, M., . . . Wolinsky, J. S. (2011). Diagnostic criteria for multiple sclerosis: 2010 revisions to the McDonald criteria. *Ann Neurol, 69*(2), 292-302. doi:10.1002/ana.22366

Prell, T., Peschel, T., Kohler, B., Bokemeyer, M. H., Dengler, R., Gunther, A., & Grosskreutz, J. (2013). Structural brain abnormalities in cervical dystonia. *BMC Neurosci, 14*, 123. doi:10.1186/1471-2202-14-123

Ramdhani, R. A., Kumar, V., Velickovic, M., Frucht, S. J., Tagliati, M., & Simonyan, K. (2014). What's special about task in dystonia? A voxel-based morphometry and diffusion weighted imaging study. *Mov Disord, 29*(9), 1141-1150. doi:10.1002/mds.25934

Reetz, K., Dogan, I., Rolfs, A., Binkofski, F., Schulz, J. B., Laird, A. R., . . . Eickhoff, S. B. (2012). Investigating function and connectivity of morphometric findings--exemplified on cerebellar atrophy in spinocerebellar ataxia 17 (SCA17). *Neuroimage, 62*(3), 1354-1366. doi:S1053-8119(12)00546-0 [pii]

10.1016/j.neuroimage.2012.05.058

Rezende, T. J., Silva, C. B., Yassuda, C. L., Campos, B. M., D'Abreu, A., Cendes, F., . . . Franca, M. C., Jr. (2016). Longitudinal magnetic resonance imaging study shows progressive pyramidal and callosal damage in Friedreich's ataxia. *Mov Disord, 31*(1), 70-78. doi:10.1002/mds.26436

Rocca, M. A., Bonnet, M. C., Meani, A., Valsasina, P., Colombo, B., Comi, G., & Filippi, M. (2012). Differential cerebellar functional interactions during an interference task across multiple sclerosis phenotypes. *Radiology, 265*(3), 864-873. doi:radiol.12120216 [pii]

10.1148/radiol.12120216

Rocca, M. A., Valsasina, P., Leavitt, V. M., Rodegher, M., Radaelli, M., Riccitelli, G. C., . . . Filippi, M. (2017). Functional network connectivity abnormalities in multiple sclerosis: Correlations with disability and cognitive impairment. *Mult Scler*, 1352458517699875. doi:10.1177/1352458517699875

Romero, J. E., Coupé, P., Giraud, R., Ta, V. T., Fonov, V., Park, M. T. M., . . . Manjón, J. V. (2017). CERES: A new cerebellum lobule segmentation method. *Neuroimage, 147*, 916-924. doi:10.1016/j.neuroimage.2016.11.003

Rub, U., Brunt, E. R., Seidel, K., Gierga, K., Mooy, C. M., Kettner, M., . . . Deller, T. (2008). Spinocerebellar ataxia type 7 (SCA7): widespread brain damage in an adult-onset patient

with progressive visual impairments in comparison with an adult-onset patient without visual impairments. *Neuropathol Appl Neurobiol, 34*(2), 155-168. doi:NAN882 [pii]

10.1111/j.1365-2990.2007.00882.x

Sacca, F., Costabile, T., Abate, F., Liguori, A., Paciello, F., Pane, C., . . . Filla, A. (2018). Normalization of timed neuropsychological tests with the PATA rate and nine-hole pegboard tests. *J Neuropsychol, 12*(3), 471-483. doi:10.1111/jnp.12125

Salmi, J., Pallesen, K. J., Neuvonen, T., Brattico, E., Korvenoja, A., Salonen, O., & Carlson, S. (2010). Cognitive and motor loops of the human cerebro-cerebellar system. *J Cogn Neurosci, 22*(11), 2663-2676. doi:10.1162/jocn.2009.21382

Sämann, P. G., Wehrle, R., Hoehn, D., Spoormaker, V. I., Peters, H., Tully, C., . . . Czisch, M. (2011). Development of the brain's default mode network from wakefulness to slow wave sleep. *Cereb Cortex, 21*(9), 2082-2093. doi:10.1093/cercor/bhq295

Sang, L., Qin, W., Liu, Y., Han, W., Zhang, Y., Jiang, T., & Yu, C. (2012). Resting-state functional connectivity of the vermal and hemispheric subregions of the cerebellum with both the cerebral cortical networks and subcortical structures. *Neuroimage, 61*(4), 1213-1225. doi:S1053-8119(12)00392-8 [pii]

10.1016/j.neuroimage.2012.04.011

Sbardella, E., Upadhyay, N., Tona, F., Prosperini, L., De Giglio, L., Petsas, N., . . . Pantano, P. (2017). Dentate nucleus connectivity in adult patients with multiple sclerosis: functional changes at rest and correlation with clinical features. *Mult Scler, 23*(4), 546-555. doi:1352458516657438 [pii]

10.1177/1352458516657438

Schmahmann, J. D., Doyon, J., McDonald, D., Holmes, C., Lavoie, K., Hurwitz, A. S., . . . Petrides, M. (1999). Three-dimensional MRI atlas of the human cerebellum in proportional stereotaxic space. *Neuroimage, 10*(3 Pt 1), 233-260. doi:10.1006/nimg.1999.0459

Schmitz-Hubsch, T., Coudert, M., Bauer, P., Giunti, P., Globas, C., Baliko, L., . . . Klockgether, T. (2008). Spinocerebellar ataxia types 1, 2, 3, and 6: disease severity and nonataxia symptoms. *Neurology, 71*(13), 982-989. doi:01.wnl.0000325057.33666.72 [pii]

10.1212/01.wnl.0000325057.33666.72

Schoonheim, M. M., Meijer, K. A., & Geurts, J. J. (2015). Network collapse and cognitive impairment in multiple sclerosis. *Front Neurol, 6*, 82. doi:10.3389/fneur.2015.00082

Sclocco, R., Beissner, F., Bianciardi, M., Polimeni, J. R., & Napadow, V. (2018). Challenges and opportunities for brainstem neuroimaging with ultrahigh field MRI. *Neuroimage, 168*, 412-426. doi:10.1016/j.neuroimage.2017.02.052

Selvadurai, L. P., Harding, I. H., Corben, L. A., & Georgiou-Karistianis, N. (2018). Cerebral abnormalities in Friedreich ataxia: A review. *Neurosci Biobehav Rev, 84*, 394-406. doi:S0149-7634(17)30186-0 [pii]

10.1016/j.neubiorev.2017.08.006

Selvadurai, L. P., Harding, I. H., Corben, L. A., Stagnitti, M. R., Storey, E., Egan, G. F., . . . Georgiou-Karistianis, N. (2016). Cerebral and cerebellar grey matter atrophy in Friedreich ataxia: the IMAGE-FRDA study. *J Neurol, 263*(11), 2215-2223. doi:10.1007/s00415-016-8252-7

10.1007/s00415-016-8252-7 [pii]

Shakkottai, V. G., Batla, A., Bhatia, K., Dauer, W. T., Dresel, C., Niethammer, M., . . . Strick, P. L. (2017). Current Opinions and Areas of Consensus on the Role of the Cerebellum in Dystonia. *Cerebellum, 16*(2), 577-594. doi:10.1007/s12311-016-0825-6

Shmuel, A., Yacoub, E., Chaimow, D., Logothetis, N. K., & Ugurbil, K. (2007). Spatio-temporal point-spread function of fMRI signal in human gray matter at 7 Tesla. *Neuroimage, 35*(2), 539-552. doi:10.1016/j.neuroimage.2006.12.030

Sled, J. G., Zijdenbos, A. P., & Evans, A. C. (1998). A nonparametric method for automatic correction of intensity nonuniformity in MRI data. *IEEE Trans Med Imaging, 17*(1), 87-97. doi:10.1109/42.668698

Smith, S. M., & Nichols, T. E. (2009). Threshold-free cluster enhancement: addressing problems of smoothing, threshold dependence and localisation in cluster inference. *Neuroimage, 44*(1), 83-98. doi:10.1016/j.neuroimage.2008.03.061

Sobotta, J. (1908). *Atlas and text‐book of human anatomy* (Vol. I, II and III). Philadelphia and London: W. B. Saunders Company.

Sokolov, A. A., Miall, R. C., & Ivry, R. B. (2017). The Cerebellum: Adaptive Prediction for Movement and Cognition. *Trends Cogn Sci, 21*(5), 313-332. doi:S1364-6613(17)30034-7 [pii]

10.1016/j.tics.2017.02.005

Solbach, K., Kraff, O., Minnerop, M., Beck, A., Schols, L., Gizewski, E. R., . . . Timmann, D. (2014). Cerebellar pathology in Friedreich's ataxia: atrophied dentate nuclei with normal iron content. *Neuroimage Clin, 6*, 93-99. doi:10.1016/j.nicl.2014.08.018

S2213-1582(14)00127-2 [pii]

Stefanescu, M. R., Dohnalek, M., Maderwald, S., Thurling, M., Minnerop, M., Beck, A., . . . Timmann, D. (2015). Structural and functional MRI abnormalities of cerebellar cortex and nuclei in SCA3, SCA6 and Friedreich's ataxia. *Brain, 138*(Pt 5), 1182-1197. doi:awv064 [pii]

10.1093/brain/awv064

Steinlin, M. (2008). Cerebellar disorders in childhood: cognitive problems. *Cerebellum, 7*(4), 607-610. doi:10.1007/s12311-008-0083-3

Stephen, R., Elizabeth, Y., & Christophe, H. (2018). Participation of the caudal cerebellar lobule IX to the dorsal attentional network. *Cerebellum Ataxias, 5*, 9. doi:10.1186/s40673-018-0088-8

88 [pii]

Stoodley, C. J., & Schmahmann, J. D. (2010). Evidence for topographic organization in the cerebellum of motor control versus cognitive and affective processing. *Cortex, 46*(7), 831-844. doi:10.1016/j.cortex.2009.11.008

Tsui, J. K., Eisen, A., Stoessl, A. J., Calne, S., & Calne, D. B. (1986). Double-blind study of botulinum toxin in spasmodic torticollis. *Lancet, 2*(8501), 245-247. doi:10.1016/s0140-6736(86)92070-2

Tzourio-Mazoyer, N., Landeau, B., Papathanassiou, D., Crivello, F., Etard, O., Delcroix, N., . . . Joliot, M. (2002). Automated anatomical labeling of activations in SPM using a macroscopic anatomical parcellation of the MNI MRI single-subject brain. *Neuroimage, 15*(1), 273-289. doi:10.1006/nimg.2001.0978

S1053811901909784 [pii]

Uwano, I., Kudo, K., Yamashita, F., Goodwin, J., Higuchi, S., Ito, K., . . . Sasaki, M. (2014). Intensity inhomogeneity correction for magnetic resonance imaging of human brain at 7T. *Med Phys, 41*(2), 022302. doi:10.1118/1.4860954

van Baarsen, K. M., Kleinnijenhuis, M., Jbabdi, S., Sotiropoulos, S. N., Grotenhuis, J. A., & van Cappellen van Walsum, A. M. (2016). A probabilistic atlas of the cerebellar white matter. *Neuroimage, 124*(Pt A), 724-732. doi:10.1016/j.neuroimage.2015.09.014

van den Heuvel, M. P., & Hulshoff Pol, H. E. (2010). Exploring the brain network: a review on resting-state fMRI functional connectivity. *Eur Neuropsychopharmacol, 20*(8), 519-534. doi:10.1016/j.euroneuro.2010.03.008

Van Dijk, K. R., Sabuncu, M. R., & Buckner, R. L. (2012). The influence of head motion on intrinsic functional connectivity MRI. *Neuroimage, 59*(1), 431-438. doi:S1053-8119(11)00821-4 [pii]

10.1016/j.neuroimage.2011.07.044

Vavla, M., Arrigoni, F., Nordio, A., De Luca, A., Pizzighello, S., Petacchi, E., . . . Martinuzzi, A. (2018). Functional and Structural Brain Damage in Friedreich's Ataxia. *Front Neurol, 9*, 747. doi:10.3389/fneur.2018.00747

Villringer, A., Them, A., Lindauer, U., Einhäupl, K., & Dirnagl, U. (1994). Capillary perfusion of the rat brain cortex. An in vivo confocal microscopy study. *Circ Res, 75*(1), 55-62. doi:10.1161/01.res.75.1.55

Ward, P. G. D., Harding, I. H., Close, T. G., Corben, L. A., Delatycki, M. B., Storey, E., . . . Egan, G. F. (2019). Longitudinal evaluation of iron concentration and atrophy in the dentate nuclei in friedreich ataxia. *Mov Disord, 34*(3), 335-343. doi:10.1002/mds.27606

Weier, K., Fonov, V., Lavoie, K., Doyon, J., & Collins, D. L. (2014). Rapid automatic segmentation of the human cerebellum and its lobules (RASCAL)--implementation and application of the patch-based label-fusion technique with a template library to segment the human cerebellum. *Hum Brain Mapp, 35*(10), 5026-5039. doi:10.1002/hbm.22529

Weier, K., Penner, I. K., Magon, S., Amann, M., Naegelin, Y., Andelova, M., . . . Sprenger, T. (2014). Cerebellar abnormalities contribute to disability including cognitive impairment in multiple sclerosis. *PLoS One, 9*(1), e86916. doi:10.1371/journal.pone.0086916

PONE-D-13-33234 [pii]

Winkler, A. M., Ridgway, G. R., Webster, M. A., Smith, S. M., & Nichols, T. E. (2014). Permutation inference for the general linear model. *Neuroimage, 92*(100), 381-397. doi:10.1016/j.neuroimage.2014.01.060

Wolf, R. C., Thomann, P. A., Sambataro, F., Wolf, N. D., Vasic, N., Landwehrmeyer, G. B., . . . Orth, M. (2015). Abnormal cerebellar volume and corticocerebellar dysfunction in early manifest Huntington's disease. *J Neurol, 262*(4), 859-869. doi:10.1007/s00415-015-7642-6

Worsley, K. J., Marrett, S., Neelin, P., Vandal, A. C., Friston, K. J., & Evans, A. C. (1996). A unified statistical approach for determining significant signals in images of cerebral

activation. *Hum Brain Mapp, 4*(1), 58-73. doi:10.1002/(sici)1097-0193(1996)4:1<58::aid-hbm4>3.0.co;2-o

Yablonskiy, D. A., & Haacke, E. M. (1994). Theory of NMR signal behavior in magnetically inhomogeneous tissues: the static dephasing regime. *Magn Reson Med, 32*(6), 749-763. doi:10.1002/mrm.1910320610

Yang, H., Wang, N., Luo, X., Lv, H., Liu, H., Li, Y., & Fan, G. (2019). Cerebellar atrophy and its contribution to motor and cognitive performance in multiple system atrophy. *Neuroimage Clin, 23*, 101891. doi:S2213-1582(19)30241-4 [pii]

10.1016/j.nicl.2019.101891

Zhang, Y., Brady, M., & Smith, S. (2001). Segmentation of Brain MR Images Through a Hidden Markov Random Field Model and the Expectation-Maximization Algorithm. *IEEE Transaction on Medical Imaging, 20*(1), 45-57. doi:10.1109/42.906424